British Geological Survey
NATURAL ENVIRONMENT RESEARCH COUNCIL

JARÐFEINGI

The three-dimensional crustal structure of the Faroe-Shetland region

Marine Geoscience Programme

Commissioned Report CR/10/110

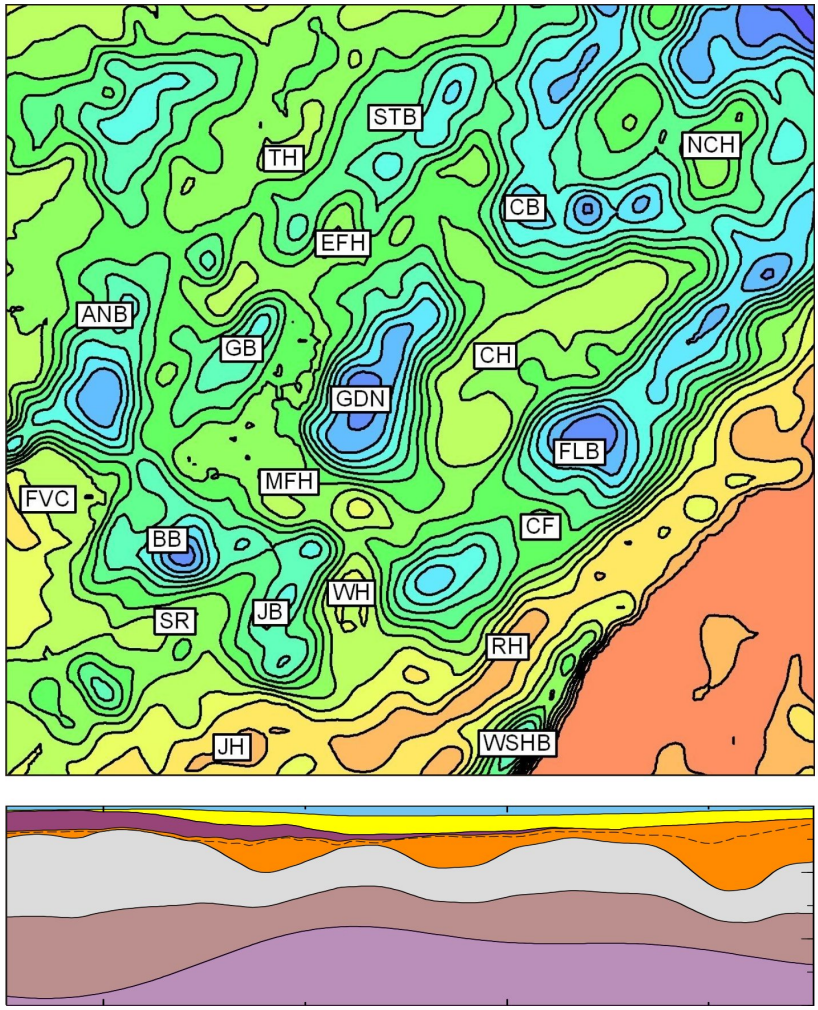

BRITISH GEOLOGICAL SURVEY

MARINE GEOSCIENCE PROGRAMME

COMMISSIONED REPORT CR/10/110

The three-dimensional crustal structure of the Faroe-Shetland region

G S Kimbell, D B McInroy, M F Quinn and H Ziska

Contributor

B C Chacksfield

Keywords

Faroe-Shetland Basin, gravity, magnetic, modelling.

Front cover

Illustrations of the 3D model in map (top basement) and section views.

Bibliographical reference

KIMBELL, G S, MCINROY, D B, QUINN, M F, AND ZISKA, H. 2010. The three-dimensional crustal structure of the Faroe-Shetland region. *British Geological Survey Commissioned Report*, CR/10/110. 102pp.

Keyworth, Nottingham British Geological Survey 2010

BRITISH GEOLOGICAL SURVEY

The full range of our publications is available from BGS shops at Nottingham, Edinburgh, London and Cardiff (Welsh publications only) see contact details below or shop online at www.geologyshop.com

The London Information Office also maintains a reference collection of BGS publications, including maps, for consultation.

We publish an annual catalogue of our maps and other publications; this catalogue is available online or from any of the BGS shops.

The British Geological Survey carries out the geological survey of Great Britain and Northern Ireland (the latter as an agency service for the government of Northern Ireland), and of the surrounding continental shelf, as well as basic research projects. It also undertakes programmes of technical aid in geology in developing countries.

The British Geological Survey is a component body of the Natural Environment Research Council.

British Geological Survey offices

BGS Central Enquiries Desk

Tel 0115 936 3143 Fax 0115 936 3276

email enquiries@bgs.ac.uk

Kingsley Dunham Centre, Keyworth, Nottingham NG12 5GG

Tel 0115 936 3241 Fax 0115 936 3488

email sales@bgs.ac.uk

Murchison House, West Mains Road, Edinburgh EH9 3LA

Tel 0131 667 1000 Fax 0131 668 2683

email scotsales@bgs.ac.uk

Natural History Museum, Cromwell Road, London SW7 5BD

Tel 020 7589 4090 Fax 020 7584 8270

Tel 020 7942 5344/45 email bgslondon@bgs.ac.uk

Columbus House, Greenmeadow Springs, Tongwynlais, Cardiff CF15 7NE

Tel 029 2052 1962 Fax 029 2052 1963

Maclean Building, Crowmarsh Gifford, Wallingford OX10 8BB

Tel 01491 838800 Fax 01491 692345

Geological Survey of Northern Ireland, Colby House, Stranmillis Court, Belfast BT9 5BF

Tel 028 9038 8462 Fax 028 9038 8461

www.bgs.ac.uk/gsni/

Parent Body

Natural Environment Research Council, Polaris House, North Star Avenue, Swindon SN2 1EU

Tel 01793 411500 Fax 01793 411501

www.nerc.ac.uk

Website www.bgs.ac.uk

Shop online at www.geologyshop.com

Acknowledgements

This project is one of a series that are being sponsored by the Faroe-Shetland Consortium, which consists of the British Geological Survey, Jarðfeingi (the Faroese Earth and Energy Directorate) and the following commercial partners:

Chevron UK Limited
ConocoPhillips (UK) Ltd
Dana Petroleum Plc
ENI UK Ltd
DONG Energy
E.ON Ruhrgas UK North Sea Limited
Faroe Petroleum
Nexen Petroleum U.K. Limited
A/S Norske Shell
Statoil UK Ltd
TOTAL E&P UK Ltd

We gratefully acknowledge the following data contributors:

Fugro Multi Client Services (UK) Ltd	- seismic data
BP Exploration Operating Co. Ltd	- seismic data
WesternGeco	- gravity, magnetic and bathymetric data
Common Data Access Ltd	- UK released well data
KMS[1]	- gravity and bathymetric data
GEBCO (IOC, IHO and BDC)[2]	- bathymetric data
Scripps Institute	- satellite-derived gravity data

1 Kort og Matrikelstyrelsen, Department of Geodynamics, Technical University of Denmark, DTU Space
2 Intergovernmental Oceanographic Commission, International Hydrographic Organization and British Oceanographic Data Centre

Contents

FIGURES

Summary

A three-dimensional model of the Faroe-Shetland region has been constructed, which incorporates new seismic mapping, rock property models derived from a large database of geophysical well logs, and deeper structure based on gravity inversion. New gravity, magnetic and topographic compilations were produced which integrate BGS and released Faroese data. A large seismic database spanning the Faroese and UK sectors of the Faroe-Shetland Basin was used to map seabed, the top of the Palaeogene volcanic sequence and, where possible, base volcanics, base Cenozoic and top basement. Velocity logs and VSPs were used to derive velocity models that were employed in the depth conversion of these data. Published sources were used to extend the model into neighbouring basins (the North-east Rockall Basin, Møre Basin and Northern North Sea). Analysis of density logs was used to define compaction trends in sedimentary sequences and departures from these relating to overcompaction and lithological variation. A density model was derived for the volcanic rocks which reflected the differences between the massive flows observed on the Faroe Islands and volcanic sequences elsewhere which include a higher content of relatively porous material (weathered layers, hyaloclastites, volcaniclastics) and do display compaction trends. A method was developed for quantifying the influence of sills on the average density of the sequence into which they were intruded.

The cover sequence geometries and rock densities were incorporated into a regional gravity model and inversion of short- and long-wavelength gravity anomalies was used to refine the forms of the top basement and Moho interfaces respectively. Density anomalies associated with the intrusive components of volcanic centres were incorporated in the model. Forward modelling was used to predict the magnetic signatures generated by the volcanic rocks and crystalline basement on the basis of simple magnetic property assumptions. The modelling results were assessed by comparison with wide-angle and normal incidence seismic results. The modelled top basement depths were converted into two-way travel time and integrated into the seismic workstation environment so that it was possible to interrogate the seismic database for evidence of any indications of structures that might have been missed without the guidance provided by the gravity model. The geophysical imaging and modelling results were analysed in a GIS and loaded into a customised viewer that facilitates the detailed comparison of multiple mapped and modelled layers, and the linkage of these to descriptive text.

The modelling results provide a new view of the compartmentalisation of the Faroe-Shetland Basin, resolving the forms of a complex set of sub-basins and structural highs. On the western side of the basin its components are strongly influenced by a north-north-east structural grain whereas, in the east, north-east to east-north-east trends are more evident. The gravity signatures over the Munkagrunnur Ridge indicate a requirement for low density rocks beneath the volcanic sequence proven by the Lopra borehole. There is little evidence for deep basins beneath the Fugloy Ridge but basins are indicated further to the north-east beneath the Pilot Whale Anticline and the Møre Marginal High. The relatively subdued gravity expression of the Faroe Bank Channel Basin is attributed to the presence within it of a substantial volume of dense igneous rocks, including both extrusive and intrusive components. The results provide new insights into the igneous history of the region, identifying a set of normally magnetised, low density intrusions north of the Faroe Islands and beneath the Faroe Bank, which may be analogues of the post-breakup felsic intrusions observed in East Greenland. Although not a primary target, the successful resolution of basement structure beneath the Northern North Sea provides a useful test of the metholodology.

This project has established a structural framework which should form a useful foundation for future studies of the structure and geodynamic evolution of the Faroe-Shetland region.

1 Introduction

This report describes the construction of a three-dimensional model of the crustal structure of the Faroe-Shetland region. The modelled area is shown in Figure 1 which is based on the structural map of Ritchie et al. (2011; see also Appendix 1). The modelling extended beyond the limits of that map, to the boundary of the rectangle shown, including parts of the Møre Basin and Northern North Sea in the east and the North-east Rockall Basin in the south-west. In UTM Zone 30 coordinates the model limits are:

160000 – 810000 m E, 6510000N – 7110000 m N

The aim of the project was to provide a regional structural framework that would underpin other activities within the Faroe-Shetland Consortium (FSC). The methodology was based on that originally described by Kimbell et al. (2004, 2005) and subsequently refined in a series of projects on the Atlantic margin (e.g. Kimbell et al., 2010). The aim in this case was to combine the best available potential field (gravity and magnetic) data from both the Faroese and UK parts of the region and integrate the modelling of these data with the interpretation of an extensive seismic database in a more detailed fashion than has previously been attempted.

This report provides an account of the methods used to generate a regional crustal model, but it is probably not the best medium to use for inspecting the results of that modelling and integrating them with other sources of information. Readers are referred to the GIS versions of the project outputs (Appendix 2) and the FSC Viewer (Appendix 3) for these purposes.

2 Data compilation

2.1 SEISMIC DATA

The area covered by the seismic database established for the project is illustrated in Figure 2. The Faroese coverage is based on released data from that area (see http://jf.fo/surveys/Seismic/). In the UK sector, about 19000 km of 2D and 14000 km^2 of 3D seismic data were assembled. This included released proprietary data contributed by Faroe-Shetland Consortium members and BP Exploration Operating Co. Ltd, together with speculative data kindly donated by Fugro Multi Client Services (UK) Ltd. The line locations in this part of the study area are not shown in Figure 2, to comply with the terms of provision of certain of the datasets.

2.2 GRAVITY DATA

A gravity compilation was established which merged BGS data with the results of released Faroese surveys and filled the areas where marine coverage was poor or absent using satellite-derived gravity data provided by the Scripps Institute, University of San Diego (Sandwell and Smith, 2009; Version 18.1 of this dataset was employed). Land areas were covered by BGS gravity stations on Orkney and Shetland, and Kort og Matrikelstyrelsen (KMS; Department of Geodynamics, Technical University of Denmark, DTU Space) stations on the Faroe Islands. The data distribution is illustrated in Figure 3. WesternGeco kindly gave permission for the UK extensions of their Faroese marine gravity surveys to be employed in this project and this has led to a distinct improvement in the coverage in the vicinity of the median line.

When the Faroese and BGS data were initially merged, an offset between the respective gravity fields was observed which increased in a southward direction. Comparison with the satellite-derived field suggested that the best solution was to leave the BGS and satellite data unchanged and apply a smoothly varying correction to the Faroese component that minimised the discrepancies. The final compilation was gridded at 1 km intervals using a tensioned spline algorithm (tension = 0.1) and smoothed using a low-pass Butterworth filter with order 8 and a central wavelength of 7.5 km. Imaging of the final merged dataset (Figure 4) indicates satisfactory joins between the different sources. The shorter wavelength content of the latest satellite-derived gravity dataset makes the contrast between this and neighbouring marine surveys less noticeable than in previous compilations.

A series of transformations have been applied to the gravity data and images of these are provided as georeferenced images (see Appendix 2). Figure 5 shows the isostatically corrected Bouguer gravity anomaly, a transformation which helps to isolate the gravity expression of upper-crustal density contrasts by removing that of topography/bathymetry and compensating variations in the depth to Moho.

2.3 MAGNETIC DATA

The primary source of magnetic data was a series of magnetic surveys owned by BGS (Figure 6). These comprised digitised analogue aeromagnetic surveys in the area around Orkney and Shetland, digital aeromagnetic surveys (originally acquired by Hunting Geology and Geophysics) in the Faroe-Shetland - North Rockall areas and marine magnetic data in the northern North Sea. The closest line spacing is 2 km (in the analogue aeromagnetic surveys and to the north-west of Shetland) and elsewhere the spacing is typically between 5 km and 10 km. In addition, aeromagnetic data from Project Magnet (US Department of the Navy) were employed in the area immediately south of the Faroe Islands; these data were acquired along

east-west lines with a spacing of 2.75 km. In the initial data compilation, the areas to the north and east of this coverage was filled with data from the GAMMAA5 compilation (Verhoef et al., 1996; © Department of Natural Resources Canada. All rights reserved). Data were gridded on a 1 km mesh using a spline with tension of 0.1 and a series of images and transforms generated (Figure 7; Appendix 2).

The GAMMAA5 coverage is poor to the north of the Faroe Islands, making it difficult to identify the continent-ocean boundary and oceanic magnetic anomalies in this area. Recent surveys by the Norwegian Geological Survey have addressed this data gap, but have not yet been made public. As an interim measure, an alternative magnetic compilation was generated which substituted marine magnetic data acquired by WesternGeco in this area (Figure 8). This provides improved imaging immediately north of the Faroe Islands and a clearer representation of the shortcomings of the coverage over the Norwegian Basin farther north.

2.4 TOPOGRAPHIC DATA

The topographic compilation was based on the data points shown in Figure 9. The main data source was soundings from marine geophysical surveys, but contours from the GEBCO Digital Atlas (IOC, IHO and BODC, 2003) were included in the north and east where original survey data were not available. These contours were compiled by Peter Hunter of the Southampton Oceanography Centre (now the National Oceanography Centre). In the onshore areas, topography in UK areas was based on gravity station elevations and on the Faroe Islands was based on data from the National Geophysical Data Centre (NGDC) GLOBE database.

The topographic data were gridded at 1 km intervals using a spline with a tension of 0.1 and smoothed using a low-pass Butterworth filter with order 8 and a central wavelength of 10 km. The resulting topographic model is illustrated in Figure 10. The grid was converted to two-way travel time (twtt) assuming a sea water velocity of 1.468 km/s and interpolated onto the points of the seabed pick in the seismic interpretation (see Section 4) in order to check for consistency.

3 Rock properties

3.1 INTRODUCTION

Models for the spatial variations in rock densities and velocities across the region were required as inputs to the gravity modelling and seismic depth conversion respectively. Geophysical well logs from 148 released offshore wells were employed in the physical property analysis, together with results from onshore drilling in the Faroe Islands (in particular Lopra-1/1A) (Figure 11). A series of side-by-side displays of compensated bulk density and sonic (P-wave) velocity logs have been produced, and some examples are shown in Figures 12 and 13. The full set of log displays is provided in a separate pdf file (fsc_geophys_well_logs.pdf), and they can also be accessed via hotlinks in the GIS (Appendix 2) and the FSC Viewer (see Appendix 3). In each case, depths are plotted relative to seabed, in order to identify compaction trends on a consistent basis, and alternative empirical compaction curves are shown for reference. The main chronostratigraphic boundaries are also indicated, although it should be noted that these were identified from a range of sources and their reliability cannot be guaranteed. Caution is also necessary when viewing the geophysical well logs as there are instances where distortions relating to casing, poor hole conditions or logging tool malfunction appear likely.

3.2 DENSITIES

3.2.1 Sedimentary rocks

The density data are plotted against compaction curves for shale, sand and chalk which are based on the empirical porosity trends of Sclater and Christie (1980). The saturated bulk density is given by an exponential relationship of the form:

$$\rho = a - be^{-cz} \qquad (3.1)$$

where ρ is density and z is depth below seabed

The constant 'a' is effectively grain density of the sedimentary rock and the exponential term simulates the influence of porosity. If ρ is in Mg/m^3 and z is in km, and a density for sea water of 1.03 Mg/m^3 is assumed, the constants in this expression are (Sclater and Christie, 1980):

Chalk:	a = 2.71	b = 1.176	c = 0.71
Shale:	a = 2.72	b = 1.065	c = 0.51
Sand:	a = 2.65	b = 0.794	c = 0.27

Overall, the log plots indicate that the shale curve appears most representative of the densities of sedimentary rocks in the central part of the Faroe-Shetland Basin, in line with previous gravity modelling of the deep-water basins along the NE Atlantic margin (e.g. Kimbell et al., 2010). Some departures from this generalisation can be ascribed to lithological variations. Volcanic rocks are responsible for some very obvious high density zones and relatively low densities can typically be correlated with sand-rich units, particularly within the Paleocene. For example, in well 204/22-2 sand-rich units at 1700-2400 m below sea bed lie on a lower density trend than the overlying and underlying mud-rich units (Figure 12a). Perhaps suprisingly, the thick sequence of sands encountered in wells drilled in the Faroese sector (e.g. 6004/16-1Z; Smallwood et al., 2004) has densities closer to the the shale compaction curve than the sand curve (Figure 12b).

The logs reveal an area of relatively high density Palaeocene sedimentary rocks in the northern part of the Flett Basin (e.g. 214/19-1; Figure 13a). The densities lie close to those predicted for

chalk but the descriptions in the composite logs indicate the dominance of mudrocks, without a particularly high calcareous content. The area is inferred to have been one of marine sedimentation throughout the Cenozoic (e.g. Stoker and Varming, 2011, fig. 100; Stoker et al., 2005, fig. 11) so overcompaction as a result of uplift and erosion is unlikely, although removal of overburden through submarine erosion does provide a possible explanation. There is uncertainty in this explanation, however, as well 206/01-3 (see separate pdf file) suggests normally compacted mudrocks above and below an anomalous Palaeocene unit. There is also a problem in that the shape of the density curve differs from that of the shale compaction curve, regardless of offset, and that there is not the concomitent offset in velocities that might be expected if the effect was simply due to overcompaction. In well 214/28-1, Holmes et al. (1999, their p. 1358 and fig. 12) noted an increase in thermal maturity that corresponds a zone of density offset in the geophysical well log. Holmes et al. (1999) attributed this to low-impact contact metamorphism and possibly hot fluid circulation, but acknowledged that such effects are neither uniform nor well-understood. The effect seems too extensive for contact metamorphism associated with the Faroe-Shetland Sill Complex (see Section 3.2.3), but a more pervasive alteration associated with fluid circulation is a possibility. The fact that the anomalous densities appear to extend into Middle Eocene rocks that post-date the intrusion of this complex (Figure 13a) is a potential impediment to this interpretation. Whatever its explanation, the anomaly in Paleocene densities needs to be allowed for in the gravity modelling. It was assessed that this could be done with sufficient accuracy by approximating it in terms of an equivalent shift to the shale normal compaction curve (Figure 14a).

Significant offsets to higher densities are observed in Pre-Cenozoic sediments preserved on structural highs and perched basins in the region and are attributed to overcompaction resulting from uplift and erosion in these areas. Figure 13b illustrates an example from the Solan Bank High (well 202/09-1) where densities in the Mesozoic sequence are characteristic of mudrocks buried more than 1 km deeper than at present. A map of apparent denudation observed in pre-Cenozoic sedimentary rocks has been constructed from the available well data, on the basis of offsets from the shale compaction curve of Sclater and Christie (1980) (Figure 14b). This is generalised, as the current state of knowledge is considered insufficient to map denudation variations in more detail. The part of the sequence affected by such denudation has been separated in a simplistic way, making no attempt to simulate the multiple unconformities observed in the area (note, for example, that the thin Cretaceous sequence in well 202/09-1 (Figure 13b) appears normally compacted). Away from areas where well data are not available, denudation estimates were guided by erosional truncation observed in seismic sections (e.g. Andersen et al., 2002). The distribution of zeolites in volcanic units also provides evidence of maximum depth of burial and thus the thickness that has been removed by erosion (Jørgensen, 2006).

Overpressure is observed in the Faroe-Shetland Basin (e.g. Carr and Scotchman, 2003) and might be expected to reduce rock densities below values predicted by a normal compaction curve. There is not, however, evidence in the well logs of large scale reductions in density that would justify quantification of this effect within a gravity model. Recent drilling through the basalts in the Faroese area has suggested the possibility of significant overpressure in the strata that underly them (D. Ellis, presentation at the 3rd Faroe Islands Exploration Conference, Tórshavn, September, 2009). Although it is not yet possible to quantify any influence this might have on rock densities it has prompted a conservative approach to assumptions about the effect of denudation on rock densities in the Faroese area.

3.2.2 Volcanic rocks

Figure 15a illustrates the available density logs through volcanic sequences in the Faroe Shetland region, together with results from DSDP/ODP drilling through similar sequences on the Vøring (Site 642) and East Greenland (Site 917A) margins. Densities within such sequences typically exhibit high variability, so a moving average filter has been applied in order to make underlying

trends more easily observable. Densities within the Faroe-Shetland and northern Rockall basins lie on a broadly similar trend, which is reminiscent of the compaction trend seen in sedimentary rocks. It is likely that this reflects the effect of compaction on the porous strata within the volcanic sequence, such as weathered units, hyaloclastites, and volcaniclastic/sedimentary rocks.

In contrast, densities in the Lopra borehole do not show a pronounced compaction trend, and vary about an average of 2.80 - 2.85 Mg/m^3 throughout the borehole (Figure 15a). This reflects the preponderance of very low porosity, massive flows within the sequence intersected. Densities within the volcaniclastic unit at 2550-2900 m decrease to a level that lies along the projection of the trend observed in the wells in the basins to the east and south (Figure 15a). Digital density log data for the deeper part of the borehole (down to TD at 3565 m) were not available to this project, but the illustration of these data by Ellis et al. (2002, fig. 3) shows that the average density of this section is similar to that observed above the volcaniclastic unit.

Although highly variable, the DSDP/ODP density data (Figure 15a) do indicate an underlying increase in density with depth along a trend that lies between those of Lopra and the wells to the east and south. The DSDP/ODP boreholes lie at the seaward edge of the landward flows on their respective margins and intersect volcanic sequences which are intermediate in terms of their constituents.

A density model has been adopted for the volcanic rocks which is similar to that used for the sediments, in that it is based on an exponential relationship to which a depth offset is applied depending on position within the study area. The difference is that, while the sedimentary offset is largely dictated by degree of denudation, the one for volcanic rocks includes other factors, in particular the relative proportion of massive and porous components. The reference curve is given by:

$$\rho = 2.85 - 0.55e^{-0.7z} \qquad (3.2)$$

where ρ is density in Mg/m^3 and z is depth in km.

Arbitrarily, a zero offset was ascribed to the trend defined by the DSDP/ODP wells. Negative offsets were then applied to sequences with a higher proportion of porous components and positive offsets to those with more massive components, and these were mapped across the area as shown in Figure 15b. The average density of the volcanic sequence was not allowed to descend below a 'floor' value of 2.3 Mg/m^3. The assumed offsets broadly honour the available data but there are, of course, large areas which are poorly constrained. An advantage of the current scheme is that it is straightforward to revise as more data become available. The offset of c. +2 km employed on the Faroe Islands somewhat underestimates densities in the top kilometre of the Lopra borehole (Figure 15a), but does appear to provide reasonable replication of average densities encountered in the Vestmanna and Glyvursnes boreholes (Japsen et al., 2005).

It should be noted that geophysical logging tools potentially underestimate the density of volcanic rocks because they are not calibrated for such lithologies. In the case of the Schlumberger compensated formation density tool, the true density of a molecular substance can be calculated from its measured density by an expression based on the ratio between the sum of the atomic numbers of the atoms making up the molecule and the molecular weight (Schlumberger, 1989). When averaged geochemical data from the Lopra borehole (Hald and Waagsten, 1984) are employed in this expression it predicts that the densities of massive basalt units will be underestimated by approximately 0.04 Mg/m^3. Given the variability in basalt properties, and uncertainty regarding the logging methods and corrections employed in the available released data, no allowance has been made for calibration errors in the logs shown here.

The density model described above was also employed in oceanic layer 2 in the gravity model (see Section 5). Calibration was provided by combining the measured average velocity in this layer (e.g. from the iSIMM experiment; White et al., 2008) with the velocity-density relationship of Carlson and Herrick (1990). The latter relationship does not apply to continental lavas, but

some degree of comparability between densities and velocities in this area is possible using trends revealed by crossplots from the Lopra borehole (Boldreel, 2006).

3.2.3 Sills

The Faroe-Shetland Sill Complex comprises a belt of sills and associated dykes that extends along the axis of the Faroe-Shetland Basin (Hitchen and Ritchie, 1987; Gibb and Kanaris-Sotiriou, 1988; Bell and Butcher, 2002; Smallwood and Maresh, 2002; Trude et al., 2003; Thomson, 2007; Passey and Hitchen, 2011). The sills are imaged by seismic surveys as a series of high-amplitude reflections, often with saucer-shaped geometries, and have been intersected by a number of wells. Available isotopic data (summarised by Passey and Hitchen, 2011) indicate ages between 55 Ma and 52 Ma. The majority of the sills are intruded into Late Cretaceous mudrocks, and are less common within the overlying Paleocene sequence. Although 3D seismic surveys have significantly improved the imaging of the sill complex (e.g. Thomson, 2007), there is still considerable uncertainty about the cumulative thickness of igneous material present, particularly towards the north-west where imaging of the sills is impaired by the effects of the overlying extrusive volcanic sequence.

Geophysical logs through the Faroe-Shetland Sill Complex from wells 208/21-1 and 219/20-1 are shown in Figures 16 and 17 respectively. The former well intersected 11 sills with a cumulative thickness of 243 m, spanning a vertical interval of 576 m; the latter intersected 19 sills with a total thickness of 365 m within a depth interval of 1415 m. The log responses are very clear: the sills have high density and sonic velocity together with a very low gamma count. Well 219/20-1 is the cleaner hole (compare the caliper records in Figures 16 and 17), so provides the clearer image of the physical property variations. In addition to the high density of the sills themselves there are consistent variations in the density of the adjacent country rocks (e.g. Figure 18a). Relative to a 'baseline' trend, their density rises as the sill is approached but then drops below this trend immediately adjacent to the sill, probably as a result of fracturing (Planke et al., 1999; Smallwood and Maresh, 2002).

Figure 18b provides a schematic illustration of the density variations across a typical sill, including approximate values for their extent and amplitude. The rise in the density of the country rocks, which is presumably associated with contact metamorphism, commences at a distance from the sill approximately equal to its thickness. The density change can be split into rising (0.6 of the thickness) and falling (0.4 of the thickness) components with maximum and minimum values of approximately +0.1 Mg/m^3 and -0.1 Mg/m^3 respectively relative to the baseline. On this basis, it is possible to estimate how much the presence of a cumulative thickness (t_s) of sills would increase the average density of a given thickness (t_b) of basin fill, given that it would otherwise have a density of ρ_b.

The effect of the sills themselves:

$$\Delta\rho_s = (2.95 - \rho_b)t_s / t_b$$

The effect of density variation in the country rock adjacent to the sills:

$$\Delta\rho_a = 0.06t_s / t_b$$

Giving a combined effect of:

$$\mathbf{\Delta\rho = (3.01 - \rho_b)t_s / t_b} \qquad (3.3)$$

Where $\Delta\rho$ and ρ_b are in Mg/m^3.

This formula can be used in gravity modelling sensitivity analyses by defining the top and bottom of the volume assumed to be occupied by the sill complex and adjusting the density of that volume by an amount predicted for a given cumulative thickness of sills.

3.3 VELOCITIES

3.3.1 Sedimentary rocks

Japsen et al. (2007) identified two types of mathematical expression that can be used to express velocity-depth trends in normally compacted rocks, and which can be related to physical models of how porosity varies with depth. These take the general forms:

$$v_p = a - be^{-cz} \quad (3.4)$$

$$v_p = 1 / (ke^{-lz} + m) \quad (3.5)$$

where v_p is compressional wave velocity (in km/s in the formulations that follow), z is depth (in km) and a, b, c and k, l, m are constants. Japsen et al. (2007) recommended using expressions of type 3.4 for sandstone and expressions of type 3.5 for shale.

Rearranging expression 3.4 and taking logarithms of both sides gives:

$$\ln(a - v_p) = \ln(b) - cz \quad (3.6)$$

Constant 'a' is a maximum velocity which is approached asymptotically at depth, and which can be guided by the metamorphic equivalents of the sedimentary rocks encountered in the basin. Taking 5.6 km/s as a representative value, Figure 19a illustrates a plot of $\ln(5.6 - v_p)$ against depth below seabed for about 300000 data points from the available sonic logs. Wells which intersected large sections of igneous material or overcompacted sedimentary rocks were omitted from this compilation but it does still contain examples of high velocities, which appear as points below the main 'cloud'. There is a much smaller number of anomalously low velocities above this cloud (only values greater than 1.5 km/s are displayed on the basis that lower values are likely to relate to measurement error).

The data in Figure 19a contains a linear trend, as predicted by equation 3.6 and the red line in the figure was fitted to this by linear regression applied to the subset of the data that forms the main cloud. This line appears representative at depths of less than 2-3 km below seabed but less so at greater depth, where it lies on the low side of the velocity trend and the observations form a much broader scatter. The formula for the line shown is:

$$v_p = 5.6 - 3.88e^{-0.19z} \quad (3.7)$$

Japsen (2000) used the following type 3.5 expression for normally compacted marine Early Jurassic shale in the North Sea area:

$$v_p = 1 / (0.460e^{-0.45977z} + 0.185) \quad (3.8)$$

Corcoran and Mecklenburgh (2005) assumed the following type 3.5 expression for normally compacted shale in the Slyne Basin. It was based on transit time data from deep wells with extensive shale sections in the neighbouring Rockall and Porcupine basins.

$$v_p = 1 / (0.40682e^{-0.50938z} + 0.18373) \quad (3.9)$$

These three curves (3.7, 3.8 and 3.9) are superimposed on all the velocity logs provided in fsc_geophys_well_logs.pdf, and in Figure 19b they are plotted against the merged velocity data. As inferred from the regression, expression (3.7) provides a good fit at depths less than 2-3 km, but at greater depth lies along a cluster of observations at relatively low velocity. Inspection of individual well logs suggests that this cluster relates to deep sequences of Cretaceous mudrocks (e.g. in wells 204/23-1, 205/22-1, 209/6-1, 209/12-1) and the mud-rich parts of the Paleocene sequence. Higher velocities appear to be associated with sandstone, limestone and igneous rocks. This expression therefore appears applicable to mudrocks, despite the contention of Japsen et al. (2007) that it is of a form more appropriate for sandstone. Curve (3.8) of Japsen (2000) lies on the lower side of the range of velocities sampled whereas curve (3.9) of Corcoran and Mecklenburgh (2005) lies closer to the centre of this range (Figure 19b). Japsen et al. (2007) suggested that the difference between the trends may be because of of the incorporation of non-

shale sediments in the analysis of Corcoran and Mecklenburgh (2005). Although the Japsen (2000) curve lies below the general trend there are sections of the logs that follow it closely (see, for example, parts of 163/06-1, 204/23-1, 206/5-2 and 214/04-1 in fsc_geophys_well_logs.pdf).

The choice of velocity trend depends on the purpose for which it is going to be used. If the main priority is in the estimation of amounts of denudation, the analysis should focus on the shale units and relate the velocities of these to a reference normal compaction curve tuned for this lithology. For present purposes the requirement is to derive a general trend that can be used for depth conversion across the basin, and as such will reflect a broader range of lithologies. For this purpose the analysis thus far has suggested that the choice is between curve 3.7 identified in this study and 3.9 of Corcoran and Mecklenburgh (2005).

Additional important evidence is provided by the results of vertical seismic profiles (VSPs) conducted in wells in the region. The available data are plotted against the three possible reference curves in Figure 20. This reveals that the exponential and Corcoran and Mecklenburgh (2005) relationships give similar results down to depths of about 4 km and that these appear more appropriate than the curve of Japsen (2000) over most of the area covered. The exception is in the north, in the Møre area, where the latter relationship provides a better fit. It is also worth noting that velocity data from the Faroese wells indicate a velocity trend that lies above all those discussed here.

Given the area and depths over which the depth conversion had to be conducted, it was decided to use the exponential relationship (3.7) for this study. It gives similar results to that of Corcoran and Mecklenburgh (2005) but has the advantages of: (i) being more amenable to the direct calculation of depth from time, and (ii) providing more conservative depth estimates at large travel times, which has advantages in terms of the stability of the subsequent gravity inversion. This compromise was adopted for the present study, but the departures noted above need to be borne in mind in any future, more detailed studies, particularly in the Møre and Faroese areas. Although it would be possible in principle to allow for velocity offsets due, for example, to denudation, this refinement was not included in the depth conversion because seismic mapping of deeper horizons, for which such an adjustment would be applicable, was generally confined to areas where such a velocity offset was unproven. Allowance was made for these effects subsequently in the inverse computation from modelled depth to time, as described in section 7.1.

3.3.2 Volcanic rocks

Figure 21 illustrates velocity logs through volcanic sequences in the Faroe-Shetland and North-east Rockall basins. As with the density data, a moving average has been applied in order to help discern trends within logs that exhibit a high degree of short wavelength variability. Although there are clearly substantial differences between the wells, they do jointly provide evidence of a broad compaction trend. Only part of the velocity log from the Lopra borehole was available digitally, but published versions of the more complete log (e.g. Christie et al., 2006) indicate no such trend. A VSP conducted in the deepened Lopra borehole indicated an average velocity of 5.248 km/s between surface and 3.51 km (Christie et al., 2006).

A velocity model was required that could be used to depth-convert the available seismic mapping of the base of the volcanic rocks. This pick is subject to significant uncertainty, particularly where the volcanic sequence is thick, and there is also considerable uncertainty in the average velocity of the volcanic sequence because of the variable proportions of high- and low-velocity components. In view of this, and of the area covered by the seismic interpretation, a single generalised velocity-depth relationship was used for the depth conversion. This is shown on Figure 21 and is described by:

$$\mathbf{v_p = 5.7 - 2.4e^{-0.45z}} \qquad (3.10)$$

Where v_p is in km/s and z is in km.

Such a relationship would not be appropriate for the sequence close to the Faroe Islands but the base volcanic pick did not extend into this area.

3.3.3 Depth conversion

The exponential expressions (3.7 and 3.10) adopted for the velocities in sedimentary and volcanic rocks within the basin are amenable to integration into direct analytical expressions of depth in terms of time:

For the sedimentary rocks:

$$z = \ln(0.307e^{0.532t} + 0.693) / 0.19 \qquad (3.11)$$

For the volcanic rocks:

$$z = \ln(0.579e^{1.2825t} + 0.421) / 0.45 \qquad (3.12)$$

Where z is depth in km and t is two-way travel time in km/s.

The above expressions are special cases where the medium extends as a single layer from surface down to depth z. In practice, the depth conversion was undertaken in a 'layer-cake' fashion in which the depth to the base of successive horizons (water, then various sedimentary and volcanic layers) was calculated in turn and provided an input to the calculation of the depth to the next interface. Optionally, a shift can be applied to the velocity function for each layer, for example to allow for the effects of overcompaction.

4 Construction of an initial cover sequence model

4.1 INTRODUCTION

The aim for the initial cover sequence model was to represent that part of the sequence that can be mapped seismically in a way that allows its gravity expression to be calculated, and to provide at least an initial estimate of deeper, less well imaged structure that would form the basis of optimisation by gravity inversion. The resolution of the gravity modelling is inherently limited, particularly over deeper structures, so fine resolution of local structure was not required. The choice of horizons was guided by insights into the density variations within the sequence provided by the physical property analysis as well as by the pragmatic requirement to adopt interfaces that could be mapped efficiently and over a sufficiently large area to make it realistic to incorporate them into the model. As described in the following sections, the interfaces mapped were:

Seabed
Top volcanics / Top Balder
Base volcanics
Base Cenozoic
Top Basement

Seismic horizons were mapped by Jarðfeingi in the Faroese sector and BGS in the UK sector. Given the resolution requirements, only a subset of the available lines was interpreted, but the detail of the seismic interpretation was nonetheless greater in places than could realistically be resolved by gravity data. To avoid aliasing of short-wavelength features, the seismic picks were binned within the 2 km cells that were used in the gravity modelling. The seismic mapping only covered part of the area of the 3D model and it was a requirement of the gravity modelling that all the structural surfaces covered the full study area. The surfaces were therefore extended to the boundary of this area using other data sources, as described in the following sections. In some cases this required the adoption of an approximate lateral equivalent. Where an interval was absent, its basal horizon was simply clipped to that of the overlying unit.

4.2 TOP VOLCANICS - TOP BALDER FORMATION

Where the Palaeogene volcanic sequence is present, its top forms a very clear and easily mapped reflector. Beyond the limit of the basalts this surface was linked to a Top Balder Formation pick, employing a 5 km wide ramp between the two to avoid a sharp step. Outside the area of Faroe Shetland Consortium mapping, the surface was extended using the sources shown in Figure 22. BGS mapping was employed in the south-west (British Geological Survey, 2007) and the north (British Geological Survey and Jarðfeingi, in preparation). In the east, Top Paleocene horizons from the Millenium Atlas (Evans et al., 2003) and from Roberts et al. (2009a) were used. Coverage in the north-west is limited to a few lines from the Faroese database and low resolution sediment thickness mapping from the North Atlantic Geophysical Atlas (Srivastava et al., 1988).

This horizon was constructed by first modelling thickness variations in the sediments that overlie it (Figure 23) and then subtracting this thickness from the bathymetric surface. This made it easier to model structures such as the tapering edge of the post-basalt sediments. The final model for the horizon is shown in Figure 24.

4.3 THICKNESS OF THE VOLCANIC SEQUENCE

The base of the volcanic sequence is often difficult to identify in seismic data. Some picks were made in the areas to the east and south-west of the Faroe Islands (the detailed contouring in Figure 25) but elsewhere it was only possible to produce a highly generalised model with very limited constraints. Typically, 2.5 - 3.0 km of volcanic rocks were assumed over the Faroe Platform and Fugloy Ridge, with thicker sequences beneath the Faroe Islands (as proved by the Lopra drilling) and where seaward-dipping reflectors were observed or inferred. The continental volcanic sequence was made continuous with oceanic layer 2 and the latter was assigned a thickness of 3 km, based on evidence from the iSIMM profile (Parkin and White, 2008).

4.4 BASE CENOZOIC

A base Cenozoic unconformity was mapped seismically in the UK area and linked to an approximate lateral equivalent beneath the Faroese area. In the south-east this was linked to the top Shetland Group surface mapped in the Millennium Atlas (Evans et al., 2003). In the north-east, limited well data (Norwegian wells 6302/6-1 and 6403/10-1) was combined with published data (in particular Vergara et al., 2001) to produce an approximate interface. Similarly, estimates in the south-west of the area were based on very limited well and seismic evidence. A map of the inferred sediment thickness between this interface and the horizon above (either Base Volcanics or Top Balder) is shown in Figure 26. The base Cenozoic horizon was not modified in the gravity inversion. For this reason its depth was kept to a minimum in poorly constrained areas. The consequence of this is that the 'pre-Cenozoic' component of the model, which *was* subjected to gravity inversion, may accommodate Paleocene sediment thickness variations in such areas.

4.5 TOP BASEMENT

The top basement surface could be identified on some well intersections and seismic lines in the UK part of the FSC database and also in the published results from normal incidence and wide-angle seismic experiments in the region (e.g. Klingelhofer et al. (2005) in the North-east Rockall Basin). In the Northern North Sea it was inferred from a combination of the deepest horizons mapped in the Millenium Atlas (Evans et al., 2003) and the mapping of Hospers and Ediriweera (1991). In the Møre Basin it was guided by published Base Cretaceous maps (e.g. Roberts et al. 2009a) and the top basement map of Ebbing and Olesen (2011).

Only a generalised initial top basement surface was required for input to the gravity modelling. The aim was to provide a starting point that would be a suitable constraint on initial modelling of depth to Moho while not containing short wavelength variations that would distort the gravity inversion. For this reason the initial pre-Cenozoic sediment thickness model (Figure 27) is highly smoothed and, subsequent to the subtraction of this from the base Cenozoic surface, further smoothing was undertaken to generate the initial top basement surface shown in Figure 28. For modelling purposes, the top of the continental basement was continuous with the top of oceanic layer 3 in the north-west.

5 Three-dimensional gravity modelling

5.1 MODEL CONFIGURATION

The gravity modelling procedure was based on that which has evolved through a series of studies of the Atlantic margin (e.g. Kimbell et al., 2004, 2010) but with some additional refinements. The model was assembled as a series of regular grids with a 2 km node spacing which defined the geometry of a set of interfaces between the surface and 125 km depth, and the density structure of the units lying between them.

In Figure 29, the components of the gravity model are shown schematically and superimposed on a velocity model across the continental margin in this region (White et al., 2008). The layers are as follows:

- Sea water, assigned a density of 1.03 Mg/m^3.
- Sedimentary rocks down to top volcanics / top Balder (S1 in Figure 29). This unit was assigned a density structure based on the normal shale compaction curve of Sclater and Christie (1980) (formula 3.1 in Section 3.2.1, with the shale constants employed). The seismic data allow more detailed subdivision of this layer, but only limited rock density data are available and do not warrant this additional complexity. Densities were therefore assigned on the basis of depth below seabed rather than stratigraphy.
- The volcanic sequence in continental areas, which was continuous with oceanic layer 2. This unit was assigned a density structure based on formula 3.2 in Section 3.2.2, to which the offsets illustrated in Figure 15b were applied.
- A Paleocene/earliest Eocene sedimentary layer (extended to include the Balder Formation to the south-east of the limit of the volcanic rocks). This is unit S2 in Figure 29. Its density was based on the shale compaction curve, offset by the amount indicated in Figure 14a.
- A pre-Cenozoic sedimentary layer (S3 in Figure 29), with a density structure based on the shale compaction curve offset by the amount shown in Figure 14b.
- The crystalline crust, which was subdivided into upper and lower units of equal thickness. In continental areas these were assigned densities of 2.75 Mg/m^3 and 2.95 Mg/m^3 respectively, while in oceanic areas they were 2.85 Mg/m^3 and 3.05 Mg/m^3 respectively. On the basis of the iSIMM velocity model (White et al., 2008), the change in densities was ramped across a zone extending 50 km landward from the continent-ocean boundary (Figure 29). Note that the term 'crystalline' is used loosely as the upper crust may contain relatively high density metasedimentary components.
- An upper mantle in which the density varied laterally and vertically on the basis of modelled temperatures. The method used is described by Kimbell et al. (2004) and Kimbell et al. (2010). On the basis of 2D finite-element thermal modelling, the transition between oceanic and continental temperature regimes was accommodated across a ramp which extended from 75 km oceanward of the continent-ocean boundary to 100 km landward of this boundary. The base of the zone of variable upper-mantle densities was set at a depth of 125 km.

The location of the continent-ocean boundary (COB) in this area was reviewed using recently published results from the iSIMM experiment and the new magnetic compilation produced for the present project. The sharp lateral change in velocity at mid-crustal levels that is interpreted as the COB (White et al., 2008; Roberts et al., 2009b) underlies the landward side of the seaward-

dipping reflectors (SDRs) on the iSIMM profile and coincides with the boundary between positive (oceanward) and negative (landward) magnetic anomalies (Figure 30). This can be compared with a similar analysis on the Hatton margin (Kimbell et al., 2005), where the COB was also identified to lie on the landward side of both a package of SDRs and a positive magnetic anomaly, which were interpreted as the signatures of oceanic crust formed subaerially during chron C24N. The difference between the two margins is that the Hatton margin contains an second package of SDRs which lie landward of the COB and are interpreted to be due to lavas erupted onto continental crust during chron C24R; there is no clear evidence for this package on the Faroese margin.

The COB was traced away from the iSIMM intersection using the magnetic mapping (Figure 30). The magnetic feature is fairly easily traced to the west, although alternative interpretations are possible on the south-east end of the Iceland-Faroe Ridge (cf. Figure 1). In the present interpretation, the COB simply cuts across the landward end of the ridge; in the alternative it would loop further oceanward along the landward flanks of major positive magnetic anomalies. Only limited magnetic data are available towards the north-east so the mapping of the COB is particularly speculative in this area, although it is corroborated by results from the MVM1 transect at the northern edge of the study area (Olaffson et al., 1992). The nature of this segment of the boundary will become better understood as a result of the recent aeromagnetic surveying by the Norwegian Geological Survey.

In addition to the inferred change in the average density of the crystalline crust between continental and oceanic areas, the model also included allowance for the high density intrusive bodies associated with volcanic centres. The density of the upper crustal layer was increased beneath these centres to values inferred from inversion of the associated positive gravity anomalies in preliminary model trials. The volcanic centres treated in this way, together with the other parts of the crustal density model, are shown in Figure 31. This included eight named centres and a further unnamed one lying to the north-west of the Brendan Volcanic Centre.

5.2 MODEL CALCULATION

The gravity modelling was conducted using the Gmod program (Dabek and Williamson, 1999), which employs wavenumber domain computation routines based on Parker (1972) and inversion methods after Oldenburg (1974).

1. A model that was in local isostatic equilibrium was constructed. This incorporated the components described in the preceding section together with the topography of the land areas. The Moho depth was adjusted, relative to a reference value of 30 km, to equalise the load at a compensation depth of 125 km.
2. A smoothed version of the isostatic Moho was used as an initial input for the model optimisation sequence described in the following steps. The smoothing was accomplished by a low-pass filter with a ramp between 80 km and 120 km. In subsequent model iterations, the Moho surface resulting from previous model optimisation, rather than the isostatic version, was used as the starting point - smoothing it with the same filter prior to re-running the optimisation.
3. An initial adaptation of the geometry of the Moho was undertaken by optimising its geometry on the basis of long-wavelength gravity variations, extracted using a low-pass filter with a ramp between wavelengths of 80 km and 133 km. At this stage the density of the crystalline crust was averaged (i.e. no division into upper and lower components).
4. The top basement interface was optimised on the basis of shorter wavelength residual gravity variations. A vertically averaged density model was used for the pre-Cenozoic part of the cover sequence. A low-pass filter with a ramp between 10 km and 20 km was

applied to the gravity field to avoid instability in the inversion and suppress features that might be associated with noise in the observations.

5. A more sophisticated pre-Cenozoic density model was adopted, stratifying this layer into seabed-parallel units to allow for compaction effects more accurately. The mid-crustal interface was introduced into the crystalline basement and mantle densities were recomputed.
6. A further optimisation of the Moho interface was undertaken, this time with the input field low-pass filtered using a ramp between 66 km and 100 km. A scaling factor was applied to the changes in Moho depth to accommodate the consequent movement of the mid-crustal interface.
7. The top basement interface was optimised again, employing the same low-pass filter as in step 5. Changes in the depth of this interface were scaled to reflect the difference between the local density contrast at the top basement surface and the average density contrast between pre-Cenozoic sediments and crystalline crust. This had the effect of dampening the model modification and suppressing instability.
8. Sedimentary and upper mantle densities were recomputed and the Moho and top basement optimisation was repeated as described in steps 6 and 7.
9. The final densities were assigned and gravity field calculated, and the model components were exported into GIS for imaging and analysis.

The input gravity field was shifted by -15 mGal to remove the regional positive gravity effect associated with the Iceland 'swell'. This correction incorporates both the influence of present-day dynamic support and the indirect effect (Chapman and Bodine, 1979) which reflects the difference between the datum adopted for the gravity measurements (the geoid) and that adopted for the gravity reference field (the spheroid).

The optimised model of depth to Moho is illustrated in Figure 32, and the thickness of crystalline crust in Figure 33. The influence of the modelling sequence on the thickness of the pre-Cenozoic sedimentary layer and the depth to top basement can be seen by comparing the initial versions (Figures 27 and 28) with the optimised versions (Figures 34 and 35). The total thickness of the cover sequence in the optimised model is shown in Figure 36. An apparent extension factor can be calculated from the modelled thickness of the crystalline crust relative to its sea-level reference value of 30 km (Figure 37). Departures from local isostasy are indicated by variations in the load calculated at 125 km relative to its reference value (Figure 38).

The calculated gravity field over the 3D model is imaged in Figure 39; the -15 mGal gravity shift has been subtracted from this to allow comparability with equivalent displays of the observed field (Figure 4). Residual gravity anomalies are illustrated in Figure 40. The RMS residual over the entire area is 2.88 mGal. Generally larger residuals occur over the oceanic area in the north-west corner because only the Moho modification affected this area. These residuals are potentially an indication of variations in the thickness of post-breakup sedimentary rocks that could be a target for further investigation. If the oceanic area is omitted from the calculation, the RMS residual is 2.49 mGal. Incorporation of intrusive igneous centres in the upper crustal model has reduced the impact of these centres on the residual gravity field effectively, although modest positive anomalies remain over the Fraenir, Darwin and Regin Smiður centres, suggesting that these may have a slightly higher density than was assumed.

6 Magnetic modelling

6.1 FORWARD MAGNETIC MODELLING

Forward magnetic fields were calculated for a model in which a simple magnetic structure was assigned to the units of the optimised gravity model. The crystalline crust was assumed to have a normal magnetisation (i.e. in the direction of the Earth's present field) of 1 A/m and the volcanic layer a reversed magnetisation of 3 A/m; the sedimentary units and the mantle were assumed to be non-magnetic. Given the complexity of the magnetisation contrasts within the basement and the Palaeogene igneous rocks, a magnetic field calculated in this way is unlikely to bear a strong resemblance to that observed, but the exercise is nonetheless useful in identifying the character of anomalies generated at different levels and in providing, at least locally, some independent corroboration (or refutation) of modelled features. The magnetic computations were done in the wavenumber domain using the Bmod program (Dabek and Williamson, 1999). No attempt was made to simulate the magnetisation structure of the oceanic crust.

The magnetic modelling results are illustrated in Figure 41. Observed (Figure 41a) and calculated fields in this figure have been upward-continued by 1 km to suppress the shortest wavelength features. Three versions of the calculated field are shown: combined basement and volcanic contributions (Figure 41b), basement contributions only (Figure 41c) and volcanic layer contributions only (Figure 41d). A common relief exaggeration factor is employed in each image, to give an indication of the relative contributions to the observed gradients, but the colour scales adapt to the amplitudes present in each case.

6.2 DEPTHS TO MAGNETIC SOURCES

Various methods are available for the automated computation of depths to magnetic sources, including Werner and Euler deconvolution and techniques that employ empirical solutions based on characteristics extracted from the shapes of individual anomalies. A relatively new innovation is to use the tilt-angle to estimate depths to magnetic sources, and this method has been applied, in its simplest form, to the magnetic data from the Faroe-Shetland region.

The tilt-angle is the arctangent of the ratio between the vertical and horizontal gradients of the magnetic field. This parameter has values of between -90° and +90° regardless of the amplitude of the anomaly, so is an effective way of applying equalisation to a magnetic field. Figure 42 is a colour-shaded image of the tilt-angle over the Faroe-Shetland area, based on a magnetic field that has been reduced to pole and upward continued by 1 km. Areas with poor magnetic data coverage have been omitted from this display.

Salem et al. (2007) showed that, with near-vertical contacts and employing the reduced-to-pole magnetic field, contours of the tilt-angle can be used to identify the locations and depths of magnetic sources. The location is indicated by the 0° contour and the depth by half the horizontal distance between the +45° and -45° contours.

Figure 43 shows the result of applying this method to the tilt-angle data displayed in Figure 42. The zone between the +45° and -45° contours is shown by a grey band (pale grey for negative angles and dark grey for positive angles) and along the zero line is plotted a set of colour-coded depth solutions based on the local distance between these contours and allowing for nominal sensor elevation and upward continuation. Solutions are omitted where the contour pattern is poorly defined or highly asymmetrical.

Initial inspection suggests that the depth solutions should only be regarded as semi-quantitative, providing a useful indication of relative source depths but requiring caution if used in more detailed analysis.

7 Analysis of results

7.1 METHODS

The model was examined by extracting profiles through it along seismic lines which provided independent evidence of deep crustal structure. These included deep wide-angle and normal incidence experiments such as iSIMM (Roberts et al., 2005; Parkin et al., 2007; Parkin and White, 2008; White et al., 2008; Roberts et al., 2009b), for which the comparison is shown in Figure 44. Comparisons were possible both in depth and two-way travel time, with the latter achieved by deriving the required algorithms from the velocity-depth relationships described in Section 3.3. Optionally, the time-depth relationships in the pre-Cenozoic sedimentary layer were modified to account for overcompaction, using the nominal offsets shown in Figure 14b. The latter were primarily geared towards the density modelling and may include compositional as well as compaction-related influences, so it is recognised that this is only an approximation when applied to velocity modelling. In practice depth to time conversions were conducted with and without the overcompaction correction and both versions compared with the independent control in order to assess the potential scale of its influence.

In addition to results from wide-angle experiments, the model was compared with time sections from BIRPS deep seismic reflection profiles (Klemperer and Hobbs, 1991; Snyder and Hobbs, 1999). As an example, Figure 45 superimposes interfaces from the 3D model on a line drawing of the NSDP84-3 profile (cf. Ritchie et al., 2011). The Moho was included in the depth to time conversion by assuming an average velocity of 6.5 km/s for the crystalline crust.

The time-converted optimised top basement surface from the 3D model was sampled at the shot point locations of the Faroe-Shetland Consortium seismic database and then imported into SeisWorks as a horizon that could be superimposed on sections displayed in that package's Seismic View. It was then possible to scan rapidly through the seismic lines in the database for evidence of the comparability of features in the gravity model with the seismic data. In the areas where seismic imaging was influenced by sills and volcanic rocks there was commonly very little seismic evidence of deeper structure, but this strategy maximised the opportunity for identifying glimpses of such structure that might otherwise have been missed. One such example is illustrated in Figure 46, which shows a seismic line from the northern side of the Faroe-Shetland Basin. Here there are indications of the pattern of pre-volcanic sediment thickness variation, but the combination with the gravity model enhances the confidence with which such features can be identified.

In addition to comparisons with seismic data, the model was compared systematically with images of the gravity and magnetic data and with the results of magnetic forward modelling and depth-to-source estimation described in Section 6.

7.2 EFFECT OF SILLS

Sensitivity trials were conducted to assess the potential influence of the Faroe-Shetland Sill Complex on the gravity models. The density anomaly associated with incorporating different cumulative thicknesses of sills in the upper 2 km of the pre-Cenozoic sequence within the Faroe-Shetland Basin was calculated using the formulas derived in Section 3.2. The integral of formula 3.1 was used to calculate the 'normal' average density, from which the density anomaly was calculated using formula 3.3. The envelope of the zone containing the sills was based on Smallwood and Maresh (2002) and Reynisson et al. (2009). The modelling indicates that each 100 m of sills generates a gravity anomaly of c. 1.6 mGal at these depths. There isn't an obvious signature in the observed gravity field that can be correlated with the mapped edge of the sill

zone, and the sensitivity trials indicate that one should have been detectable if there was a sharp change from no igneous material to several hundred metres of sills across this edge. It is likely that the distribution of igneous material is more complex and generates signatures that are more difficult to detect.

If it were possible to introduce a realistic simulation of the distribution of sills into the models, any compensating changes would occur at both top basement and Moho levels. The latter interface would absorb the longer-wavelength component and this would not entail a large displacement, given the size of the density contrast between crust and mantle (each 100 m of Moho displacement generates a gravity change of about 1.9 mGal). The assimilation of shorter wavelength variation at top basement level could introduce larger changes, particularly if the sills were present in the rocks adjacent to this boundary (as opposed to the case where topography on the basement surface interacts with an underlying, sill-free part of the cover sequence). The danger of reducing the density contrast across the top basement boundary, without strong supporting evidence, is that it increases the likelihood of the gravity inversion becoming unstable. For present purposes it was not considered practicable to introduce an *a priori* model that accurately reflected short wavelength variations in cumulative sill thickness and depth. The results of the trials were, however, used to inform analysis of model features and judge how incorporation of sills might modify the result.

7.3 MODEL OVERVIEW

The comparison with the iSIMM profile (Figure 44), provides a useful starting point for an assessment of the general features of the model, as this is a recent high-quality seismic experiment that traverses from oceanic crust across the Fugloy Ridge and into the central part of the Faroe-Shetland Basin.

The depth to Moho beneath the Norwegian Sea is on average about 1 km greater in the model than inferred from the seismic experiment, although the overestimate at the north-western end of the profile can be explained in part by an underestimate of sediment thickness in this area. As the continental margin is approached, the discrepancy changes polarity and increases, reaching a maximum beneath the oceanward side of the seaward-dipping reflector package and coinciding with the thick, high-velocity crust that underlies it. This discrepancy is not easily explained. If it was due to an underestimate of lower crustal density, the velocity contours indicate that the high densities should extend into the lower crust to the north-west and this would increase the discrepancy between seismic and gravity models in that area. Although the seaward-dipping reflectors are not associated with a positive velocity anomaly, it is possible that they are anomalously dense, as proposed by Korenaga et al. (2001). Increasing the density of this zone in the gravity model would lead to a compensating increase in the thickness of the underlying crust. An alternative explanation invokes lateral density variations in the underlying mantle. The modelling accounted for the effect of temperature but not for that of variable depletion, which also influences mantle density (Klein and Langmuir, 1987; Niu and Batiza, 1991; Kimbell et al, 2004). To explain the observations would require less depleted (higher density) upper mantle beneath the margin than beneath the oceanic crust to the north-west. This is counter-intuitive, given the thicker igneous crust produced at the time of breakup, and would require processes such as cycling of asthenosphere through the melting zone at that time and/or subsequent lateral transfer of melt into the area.

The modelled Moho beneath the Fugloy Ridge provides a good match to that interpreted from the seismic experiment (Figure 44). The implication of the relatively deep Moho is that any pre-basalt low-density sedimentary layer present beneath the ridge is thin, as has been shown in the latest iSIMM interpretations (e.g. Roberts et al., 2009b; Lau et al., 2009). The gravity modelling invokes short-wavelength variations in the thickness of this layer to explain residual gravity variations, although these could arise in part from inaccuracies in simulating the gravity expression of topography at shallower levels (top basalt and sea bed). The gradual tapering of the

low-velocity layer beneath the edge of the seaward dipping reflectors shown in the iSIMM model is a difficult target for investigation by the gravity method. Although crystalline crust is modelled to lie immediately beneath the thin low-density, pre-volcanic sediments, it is possible that this is a sedimentary layer that has a high density because of a high degree of intrusion and/or metamorphism (e.g. Eccles et al., 2009).

The modelled overall crustal thickness across the Faroe-Shetland Basin is in reasonable agreement with that interpreted from the iSIMM wide-angle seismic data, but there is rather poor correlation between the details of the modelled top-basement structure and the velocity model (Figure 44). In particular, the latter shows a depression in the velocity contours (i.e. a low velocity zone) where the gravity model places the south-eastern side of the Corona High. There is corroboration in the normal incidence reflection section for the modelled location of this margin (Figure 44), so it is possible that the limitation in this case is with the velocity modelling rather than the gravity modelling. Roberts et al. (2009b) noted that it was difficult to model the crustal structure beneath this part of the iSIMM profile. Although the sedimentary thickening in the Flett Basin at the south eastern end of the profile is corroborated by the seismic data, the two possible sub-basalt basins modelled farther to the north-west illustrate the challenge of gravity modelling in this region. Seismic evidence for these features is tenuous, at best, because of imaging problems associated with overlying igneous rocks. A significant portion of the observed gravity signal is due to the bathymetry and changes in the thickness of the post basalt sediments. For example a gravity gradient at 250 km can be correlated with the Faroe-Shetland Escarpment, but the modelled amplitude of the associated gravity feature is larger than that observed so the inversion has attempted to compensate for this by thickening the sub-basalt sedimentary layer on the seaward side of the escarpment and thinning it on the landward side. On the evidence of an individual profile, such features must necessarily be treated with great caution. The analysis process described in the following section involves looking at the overall form of the modelled features and comparing them with multiple sources of information (groups of seismic lines, magnetic data) in order to form a better assessment of the confidence with which they can be identified.

7.4 MORE DETAILED ANALYSIS

The following discussion includes abbreviations (in bold font) which refer to labelled features shown in Figures 47 and 48. The FSC Viewer (Appendix 3) provides a more interactive way of linking the discussion to images of the modelled features and other sources of evidence.

7.4.1 Faroe Platform - Fugloy Ridge - Møre Marginal High

There is a pronounced local gravity low centred about 20 km north-north-west of the island of Mykines (**MY** in Figures 47 and 48). The alternative magnetic compilation (Figure 8) reveals that this coincides closely with a zone of short wavelength, generally positive magnetic anomalies. The model inversion endeavours to explain the gravity feature in terms of a deep, sub-basalt basin, but this geometry fails to generate the observed gravity response (there is still a residual gravity anomaly of more than 20 mGal) and is regarded as unlikely. There are sufficient seismic lines in the area to rule out a post-basalt sedimentary thickening as the explanation (Figure 2). The preferred interpretation is that this anomaly is due to a low density, normally magnetised intrusive body of probable Palaeogene age. There are a number of felsic plutons in the conjugate part of the East Greenland margin that provide possible analogues (e.g. Tegner et al., 2008). The Greenland intrusions are syn- to (mainly) post-breakup in age and this would be compatible with the setting of the Mykines anomalies, which suggest a normally magnetised body intruded through the extrusive volcanic sequence. The Kangerlussuaq Alkaline Complex, for example, is also associated with a prominent positive magnetic anomaly (Riishuus et al., 2008), although those authors suggest that this is associated with an underlying mafic phase rather than the felsic (and presumably low density) components.

A local gravity anomaly low and positive magnetic anomaly on the north-east side of the Faroe Islands (**NEF**) is considered most likely to be due to a further low density, normally magnetised, felsic intrusive body of the type proposed near Mykines.

A conspicuous gravity low extends in a south-south-east direction along the axis of the Munkagrunnur Ridge (**MR)** and generates a thick apparent basin in the gravity model. Although an intrusive source for this anomaly cannot be entirely discounted it appears less likely than in the case of the Mykines and north-east Faroe anomalies. There is a clear spatial correlation between the Munkagrunnur feature and magnetic field variations, but the latter can be correlated with the structure and magnetostratigraphy of the overlying volcanic sequence rather than the magnetisation of a central intrusive body. The observed annular positive magnetic anomalies (Figure 8) can be correlated with the subcrop of normally magnetised units in the upper part of the Beinisvørð Formation that have been sampled onshore (Riisager et al., 2002) and traced in the offshore area by marine (Schrøder, 1971) and airborne (Ziska and Morgan, 2005) magnetic methods. The central gravity low coincides with a relative magnetic low, unlike the positive Mykines and north-east Faroes anomalies and is consistent with the erosional thinning of the normally magnetised units in the centre of the anticline. The gravity data indicate that within the core of this anticline, and beneath the high density volcanic sequence sampled in the Lopra borehole, lies a low density unit. A felsic intrusion might be expected to generate a relatively high heat flow and there is no evidence of that in the temperature measurements in the Lopra-1/1A borehole (Balling et al., 1984, 2006). It is considered more likely that the ridge is underlain by an inverted basin or perhaps particularly low density crystalline basement.

The modelled pre-volcanic sedimentary sequence is thin across the Fugloy Ridge (**FYR**). This was to some extent guided by the initial assumptions but it is compatible with the deep Moho detected by the iSIMM experiment.

Farther to the north-east there is evidence of sedimentary basins beneath the Møre Marginal High. In particular, a gravity low which extends north-west across the high (**MMB**; Figures 47 and 48**)** is interpreted in terms of a basin containing about 6 km of pre-volcanic sedimentary rocks. The associated gravity anomaly appears to extend north-westwards across the continent-ocean boundary, suggesting that the latter may be placed too far toward the south-east or that this extension relates to a feature at top basalt level that was not properly resolved in the seismic model.

7.4.2 Faroe Bank area

The Faroe Bank High is blanketed by volcanic rocks which, from the magnetic signatures at the edges of the high, can confidently be attributed a reversed magnetisation. The exception to this pattern is on the south-eastern part of the bank where there is a strong positive magnetic anomaly which correlates spatially with a local gravity anomaly low (**FBA** in Figures 47 and 48). This is considered most likely to indicate a felsic, normally magnetised igneous body which appears to have been intruded into the reversed polarity lavas.

A further positive magnetic anomaly in the Faroe Bank Channel can be correlated with the Regin Smiður Volcanic Centre (**RSVC**). In this case the associated gravity feature is positive, indicating a dense (c. 3 Mg/m^3), mafic intrusive body. The magnetic anomaly has an annular form and there are local changes in dip at top basalt level that appear to reflect this annulus. However the shallowest part of the volcanic sequence is reversely magnetised, as indicated by the anomalies generated nearby by its topography at the edge of the Munkagrunnur Ridge. The implication is that a normally magnetised intrusion has disrupted the overlying volcanic rocks but has not necessarily punctured right through them. The geophysical anomalies are not confined to this circular feature but extend towards the north-west, suggesting further intrusive material in that area.

When the gravity effect of bathymetry, post-volcanic sedimentary rocks and the underlying volcanic sequence in the Faroe Bank Channel Basin (**FBCB**) is subtracted from the observed field there is little indication of a residual negative effect in the central part of the basin that could be indicative of pre-volcanic sedimentary rocks. This is surprising, given the seismic evidence for layered reflectivity beneath the tentative base volcanic pick (see also Keser Neish and Ziska, 2005). The most likely explanation is that the deep fill of the Faroe Bank Channel Basin has a high density, probably because it contains a high proportion of extrusive or intrusive igneous material.

The model does indicate a thickening of the pre-volcanic sedimentary layer along the eastern side of the Faroe Bank High and extending into the northern part of the Faroe Bank Channel Basin (**NFBCB**). This coincides with the edges of a topographic feature and an area of thickened post-volcanic sediments, so it is possibly an artefact relating to shortcomings in simulating their gravity effect. The seismic and gravity data coverages do not appear particularly inadequate in this area, however. The feature wraps around the western side of the gravity and magnetic high that extends north-westwards from the Regin Smiður Volcanic Centre, so might indicate a part of the basin fill that was not modified by that igneous activity.

Farther south, the Faroe Bank Channel Knoll igneous centre (**FBCK**) is associated with positive gravity and magnetic anomalies. The polarity of the magnetisation could indicate emplacement at the same time as the Regin Smiður centre, although their geometries are different, with the Faroe Bank Channel Knoll requiring a broader body with a smaller density contrast or smaller depth extent. A mainly intrusive origin still appears more likely, though, as there is evidence of truncation of intra-volcanic reflectors at the margins of the complex.

7.4.3 North-east Rockall Basin and Wyville Thomson Ridge

The Drekaeyga (**DAVC**) and Darwin (**DVC**) volcanic centres align south-westwards from the Faroe Bank Channel Knoll (Figures 31a, 47 and 48). All three centres are associated with positive gravity effects indicative of an intrusive, mafic component, but a common intrusive chronology appears unlikely as the Darwin centre has reversed magnetic polarity in contrast to the normal polarity of Drekaeyga and Faroe Bank Channel Knoll. The postulated Sula Sgeir Volcanic Centre (**SGVC**), due east of the Darwin centre, is also reversely magnetised.

On seismic sections, the Auðhumla Basin (**AB**) appears to be a complementary syncline between the Wyville Thomson and Ymir anticlines. The post-volcanic sediments within the basin do not appear thick enough to explain the full amplitude of the gravity anomaly low over the basin, so the modelling has also invoked a thickening of the pre-volcanic sequence within it.

The model invokes a thicker pre-volcanic sedimentary sequence in the deepest part of the North-east Rockall Basin (**NERB**) than is interpreted from the AMP wide-angle seismic experiment (Klingelhöfer et al, 2005). This doesn't appear to be simply a function of the way the gravity effect is partitioned between the sedimentary and crystalline parts of the crust, as the thickness of crystalline crust is similar in the two models. The density assumed for the deeper part of the basin in the gravity model of Klingelhöfer et al. (2005) (2.4 Mg/m^3) is significantly lower than indicated by the shale compaction trend (Sclater and Christie, 1980) used in the present study.

The Dome Prospect of Archer et al. (2005) (**DP**) is resolved in the model as a distinct apparent basement high. This prospect was explored by the 164/07-1 well, which intersected Late Cretaceous mudstone intruded by numerous sills, interpreted to be associated with an underlying mafic intrusive body (Archer et al. 2005). The geophysical well logs demonstrate that the Cretaceous sedimentary rocks encountered in the well have an anomalously high density, presumably because of thermal metamorphism associated with the igneous activity, and this will also contribute to a positive gravity effect. Because the model endeavours to explain the gravity response in terms of a basement high, the magnetic field calculated from it (Figure 41) contains a positive anomaly over the prospect. If the intrusion postulated by Archer et al. was normally

magnetised it would be expected to generate an anomaly of this type. Archer et al. (2005), working with a more detailed magnetic dataset, did indeed find evidence for a normally magnetised intrusive body underlying reversely magnetised lavas. The evidence from our magnetic dataset is more equivocal, although this is admittedly on the basis of sparse observations (Figure 6). There is is a weak observed magnetic high but it is offset to the south-east of the computed feature (Figure 41). This might provide evidence of the influence of non-uniform and/or remanent magnetisation but more detailed interpretation is not justified without further observations.

The key to understanding the deep structure of the Wyville Thomson Ridge (**WTR**) lies in removing the gravity expression of topography at seabed and top volcanic levels with sufficient accuracy to leave signatures that can be interpretated meaningfully in terms of underlying structure. This can only be done with limited resolution in the current model given the distribution of data used in its construction and the relatively coarse (2 km) grids that define it. Smith et al. (2009) conducted more detailed modelling, but only along two profiles crossing the eastern side of the ridge (east of 8°W). Their results suggested that the thick pre-volcanic sediments of the North-east Rockall Basin may extend northwards as far as the axis of the ridge and then thin farther northwards beneath the Faroe Bank Channel Basin. The implication was that the ridge may have formed as the result of inversion of an underlying basin. The present 3D model echoes this configuration east of 8°W, but farther west the ridge coincides with a thinning of the pre-volcanic sequence. The magnetic modelling places some doubt on the robustness of the latter interpretation, as it predicts a conspicuous magnetic high to the west of 8°W, generated by a combination of thinning of reversely magnetised lavas and basement topography, and such a feature is not observed.

The model predicts a local thickening of the pre-volcanic sediments just north of the eastern end of the Wyville Thomson Ridge, beneath the south-eastern corner of the Munkur Basin (**MKB**). This feature is speculative, however, as it lies in an area where the topography of the top basalt surface was not well constrained (Figure 22). Farther north there is little evidence for low density sediments beneath the volcanic rocks of the Munkur Basin. As with the Faroe Bank Channel Basin to the north-west, it may be that the density of the deeper parts of the basin fill is influenced by high density igneous extrusive and/or intrusive rocks. The positive magnetic anomaly over the basin suggests that a substantial proportion of such rocks would have to be normally magnetised, and thus might be related to the Faroe Bank Channel Knoll centre to the north-west.

7.4.4 The Faroe-Shetland Basin

The Annika Sub-basin (**ANB**), on the eastern side of the Munkagrunnur Ridge and Faroe Platform has been interpreted by Keser Neish (2003) to have its primary seismic expression at sub-basalt level. The 3D model does indicate a thickening of the pre-volcanic sedimentary component of the basin (Figure 47), with depocentres near its northern and southern margins, although the thickened sequence does not extend as far west as the western boundary fault defined by Keser Neish (2003). The modelled eastern boundary of the basin is a linear, NNE-trending feature in its southern part, and the neighbouring high is associated with a positive magnetic anomaly, suggesting that this basement feature may influence magnetic field variations in this area. The high lies close to the Heri High of Keser Neish (2003) and Ritchie et al. (2011) but that was identified at shallower structural levels and the trends of the two features differ by about 20°.

The Annika Sub-basin is crossed by the ‘Annika Anomaly’, a positive magnetic feature that extends north-eastwards across the basin. Although it approximately parallels the structural highs that mark the south-east side of the basin, the anomaly is offset towards the north-west. In fact there is a correlation with the northern edge of the apparent southern compartment of the modelled basin (Figures 7 and 47). Previous attempts at modelling the source of the Annika

Anomaly have ranged from deep-seated intrusive bodies (Sweetman, 1997) to magnetisation variations within a relatively thin volcanic sequence (Smallwood et al., 2001). There is a magnetic step down towards the south-east along the length of the anomaly, upon which is superimposed a discrete magnetic high which is much more prominent in the south-west. A narrow, normally magnetised source would generate a magnetic low on its north-western side, which is not observed, and a better fit to the observations is provided if such a source extends towards the north-west. Given that there is solid evidence for normally magnetised units within the upper part of the Beinisvørð Formation on the Faroe Platform (see Section 7.4.1), it is persuasive to link the anomaly to the south-eastward truncation of such rocks. The parts of the anomaly where the discrete high has a larger amplitude are difficult is explain by a simple 'edge of sheet' effect suggesting that there may be a local thickening of the normally magnetised unit (and/or thinning of reversely magnetised units) in this area. The amplitude of the magnetic lows on the south-east side of the Annika Anomaly suggests thickening of the reversely magnetised part of the volcanic sequence in these areas.

The Annika Anomaly may therefore result from interactions between the normally and reversely magnetised parts of the volcanic sequence, complicating its interpretation. The implication of the above discussion is that the anomaly could mark the original location of a physical barrier that restricted the spread of the basalts at the time the normally magnetised sequence was being erupted (cf. Ellis et al., 2002). On this basis it would be expected that the volcanic rocks that extend farther to the south-east would be representatives of younger units that finally overspilled the barrier. There is, however, biostratigraphic evidence that suggests lavas of Beinisvørð Formation affinity do occur within the UK sector (205/9-1; Ellis et al., 2002), requiring eruption from a local vent or some other mechanism for by-passing the barrier if the hypothesis is to be sustained.

The Tróndur High (**TH**) and East Faroes High (**EFH**) have been mapped seismically as branching features with north-east to north-north-east trends (Figure 1; Keser Neish, 2003, 2005; Ritchie et al., 2011). There is generally a reasonable correspondence between these and highs at top basement level in the 3D model (Figure 48). This starts to break down, however, at the north-eastern end of the East Faroes High, north-east of the Grimur Kamban Lineament (Ritchie et al., 2011; Figures 1 and 49), where the modelled feature lies to the east of the trace indicated by previous mapping. There is some corroboration for the new interpretation from the magnetic observations, as these show a magnetic high which coincides with the anomaly predicted from forward magnetic modelling of the basement structure (Figure 41). Farther to the north-west, basement magnetic signatures appear to be swamped by those associated with the overlying volcanic rocks, so this may be one of the most westerly sub-basalt features in the basin that is amenable to joint gravity and magnetic analysis.

The Grimhild (**GB**) and Steinvør (**STB**) sub-basins were identified as apparent Mesozoic basins by Keser Neish (2003). Pre-volcanic sedimentary thickening is predicted in these areas by the 3D model, which provides more insight into their geometry. The depocentre of the Steinvør Basin is offset south-westwards from the previous mapping, in line with the relocation of the northern limb of the East Faroes High. Both basins are aligned along a north-north-east trend, and their forms suggest dextral dislocations across north-west-trending ?transfer faults, particularly the Corona and Grimur Kamban lineaments (Ritchie et al., 2011; Figure 49).

The Guðrun Sub-basin (**GDN**) is poorly defined by seismic data (Ritchie et al., 2011), but is the site of substantial pre-volcanic sedimentary thickening in the 3D model. The north-north-east trend of the basin echoes that observed in the Annika, Grimhild and Steinvør sub-basins to the west and contrasts with the more easterly trend of the sub-basins farther east, although the latter trend may influence the northern part of the basin.

To the south of the Guðrun Sub-basin lies the Mid Faroe High (**MFH**), which is poorly defined seismically (Ritchie et al., 2011) but conspicuous in the gravity data and the 3D model. There is a clear correspondence with a magnetic anomaly in the east, at the junction with the Corona High

but only a weak positive magnetic response over its central part. The structural elements map of Ritchie et al. (2011) (Figure 1) shows the high swinging northwards between the Grimhild and Guðrun sub-basins in the west and this is reflected in the 3D model.

The modelled western margin of the Brynhild Sub-basin (**BB**) approximately aligns with the north-north-east-trending western margin of the Annika Sub-basin. When combined with the west-north-west trend of its northern margin against the Mid Faroe High and the east-north-east trend of its southern margin against the Sjúrður Ridge (**SR**), this gives the basin a distinctive triangular form. The Sjúrður Ridge trend forms a clear lineament in the top basement map (Figure 48), although this does cross-cut the Judd Lineament (Figure 49). To the west of the Brynhild Sub-basin lies the Fraenir Volcanic Centre (**FVC**), and comparison of the density model for that centre with the magnetic mapping suggests that it is predominantly reversely magnetised.

The Judd Sub-basin (**JB**) and northern part of the Judd High (**JH**) have been extensively explored by seismic methods and it is unlikely that a relatively low resolution gravity model will provide significant new insights in this area. The modelling does reveal an apparent co-linearity between the deepest part of the Judd Sub-basin and the Guðrun Sub-basin to the north. As noted by Ritchie et al. (2011), the northern part of the Westray High (**WH**) is well resolved by gravity and magnetic data, but farther south the correspondence between potential field and seismic features is less exact. In the latter area there is little magnetic indication of the high and the associated gravity feature (as reflected in the 3D model) is offset slightly to the east of that mapped seismically (e.g. Ritchie et al., 2011).

The Corona High (**CH**; Figures 47 and 48) forms a prominent gravity and magnetic feature in the central part of the Faroe-Shetland Basin. In the south there is a good correspondence between gravity (as reflected in the 3D model), magnetic and seismic expressions of the high, but these become less well aligned as the feature is traced north-eastwards. The first conspicuous change is a marked northward reduction of the amplitude of the magnetic anomaly (Figure 7), which occurs across the postulated Corona Lineament (Ritchie et al. 2011). The most likely explanation for this is a change in the basement magnetisation, perhaps associated with the juxtaposition of crystalline and metasedimentary basement units. A similar magnetisation reduction can be seen where this lineament crosses the Rona High to the south-east, although magnetic basement does reappear on the north side of the lineament in the northernmost part of the West Shetland High. To the north of the Corona Lineament, the gravity expression of the Corona High starts to deviate to the east of the seismically defined feature and the attenuated, but still distinct, magnetic expression. The reason for this is not known but, given the potential amplitude of gravity anomalies associated with the Faroe-Shetland Sill Complex (Section 7.2), it is possible that this could distort the gravity expression of the northern part of the Corona High.

The Corona Sub-basin (**CB**) is shown as a relatively large feature by Ritchie et al. (2011), but they note that it is poorly imaged by seismic data because of the effect of the overlying volcanic rocks. The 3D model provides some interesting insights into this basin. A distinct basement high is modelled between it and the Guðrun Sub-basin to the south. The basin appears to have two limbs, one extends in a north-north-east direction towards the western end of the Erlend Basin and the second has an east-north-east trend and appears to link to a hiatus in the Corona High.

Gravity images (e.g. Figure 5) suggest that the Erlend High (**EH**) may extend eastwards across the Faroe-Shetland Basin, but there has been little supporting seismic evidence for this. The new 3D model provides some indication of such a feature at top basement level (Figure 48), but also contains elements of the north-eastward structural grain that is more traditionally mapped in this part of the basin. In particular, there is an apparent northward extension of the Corona High (**NCH**) which has a north-eastward trend and is corroborated by seismic evidence. The model suggests a feature with a similar form centred about 25 km to the north-west but in that case the support from seismic imaging is weaker.

The Flett High is not well resolved by the 3D model, in which the Flett and Foula sub-basins appear to merge in a single, pronounced, north-east-trending depocentre (**FLB**). The clearest potential field indication of the high is in the magnetic tilt derivative (Figure 42), which amplifies the weak signal that is present. Within the gravity data, the most prominent hiatus along the basin axis can be correlated with a distinct circular feature (**CF**) identified by Robinson et al. (2004) in 3D seismic data and interpreted by them as evidence for an igneous intrusion. An igneous origin is certainly possible on the basis of the modelled apparent basement high, although it is not associated with a clear magnetic response.

A substantial sedimentary thickness is predicted in parts of the Erlend Sub-basin (**EB**), with a pronounced local pre-Cenozoic thickening occurring immediately north of the Erlend High (Figure 47). Such a feature was not presaged by the starting model (Figure 27) and is a response to a local isostatic gravity anomaly low. It is possible, however, that the inversion has become unstable in this area and overestimated the basin thickness. This could have been triggered by distortion associated with the proximity of major positive gravity features associated with the Brendan and Erlend volcanic centres and exacerbated by the small density contrast at top basement level at greater optimised thicknesses. In contrast, a large area in the western part of the basin is predicted to contain less than 1 km of pre-Cenozoic sediments. This coincides with an area where the post-volcanic sedimentary sequence is thickest, and apparently sufficient to explain much of the required negative gravity effect. The gravity variations across the basin appear too large to be explained by changes in cumulative sill thickness, although the latter could introduce distortion.

A local sedimentary thickening is predicted beneath the Pilot Whale Anticline (**PWB**), a north-north-east trending feature at the northern extremity of the Erlend Sub-basin. The axis of the anticline (as defined, for example, at top volcanic level (Figure 24)) coincides with that of the predicted basin in the north but with the basin's eastern margin in the south. Model features such as this could arise because of inaccuracy in simulating the gravity effect of the overlying structure, but there is some corroboration for it from the seismic database. One possible explanation is that there is a Mesozoic basin beneath the anticline, and the latter formed because of Cenozoic compressional reactivation of the structures controlling that basin. The offset in the basin's axis coincides with an area where mud mounds are observed at the sea bed (Ritchie et al., 2003). A further offset beneath the northern end of the anticline coincides with the Brendan lineament of Ritchie et al. (2011) (Figure 49).

The upper crustal density anomaly required to explain the gravity effect of the Brendan Volcanic Centre (**BVC**) coincides with a sharp magnetic low (Figures 7 and 31a), indicating that at least the core of the associated intrusion is reversely magnetised. The density model includes a second centre about 40 km to the north-west, although in this case its magnetisation is less clear, perhaps because of masking by effects associated with the overlying lavas. These features lie within an area identified by Rohrman (2007) as being dominated by intrusive complexes and having a higher exploration risk.

7.4.5 The Møre Basin

The gravity inversion has introduced substantial variations in the thickness of the Pre-Cenozoic sediments in the Møre Basin (**MB**; Figure 47). The initial model for this basin was relatively poorly constrained so some distortion may result from inaccurate modelling of shallower structure, particularly in areas with volcanic cover. A north-east-trending basement high (**MB1**) is predicted to underlie the basalt in the southern part of the basin. A second high (**MB2**) lies 35 km south-east of the southern end of this feature and parallels its trend. MB1 has no clear magnetic expression but MB2 is associated with a weak positive magnetic anomaly.

Farther north, on the projection of MB1 lies a further modelled intra-basin high (**MB3**), which is marked by both gravity and magnetic highs, although the latter is offset to the east of the former. The features coincide with an apparent structural high on the MVM1 seismic transect (Olafsson

et al., 1992) and (approximately) with one of the magnetic anomalies Lundin and Doré (2002) have interpreted to be caused by Early Cretaceous seamounts. The pronounced sedimentary thickening modelled to the east of this feature is corroborated by the MVM1 velocity model.

At the eastern edge of the study area the Møre Basin is crossed by a north-east-trending chain of positive magnetic anomalies (compare **MB4** in Figure 48 with Figure 7), which Lundin and Doré (2002) associated with Early Cretaceous seamounts formed along the axis of the basin during a major rifting event. This chain can be correlated with apparent basement highs in the model, and the magnetic anomalies calculated over these features and the thick sedimentary axis on their south-east side compare well with the observations (Figure 41).

The southern margin of the Møre Basin is formed by a series of structural highs: Margarta's Spur (**MS**; an extension of the East Shetland High), the Manet High (**MAH**) and the Møre-Trøndelag Fault Complex (**MTF**) (Blystad et al., 1995). These features are well-resolved by the gravity model. Just to the south lie the Magnus (**MGB**) and Marulk (**MAB**) basins, which are modelled to have a very thick sedimentary fill (top basement lying at depths in excess of 10 km). Nøttvedt et al. (2000) describe these basins as essentially an extension of the Møre Basin, and there is some support for this argument from the modelled geometry, which reflects north-east trending structural control rather than the north- to north-north-east grain that characterises the Northern North Sea. There is also evidence of structures linked to the basement domain to the south, however, because a north-north-east-trending magnetic anomaly can be traced from that area towards the high between the two basins (Figure 7), and appears to be truncated at the lineament which marks their northern edge.

7.4.6 Northern North Sea

The Northern North Sea is not a primary target for the present investigation, but it is encouraging that the modelling methodology has resolved features in this area that are corroborated by seismic data that were not employed in the initial model construction. Comparison with the BIRPS deep seismic profiles, for example, reveals good correlations with seismic imaging of the cover sequence and lower crustal reflectivity (e.g. Figure 45).

Comparison can be made with structural elements mapped by the Norwegian Petroleum Directorate, which can be downloaded as a shapefile from:
http://www.npd.no/en/Topics/Geology/Temaartikler/Structure-elements/
There are good correlations with mapped features that were not well-resolved by the starting model (compare Figures 28 and 48). These include the Tampen Spur (**TS**) and Tjalve Terrace (**TT**) in the north and a series of sub-basins along the Viking Graben: the Runge (**RB**), Fensal (**FEB**), Vana (**VAB**) and Vilje (**VIB**) sub-basins. Farther west, sedimentary thickening is also modelled in the East Shetland Basin (**ESHB**) and Beryl Embayment (**BE**).

7.4.7 West Lewis - Orkney - Shetland area

This is the triangular area on the south side of the model, characterised by generally shallow basement (Figure 48). A problem with modelling in this area concerns how to classify the Devonian sedimentary rocks. Seismic imaging reveals a thick Devonian sequence in places, but the density contrast between these rocks and the underlying basement is likely to be small (Holloway et al., 1991). No attempt was made to incorporate the Devonian strata in the initial cover sequence model, and this will lead to their presence largely being suppressed in the final model. Local thickening of low density Devonian rocks will have generated some modelled sedimentary thickening, but longer wavelength features will have been absorbed at Moho level, with a modest overestimate of Moho depth possible if these sediments are appreciably less dense than the underlying basement.

The influence of Devonian and older (meta)sedimentary rocks is evident in the magnetic field. Where crystalline basement lies at shallow depth, in the north and west of the area, high

amplitude magnetic anomalies are observed; in other areas, where such basement is nominally shallow but includes, for example, Moine and/or Devonian rocks, the magnetic field variations are subdued (compare figures 41a and 41b).

In the west the model resolves a thick sedimentary sequence in the West Lewis Basin (**WLB**) with a linear, probably faulted north-east-trending western margin against the West Lewis High (**WLH**).

The North Lewis Basin (**NLB**) is modelled to be more than 5 km deep along a north-south axis, which is truncated to the north by the axis formed by the East and West Rona intrabasinal highs of Ritchie et al. (2011). The part of the North Lewis Basin to the north of these highs is modelled to have relatively thin (1 - 2 km) fill.

The modelled sediment thickness in the north-east-trending North Rona Basin (**NRB**) compares satisfactorily with the well and seismic evidence and the similarly trending Solan Bank High (**SBH**) is clearly resolved by the model and also by its magnetic response.

A variable sedimentary thickness characterises the West Orkney Basin (**WOB**), with maximum values in a north-western compartment and three further shallower rifts to the south and east which have similar north-east trends. The subcrop of the Moine Thrust may run between these features and have influenced the evolution of the basin (see Ritchie et al., 2011).

The West Shetland Basin (**WSHB**) and flanking Rona High (**RH**) are particularly well resolved by the combination of the gravity modelling and magnetic imaging. Offsets in the magnetic anomaly associated with the shallow crystalline basement beneath the Rona High provide clear evidence for the location of transfer faults affecting the Faroe-Shetland Basin to the north-west. The impact of these structures on the modelled eastern margin of the West Shetland Basin (against the Papa and West Shetland highs) and its associated magnetic anomalies is far less obvious, although there is perhaps a small offset on the projection of the Corona Lineament. This implies that the pinline for transfer movements lies along east side of the West Shetland Basin, and contrasts with the situation farther north, where the lineaments influencing the northern part of the Faroe-Shetland Basin appear to extend south-eastwards across the East Shetland High (Figure 1; Ritchie et al., 2011).

The Unst Basin (**UB**) is a Y-shaped feature which is considered by Johns and Andrews (1985) to have been formed by Permo-Triassic rifting controlled by intersecting Caledonian faults. The model indicates a thicker basin fill in the north-western arm of the basin, compared with those to the north-east and south, and this is compatible with the observed presence of additional Jurassic to Early Cretaceous sediments in that part of the basin. Magnetic data indicate a distinct north-east-trending magnetisation boundary along the south-east side of the basin, with shallower magnetic rocks towards the south-east (Figure 7), but the feature is more linear than the basin margin and extends over a greater distance so it is interpreted to be associated with intra-basement magnetisation contrasts rather than those between cover and basement.

The West Fair Isle Basin (**WFIB**) lies along major basement structures (the Great Glen and Walls Boundary faults) which also have a clear magnetic expression (Figure 7). This generally takes the form of a deepening of the magnetic component of the basement from west to east although the sense is opposite at the northern, deepest part of the basin. The siting and form of the basin have clearly been strongly influenced by these structures. It is modelled to contain up to about 4 km of sediments along much of its length, increasing to 6 km at its northern end. Comparison with seismic reflection data suggests that these could be overestimates, even allowing for the influence of overcompaction on rock velocity (Figure 45).

The modelled forms of the East Orkney (**EOB**) and East Fair Isle (**EFIB**) basins suggest that they are controlled by north-west-trending structures, and the magnetic data provide evidence of the existence of this trend within the underlying basement. Gravity and magnetic anomalies and a modelled sedimentary thickening suggest features with a similar trend extending south-eastwards from Shetland. In contrast, the form of the Dutch Bank Basin (**DBB**) suggests control

by north-south structures, parallel to those which have influenced the Beryl Embayment to the east.

8 Conclusions and recommendations

The new three-dimensional model confirms the structural complexity of the Faroe-Shetland region. Previous mapping (e.g. Keser Neish, 2003; Ritchie et al., 2011) has identified a large number of sub-basins and structural highs within the region. The new model (Figures 47 and 48) corroborates and adds to this collection and provides new detail to our understanding of the geometry of the individual elements. The analysis of trends has a chequered history, and does run the risk of overinterpretation, but there do seem to be several 'grains' present which suggest that the complexity in the cover sequence may relate to complexity in the underlying basement.

On the west side of the Faroe-Shetland Basin a north-north-east trend can be seen in the Grimhild, Guðrun and Steinvør sub-basins, and also appears to affect the southern Annika Sub-basin and Judd Sub-basin. More distantly, there are echoes of it on the eastern margin of the north-east Rockall Basin and western margin of the Møre Basin. Cross-cutting this is an east-north-east trend that can be seen, for example, in the eastern arm of the Corona Sub-basin, the northern Annika Sub-basin and southern margin of the Brynhild Sub-basin. Although the subdivision is subtle, the north-east trend of the Flett-Foula axis does appear distinct from the north-north-east and east-north-east orientations and to be reflected in the northern arm of the Corona Basin. Cutting across all these is the broadly north-westward 'transfer' trend, which is the subject of ongoing debate (e.g. Moy and Imber, 2009). Such a trend is undeniable in the major transfer between the Faroe-Shetland and North-east Rockall basins, which appears to be effected across a complex of structures spanning the Westray, Judd and Wyville Thomson lineaments (Figures 1 and 47; Kimbell et al., 2005). Farther north the mapping of such structures is more ambiguous and open to alternative interpretations (compare Figure 1 with Rumph et al., 1993). The new model does contain many offsets which coincide with the lineaments of Ritchie et al. (2011), as illustrated by Figure 49, but the two interpretations are not entirely independent as gravity imagery contributed to the original lineament identification.

The model has been constructed in such a way that it should be straightforward to update as new information becomes available, either as a result of feedback from Faroe-Shetland Consortium (FSC) members or from new data acquired during the course of the consortium's work programme. The structural components were assembled in ArcGIS, and integration of different data sources was achieved using ModelBuilder applications, which can be re-run if any of the sources are changed. The modelling routines have been saved as a linked series of Unix scripts that can be refined and re-run as required.

The model could be used to update the structural elements map of the area and should inform future FSC projects, for example helping to indentify structural control over the siting of Cenozoic deformation and assessing the geodynamic influences on, and effects of, that deformation. It could form the basis for more focussed studies within particular subareas incorporating more detailed modelling. For example the northward extension of the Corona High and the internal structure of the Erlend Sub-basin are worthy of further investigation, given the exploration potential of these currently poorly understood areas. The physical property analysis described here has provided a framework for quantification of the influence of the Faroe-Shetland Sill Complex on the inferred structure of the basin but this needs to be pursued in more detail over specific targets. As the 3-D seismic imaging of the complex develops, the scope for direct forward modelling of its associated potential field responses improves.

On a broader scale, there is considerable scope for obtaining geodynamic and thermal insights from the modelling results. There are clear patterns in the mapped departures from isostatic equilibrium that warrant analysis in terms of the interplay of different mechanisms (e.g. sediment loading, extensional and compressional deformation, lithospheric folding) within the context of spatially and temporally varying lithospheric strength. The modelled geometries can be used to

compute maps of predicted present-day heat flow and sub-surface temperature which can be compared with estimates derived from corrected bottom hole temperatures. The influence of denudation on rock properties identified in the well log analysis could be followed up in more detail, refining the estimates by reference to rock lithologies, calibrating against other methods (e.g. fission track), and considering the implications of the results in terms of basin evolution and prospectivity.

The igneous components of the model would benefit from closer examination. The initial attempt to simulate the gravity response over the mafic intrusive components of the volcanic centres has proved effective and could be followed up with more detailed gravity and magnetic modelling. The proposed felsic intrusive centres would provide good targets for follow-up studies and, potentially, shallow drilling. The magnetic signatures over the extrusive sequences are complex but there are clear patterns that would be amenable to modelling. In particular, the normally magnetised units that crop out on the Munkagrunnur Ridge, and are implicated in the Annika Anomaly, would be amenable to three-dimensional magnetic modelling. Having a better understanding the magnetostratigraphy of the volcanic sequences in this region could have an important impact on exploration. If it is known, for example, that only reversely magnetised units are present in a particular area, then the magnetic anomaly pattern can be analysed directly for indications of variations in the thickness of that sequence that would clearly be important when considering options for drilling. The magnetostratigraphy can be investigated using the magnetic responses over subcropping, dipping volcanic units and the anomalies associated with volcanic topography (e.g. at escarpments or faulted offsets), as well as by further sample measurements.

Finally, the work of the FSC provides an opportunity for developing new ways of presenting multiple sources of information and interpretation in order to enhance the user's ability to recognise their implications and connections. The FSC Viewer (Appendix 3) provides one vehicle for doing this and there is scope for further development in this area.

Appendix 1 Structural element abbreviations

The following abbreviations are used in the structural elements map of Ritchie et al. (2011), which appears in Figure 1 and in the FSC Viewer (Appendix 3). Note that the abbreviations are also identified when the mouse pointer is moved over the labels in the Viewer.

AB	Auðhumla Basin
ANB	Annika Sub-basin
BB	Brynhild Sub-basin
BL	Brendan Lineament
BVC	Brendan Volcanic Centre
CB	Corona Sub-basin
CH	Corona High
CL	Clair Lineament
CLB	Clair Basin
COL	Corona Lineament
DAVC	Drekaeyga Volcanic Centre
DGH	Darwin-Geikie High
DVC	Darwin Volcanic Centre
EB	Erlend Basin
EFH	East Faroe High
EFIB	East Fair Isle Basin
EH	Erlend High
EL	Erlend Lineament
EOB	East Orkney Basin
ERH	East Rona High
ESB	East Solan Basin
ESH	East Shetland High
EVC	Erlend Volcanic Centre
FB	Fetlar Basin
FBCB	Faroe Bank Channel Basin
FBCK	Faroe Bank Channel Knoll
FBH	Faroe Bank High
FH	Flett High
FLB	Flett Sub-basin
FOB	Foula Sub-basin
FP	Faroe Platform
FVC	Frænir Volcanic Centre
FYR	Fugloy Ridge
GB	Grimhild Sub-basin
GDN	Guðrun Sub-basin
GFT	Grani Fault Terrace
GGF	Great Glen Fault
GKL	Grímur Kamban Lineament
HH	Heri High
IFR	Iceland-Faroe Ridge
JB	Judd Sub-basin
JF	Judd Fault
JH	Judd High
JL	Judd Lineament
MAH	Manet High
MB	Møre Basin
MF	Melby Fault
MFH	Mid Faroe High
MGB	Magnus Basin
MIF	Minch Fault
MKB	Munkur Basin
ML	Magnus Lineament
MMH	Møre Marginal High
MR	Munkagrunnur Ridge
MT	Moine Thrust
NB	Norwegian Basin
NERB	North-east Rockall Basin
NF	Nesting Fault
NFBCB	North Faroe Bank Channel Basin
NFF	North Flett Fault
NLB	North Lewis Basin
NRB	North Rona Basin
NRSSH	Nun Rock-Sule Skerry High
NSH	North Shoal High
OBF	Otter Bank Fault
OHH	Outer Hebrides High
OSH	Orkney-Shetland High
PB	Papa Basin
PBH	Pobie High
PH	Papa High
RF	Rona Fault
RH	Rona High
RSVC	Regin Smiður Volcanic Centre
SB	Sandwick Basin
SBH	Solan Bank High
SFF	South Flett Fault
SGVC	Sula Sgeir Volcanic Centre
SMBB	St Magnus Bay Basin
SR	Sjúrður Ridge
SSB	South Solan Basin
SSF	Shetland Spine Fault
SSH	Sula Sgeir High
STB	Steinvør Sub-basin
TH	Tróndur High
UB	Unst Basin
VL	Victory Lineament
WBF	Walls Boundary Fault
WEVC	West Erlend Volcanic Centre
WF	Westray Fault
WFIB	West Fair Isle Basin
WH	Westray High
WL	Westray Lineament
WLB	West Lewis Basin
WLH	West Lewis High
WOB	West Orkney Basin
WRH	West Rona High
WSB	West Solan Basin
WSH	West Shetland High
WSHB	West Shetland Basin
WTLC	Wyville Thomson Lineament Complex
WTR	Wyville Thomson Ridge
YR	Ymir Ridge

Appendix 2 GIS components

GEOPHYSICAL IMAGES

The following georeferenced geophysical images are provided (in the 'fsc_geophys_images' folder). Colour scales to accompany these images are included in the 'colour_scales' sub-folder. The naming convention for these reflects the 'type' component of the name of the main image. For example the colour scale for 'fsc_ba220_cn.jpg' is 'ba220.jpg'.

Gravity and topographic images	
fsc_ba220_cn.jpg	Bouguer gravity anomaly with reduction density of 2.20 Mg/m^3. Colour shaded-relief with illumination from the north.
fsc_ba275_cn.jpg	Bouguer gravity anomaly with reduction density of 2.75 Mg/m^3. Colour shaded-relief with illumination from the north.
fsc_faba_cne.jpg	Free-air gravity anomaly (Bouguer onshore). Colour shaded-relief with illumination from the north-east.
fsc_faba_cnw.jpg	Free-air gravity anomaly (Bouguer onshore). Colour shaded-relief with illumination from the north-west. (Figure 4 in this report).
fsc_ghg_cn.jpg	Horizontal gradient of the free-air gravity anomaly (Bouguer onshore). Colour shaded-relief with illumination from the north.
fsc_g1vd_cn.jpg	First vertical derivative of the free-air gravity anomaly (Bouguer onshore). Colour shaded-relief with illumination from the north.
fsc_gisos_cne.jpg	Isostatically corrected Bouguer gravity anomaly. Calculated assuming an upper crustal density of 2.75 Mg/m^3 and a density contrast across the Moho of 0.4 Mg/m^3. Colour shaded-relief with illumination from the north-east.
fsc_gisos_cnw.jpg	Isostatically corrected Bouguer gravity anomaly. Calculated assuming an upper crustal density of 2.75 Mg/m^3 and a density contrast across the Moho of 0.4 Mg/m^3. Colour shaded-relief with illumination from the north-west. (Figure 5).
fsc_gisoshp_cne.jpg	High-pass filtered isostatically corrected Bouguer gravity anomaly. Calculated assuming an upper crustal density of 2.75 Mg/m^3 and a density contrast across the Moho of 0.4 Mg/m^3. The filter had a cosine taper between wavelengths of 150 km and 200 km. Colour shaded-relief with illumination from the north-east.
fsc_gisoshp_cnw.jpg	High-pass filtered isostatically corrected Bouguer gravity anomaly. Calculated assuming an upper crustal density of 2.75 Mg/m^3 and a density contrast across the Moho of 0.4 Mg/m^3. The filter had a cosine taper between wavelengths of 150 km and 200 km. Colour shaded-relief with illumination from the north-west.
fsc_gr10_cne.jpg	Residual free-air gravity anomaly (Bouguer onshore). Calculated by subtracting a 10 km upward continuation. Colour shaded-relief with illumination from the north-east.
fsc_gr10_cnw.jpg	Residual free-air gravity anomaly (Bouguer onshore). Calculated by subtracting a 10 km upward continuation. Colour shaded-relief with illumination from the north-east.
fsc_gravlines.jpg	Locations of gravity observations (Figure 3 of this report)

fsc_gup10_cn.jpg	Regional free-air gravity anomaly (Bouguer onshore). Calculated by upward continuation by 10 km. Colour shaded-relief with illumination from the north.
fsc_topo_conts.jpg	Topographic contours at 200 m intervals (Figure 10)
fsc_topo_eqint_cv.jpg	Topography: colour image with vertical illumination
Magnetic images	
fsc_m1vd_cn.jpg	First vertical derivative of the total magnetic field. Colour shaded-relief with illumination from the north.
fsc_mag_cne.jpg	Total magnetic field. Colour shaded-relief with illumination from the north-east.
fsc_mag_cnw.jpg	Total magnetic field. Colour shaded-relief with illumination from the north-west. (Figure 7)
fsc_maglines.jpg	Locations of magnetic observation points
fsc_magmerge_cne.jpg	Total magnetic field: alternative compilation. Colour shaded-relief with illumination from the north-east.
fsc_magmerge_cnw.jpg	Total magnetic field: alternative compilation. Colour shaded-relief with illumination from the north-west. (Figure 8).
fsc_mhg_cn.jpg	Horizontal gradient of total magnetic field. Colour shaded-relief with illumination from the north.
fsc_mr10_cne.jpg	Residual reduced-to-pole magnetic anomaly. Calculated by subtracting a 10 km upward continuation. Colour shaded-relief with illumination from the north-east.
fsc_mr10_cnw.jpg	Residual reduced-to-pole magnetic anomaly. Calculated by subtracting a 10 km upward continuation. Colour shaded-relief with illumination from the north-west.
fsc_mup10_cn.jpg	Regional reduced-to-pole magnetic anomaly. Calculated by upward continuation by 10 km. Colour shaded-relief with illumination from the north.
fsc_pseud_cn.jpg	Pseudogravity anomaly. Colour shaded-relief with illumination from the north.
fsc_pseudhg_cn.jpg	Horizontal gradient of pseudogravity anomaly. Colour shaded-relief with illumination from the north.
fsc_pseudhp_cne.jpg	High-pass filtered pseudogravity anomaly. The filter had a cosine taper between wavelengths of 150 km and 200 km. Colour shaded-relief with illumination from the north-east.
fsc_pseudhp_cnw.jpg	High-pass filtered pseudogravity anomaly. The filter had a cosine taper between wavelengths of 150 km and 200 km. Colour shaded-relief with illumination from the north-west.
fsc_rtp_cne.jpg	Reduced-to-pole magnetic anomaly. Colour shaded-relief with illumination from the north-east.
fsc_rtp_cnw.jpg	Reduced-to-pole magnetic anomaly. Colour shaded-relief with illumination from the north-west.
fsc_tilt_deriv.jpg	Tilt derivative of the magnetic field after upward continuation by 1 km and reduction to pole. Colour shaded-relief with illumination from the north. (Figure 42).
fsc_tilt_depths.png	Colour coded tilt-depth estimates superimposed on a background showing tilt angles of -45° to 0° in pale grey and 0 to +45° in dark grey. (Figure 43).

MODEL IMAGES

The 3D model is presented as a series of georeferenced colour contour maps (in the 'fsc_model_images' folder). In many cases there are two versions of the file - one without contour labels and one with automatically generated labels (denoted by an additional '_lab' in the filename). The relevant colour scales can be found in the 'colour_scales' sub-folder.

Model images	
basdenshift.jpg	Density shift applied to the volcanic layer (Figure 15b in this report)
basthk.jpg	Thickness of the volcanic layer, contoured at 0.5 km intervals (Figure 25)
calcmag_basement_up1.jpg	Calculated magnetic field: just basement component (Figure 41c)
calcmag_lavas_up1.jpg	Calculated magnetic field: just volcanic component (Figure 41d)
calcmag_up1.jpg	Calculated magnetic field: basement and volcanic components (Figure 41b)
cover.jpg	Optimised total cover sequence thickness, contoured at 1 km intervals (Figure 36)
crysthk.jpg	Optimised thickness of crystalline crust, contoured at 2 km intervals (Figure 33)
den_lc.jpg	Density of the lower crust (Figure 31b)
den_uc.jpg	Density of the upper crust (Figure 31a)
exfac.jpg	Apparent crustal extension factor (Figure 37)
grav_calc.jpg	Calculated gravity field. Colour shaded-relief, illuminated from the north (Figure 39).
grav_resid.jpg	Residual gravity anomalies, contoured at 5 mGal intervals (Figure 40)
loadanom.jpg	Load anomaly at 125 km, contoured at 5 MPa intervals (Figure 38)
moho.jpg	Optimised depth to Moho, contoured at 2 km intervals (Figure 32)
obsmag_up1.jpg	Observed magnetic field, upward continued by 1 km (for comparison with calculated fields; Figure 41a)
paldenshift.jpg	Density shift applied to the pre-volcanic Cenozoic sedimentary layer (Figure 14a)
palthk.jpg	Thickness of the pre-volcanic Cenozoic sedimentary layer, contoured at 0.5 km intervals (Figure 26)
postbasthk.jpg	Thickness of the post-volcanic sedimentary rocks, contoured at 0.5 km intervals (Figure 23)
precen_annot.jpg	Optimised pre-Cenozoic sediment thickness with feature labels (Figure 47). Version with smaller labels.
precen_annot_large.jpg	Optimised pre-Cenozoic sediment thickness with feature labels (Figure 47).
precen_init.jpg	Initial pre-Cenozoic sediment thickness, contoured at 1 km intervals (Figure 27)
precen_opt.jpg	Optimised pre-Cenozoic sediment thickness, contoured at 1 km intervals (Figure 34)
pretdenshift.jpg	Density shift applied to the pre-Cenozoic sedimentary layer (Figure 14b)
topbasbal.jpg	Top volcanic sequence / Balder Formation, contoured at 0.5 km intervals (Figure 24)

topbsmnt_annot.jpg	Optimised top basement with feature labels (Figure 48). Version with smaller labels.
topbsmnt_annot_large.jpg	Optimised top basement with feature labels (Figure 48).
topbsmnt_init.jpg	Initial top basement surface, contoured at 1 km intervals (Figure 28)
topbsmnt_opt.jpg	Optimised top basement surface, contoured at 1 km intervals (Figure 35)

OTHER LAYERS

The following shapefiles are included:

tecmap.jpg	Structural elements map of the Faroe-Shetland area, after Ritchie et al. (2011). Figure 1 in this report.
fsc_phys_prop_wells.shp	Locations of wells for which digital geophysical logs were available. Includes hyperlinks to pdf files of log plots. Well locations and other attributes based on a shapefile available for download on the DECC website (https://www.og.decc.gov.uk/information/maps_offshore.htm). Additional attributes are: 'logimages' (location of file containing the log displays) and WATDEP_M (water depth in metres).
fsc_faroese_wells.shp	Locations of wells in the Faroese area, including hyperlinks to pdf files of log displays.
fsc_model_annot.shp	Point shapefile of the annotations shown in Figures 47 and 48 of this report. The accompanying layer file displays the labels in a white box as shown in the figures.
fsc_3dmodel_area.shp	Rectangle enclosing the modelled area
coast_gshhs.shp	Coastline file based on the Global Self-consistent Hierachical, High-resolution Shoreline (GSHHS, Version 1.3) (Wessel and Smith, 1996).

The hyperlinks are activated in ArcGIS by checking the 'Support hyperlinks using field:' checkbox in the Display tab of the Layer Properties and selecting the 'logimages' field. The address assumes that the mxd is located in the folder which contains the '3D_model' subfolder. If this is not the case it will be necessary to edit the links or reorganise the file structure; alternatively the hyperlink base can be set explicitly in Document > Properties.

The Department for Energy and Climate Change (DECC) website referred to above offers a number of useful shapefiles, including UK quads and blocks and the locations of known hydrocarbon fields. These have been copied into the decc_shapefiles subfolder. The document decc_shapefile_info.pdf in this folder contains the information on these layers provided on the website at the time they were downloaded, including the dates on which they were last updated.

Appendix 3 The FSC Viewer

Many of the images contained in this report and in the GIS layers described in Appendix 2 can be accessed using the Faroe-Shetland Consortium 'Viewer', which is a customised interface for comparing geophysical and geological maps and other information in a side-by-side format. Double-click on the **fsc_viewer.htm** file icon in Windows Explorer and the Viewer should appear in the user's default browser. It has been tested in recent versions of Internet Explorer, Mozilla Firefox and Safari on a PC platform, but does not work in Google Chrome. A warning about active content may appear when the Viewer is started up, and it is necessary to allow such content for it to function properly. To avoid getting this message each time the Viewer is used, it is possible to allow active content from CDs or My Computer by default in Internet Explorer by checking the appropriate boxes accessed via Tools > Internet Options > Advanced (scroll down to 'Security').

The default interface (Figure A3.1) has four equally sized windows, although these can be resized by dragging the bars between them, for example moving the horizontal bar upwards to focus on the interactions between the bottom two windows. The display area can be maximised by pressing the F11 button, which is particularly useful with lower resolution monitors. Press the F11 button again to return to the normal display.

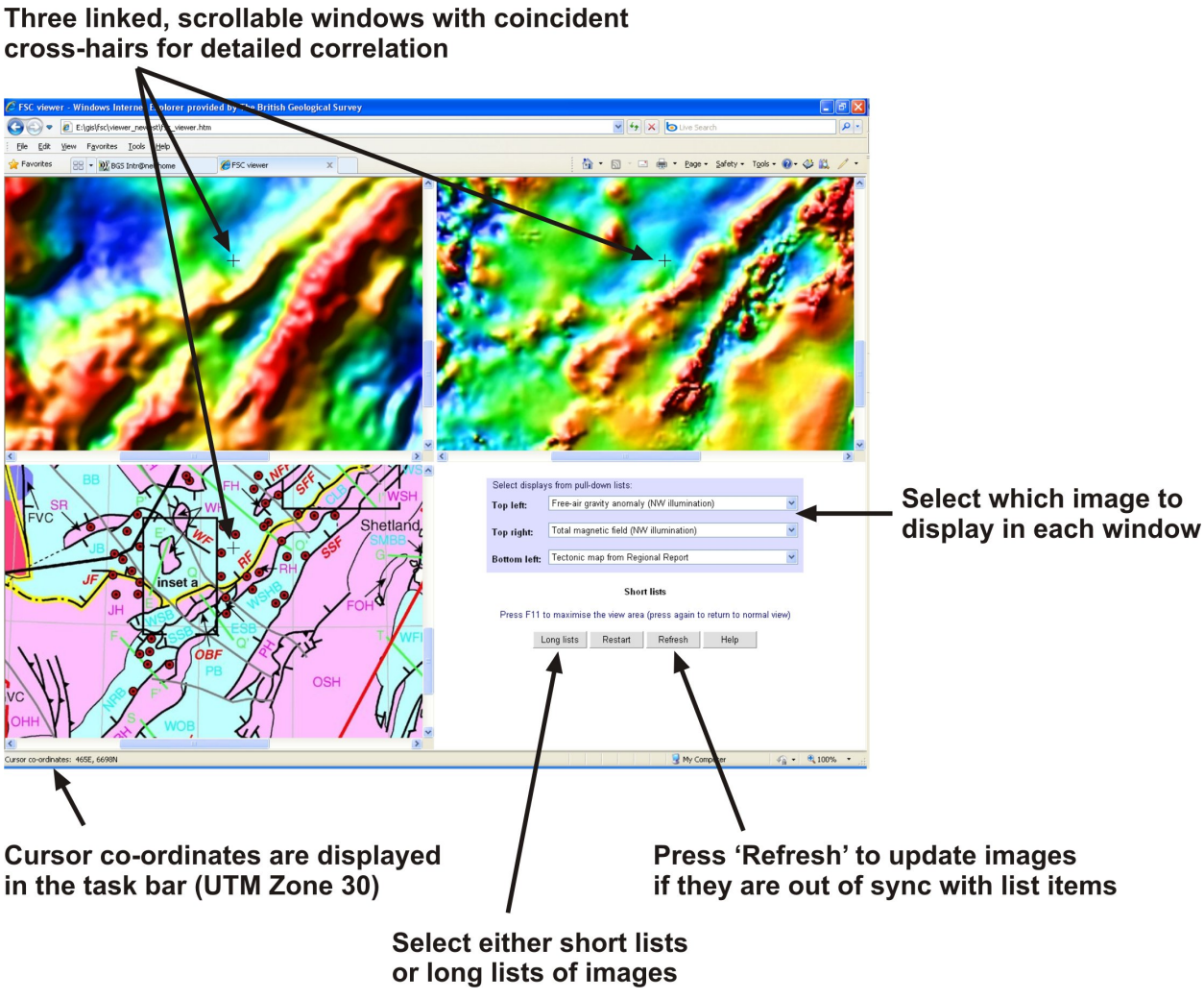

Figure A3.1 The FSC Viewer, with selector panel in the bottom right-hand window

When the Viewer first opens, the bottom right-hand window is occupied by the 'selector' panel, which contains drop-down lists enabling the user to choose what appears in the other three windows. There are two versions of this panel: one which allows access to a short list of selected displays and a second which contains comprehensive lists of images of the geophysical data and model components. Use the left-hand button in the selector window to toggle between these lists. Each retains a memory of the items displayed, so this button can be used to switch rapidly between complementary sets of images. The selector pane also contains buttons to restart the Viewer (for example to equalize the window sizes), to refresh the display (to confirm the synchronisation between displayed images and labels) and for help.

The three image windows are 'locked' together, such that when one is scrolled the other two will follow. When the cursor is moved over one of the windows, coincident cross-hairs appear on all three, enabling detailed correlations to be made between the features they display. The displays that contain abbreviations for structural or geophysical features employ 'tool tips' which spell out the abbreviation if the cursor is held over the label.

The bottom right-hand window is also used to display text and graphics linked to labelled features in selected maps (Figure A3.2). At present the displays that are active in this way are:

- The structural element map from the Faroe-Shetland Basin regional report (Ritchie et al., 2011). Click on labels on this map to access the relevant original text from the report, extracted from Chapter 2 (Structure) (Ritchie et al., 2011) and Chapter 8 (Cenozoic (Igneous)) (Passey and Hitchen, 2011).
- Labelled versions of the optimised Pre-Cenozoic sediment thickness and top basement maps (Figures 47 and 48 in this report), which are linked to the discussion contained in Section 7.4.
- A map of the locations of wells used in the physical property analysis (Section 3) in which the labels are linked to displays of the density and velocity well logs in the format illustrated in Figures 12 and 13. Note that these are in PDF format, so it is required that files in this format can be viewed in the browser window. This is the default when Adobe Acrobat or Reader is installed, but if it doesn't occur check that this option is selected under Edit > Preferences > Internet in one of those programs.

The text invoked from labels on the structural elements and model maps contains links (in red) to the geographical location of the feature under discussion. Clicking on one of these links will pan the three image windows such that the feature lies at their centres, or as near as is possible when it is near the edge of the map. If the windows are different sizes, the bottom left-hand one takes precedence.

The geophysical logs are stored in a single large file, and it is possible to scan through them by clicking on the bottom right-hand window, when it contains this sort of display, and pressing the <Page Up> or <Page Down> keys. Pressing the <Home> key will display the first page of the document, which contains a legend for the geological abbreviations used and the reference curves that appear on each log plot. Holding down the <Ctrl> key while typing 'L' will display the Acrobat toolbars (repeat to remove the toolbars).

To return the bottom right-hand window to the selector panel, double-click on any window (except for the PDF of geophysical well logs). The selector that was in use prior to displaying other information in the window will reappear.

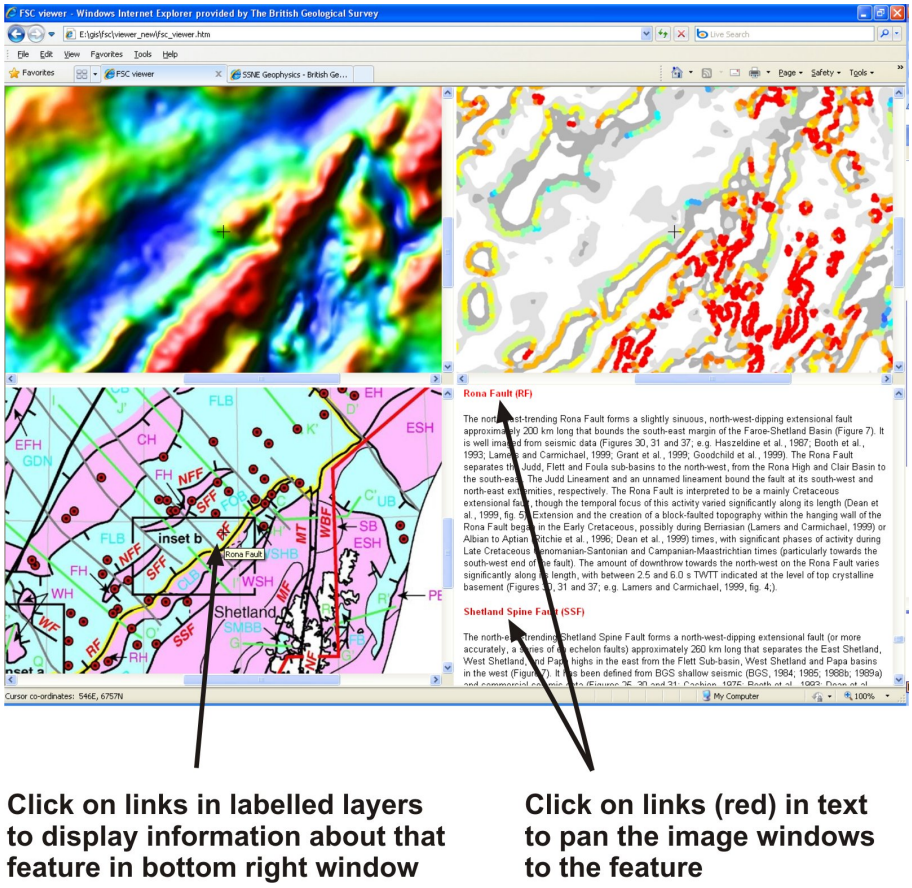

Figure A3.2 The FSC Viewer, with a text panel in the bottom right-hand window

Appendix 4 List of model features

Below is an alphabetical list of the model features shown in Figures 47 and 48 and discussed in Section 7.4, which are also accessible using the the FSC Viewer (Appendix 3).

AB	Auðhumla Basin
ANB	Annika Sub-basin
BB	Brynhild Sub-basin
BE	Beryl Embayment
BVC	Brendan Volcanic Centre
CB	Corona Sub-basin
CF	Circular feature of Robinson et al. (2004)
CH	Corona High
DAVC	Drekaeyga Volcanic Centre
DBB	Dutch Bank Basin
DP	'Dome Prospect' of Archer et al. (2005)
DVC	Darwin Volcanic Centre
EB	Erlend Basin
EFH	East Faroe High
EFIB	East Fair Isle Basin
EH	Erlend High
EOB	East Orkney Basin
ESHB	East Shetland Basin
FBA	Faroe Bank anomaly
FBCB	Faroe Bank Channel Basin
FBCK	Faroe Bank Channel Knoll (volcanic centre)
FEB	Fensal Basin
FLB	Flett(/Foula) sub-basins
FVC	Frænir Volcanic Centre
FYR	Fugloy Ridge
GB	Grimhild Sub-basin
GDN	Guðrun Sub-basin
JB	Judd Sub-basin
JH	Judd High
MAB	Marulk Basin
MAH	Manet High
MB	Møre Basin
MB1	Gravity feature in Møre Basin
MB3	Magnetic high in Møre Basin
MB4	Magnetic features in SE Møre Basin
MFH	Mid Faroe High
MGB	Magnus Basin
MKB	Munkur Basin
MMB	Apparent basin on Møre Marginal High
MR	Munkagrunnur Ridge (gravity anomaly)
MS	Margarta's Spur
MTF	Møre-Trøndelag Fault Complex
MY	Mykines anomaly
NCH	Northern extension of Corona High
NEF	North-east Faroes anomaly
NERB	North-east Rockall Basin
NFBCB	North Faroe Bank Channel Basin
NLB	North Lewis Basin
NRB	North Rona Basin
PWB	Apparent basin beneath Pilot Whale Anticline
RB	Rungne Sub-basin
RH	Rona High
RSVC	Regin Smiður Volcanic Centre
SBH	Solan Bank High
SGVC	Sula Sgeir Volcanic Centre
SR	Sjúrður Ridge
STB	Steinvør Sub-basin
TH	Tróndur High
TS	Tampen Spur
TT	Tjalve Terrace
UB	Unst Basin
VAB	Vana Sub-basin
VIB	Vilje Sub-basin
WFIB	West Fair Isle Basin
WH	Westray High
WLB	West Lewis Basin
WLH	West Lewis High
WOB	West Orkney Basin
WSHB	West Shetland Basin
WTR	Wyville Thomson Ridge

References

British Geological Survey holds most of the references listed below, and copies may be obtained via the library service subject to copyright legislation (contact libuser@bgs.ac.uk for details). The library catalogue is available at: http://geolib.bgs.ac.uk.

ANDERSEN, M S, SØRENSEN, A B, BOLDREEL, L O, and NIELSEN, T. 2002. Cenozoic evolution of the Faroe Platform: comparing denudation and deposition. 291-311 in *Exhunation of the North Atlantic Margin: Timing Mechanisms and Implications for Petroleum Exploration*. Doré, A G, Cartwright, J A, Stoker , M S, Turner, J P, and White, N (editors). *Geological Society, London, Special Publications*, No. 196.

ARCHER, S G, BERGMAN, S C, ILIFFE, J, MURPHY, C M, and THORNTON, M. 2005. Palaeogene igneous rocks reveal new insights into the geodynamic evolution and petroleum potential of the NE Rockall Trough. *Basin Research*, Vol. 17, 171-201.

BALLING, N, KRISTIANSEN, J I, and SAXOV, S. 1984. Geothermal measurements from the Vestmanna-1 and Lopra-1 Boreholes. 137-147 in *The deep drilling project 1980-1981 in the Faroe Islands*. BERTHELSEN, O, NOE-NYGAARD, A, and RASMUSSEN, J (editors). *Annales Societatis Scientiarum Faeroensis*, Supplementum IX.

BALLING, N, BREINER, N, and WAAGSTEIN, R. 2006. Thermal structure of the deep Lopra-1/1A borehole in the Faroe Islands. 91-108 in *Scientific results from the deepened Lopra-1 borehole, Faroe Islands*. CHALMERS, J A, and WAAGSTEIN, R (Editors). *Bulletin of the Geological Survey of Denmark and Greenland*, No. 9.

BELL, B R, and BUTCHER, H. 2002. On the emplacement of sill complexes: evidence from the Faroe–Shetland Basin. 307–329 *in* The North Atlantic Igneous Province: stratigraphy, tectonic, volcanic and magmatic processes. JOLLEY, D W, and BELL, B R (editors). *Geological Society of London Special Publication*, No. 197.

BLYSTAD, P, BREKKE, H, FAERSETH, R B, LARSEN, B T, SKOGSEID, J, and TØRRUDBAKKEN, B. 1995. *Structural elements of the Norwegian continental shelf. Part II: The Norwegian Sea Region*. NPD-Bulletin, No. 8. (Stavanger: Norwegian Petroleum Directorate.)

BOLDREEL, L O. 2006. Wire-line log-based stratigraphy of flood basalts from the Lopra 1/1A well, Faroe Islands. 7-22 in *Scientific results from the deepened Lopra-1 borehole, Faroe Islands*. CHALMERS, J A, and WAAGSTEIN, R (editors). *Bulletin of the Geological Survey of Denmark and Greenland*, No. 9.

BRITISH GEOLOGICAL SURVEY. 2007. North Rockall Basin (Sheet 58ºN 13ºW, bedrock). 1:500000. (Keyworth, Nottingham: British Geological Survey.)

BRITISH GEOLOGICAL SURVEY and JARÐFEINGI. In preparation. NE Faroe-Shetland Basin (Sheet 62ºN 4ºW, bedrock). 1:500000. (Keyworth, Nottingham: British Geological Survey.)

CARLSON, R L, and HERRICK, C N. 1990. Densities and porosities in the oceanic crust and their variations with depth and age. *Journal of Geophysical Research*, Vol. 95, 9153-9170.

CARR, A D, and SCOTCHMAN, I C. 2003. Thermal history modelling in the southern Faroe-Shetland Basin. *Petroleum Geoscience*, Vol. 9, 333-345.

CHAPMAN, M E, AND BODINE, J. 1979. Considerations of the indirect effect in marine gravity modelling. *Journal of Geophysical Research*, Vol. 84, 3889-3892.

CHRISTIE, P, GOLLIFER, I, and COWPER, D. 2006. Borehole seismic studies of a volcanic succession from the Lopra-1/1A borehole in the Faroe Islands, northern North Atlantic. 23-40 in *Scientific results from the deepened Lopra-1 borehole, Faroe Islands*. CHALMERS, J A, and WAAGSTEIN, R (editors). *Geological Survey of Denmark and Greenland Bulletin*, Vol. 9, .

CORCORAN, D V, and MECKLENBURGH R. 2005. Exhumation of the Corrib gasfield, Slyne Basin, offshore Ireland. *Petroleum Geoscience*, Vol. 11, 239–256.

DABEK, Z K and WILLIAMSON, J P. 1999. Forward and inverse wavenumber formulae for the gravity and magnetic responses of layered models. *British Geological Survey Technical Report* WK/99/03C.

EBBING, J, AND OLESEN, O. 2011. New compilation of top basement and basement thickness for the Norwegian Continental Shelf reveals the segmentation of the passive margin system. *Petroleum Geology: from Mature Basins to New Frontiers - Proceedings of the 7th Petroleum Geology Conference.*(London: The Geological Society.)

ECCLES, J D, WHITE, R S, and CHRISTIE, P A F. 2009. Identification and inversion of converted shear waves: case studies from the European North Atlantic continental margins. *Geophysical Journal International*, Vol. 179, 381-400.

ELLIS, D, BELL, B R, JOLLEY, D W, and O'CALLAGHAN, M. 2002. The stratigraphy, environment of eruption and age of the Faroes Lava Group, NE Atlantic Ocean. 253–269 *in* The North Atlantic Igneous Province: Stratigraphy, Tectonic, Volcanic and Magmatic Processes. JOLLEY, D W, and BELL, B R (editors). *Geological Society of London Special Publication*, No. 197.

EVANS, D, GRAHAM, C C, ARMOUR, A, AND BATHURST, P. 2003. The Millennium Atlas: petroleum geology of the Central and Northern North Sea. (London: The Geological Society.)

GIBB, F G F, and KANARIS-SOTIRIOU, R. 1988. The geochemistry and origin of the Faroe–Shetland sill complex. 241–252 *in* Early Tertiary volcanism and the opening of the NE Atlantic. MORTON, A C, and PARSON, L M (editors). *Geological Society of London Special Publication*, No. 39.

HALD, N and WAAGSTEIN, R. 1984. Lithology and chemistry of a 2-km sequence of Lower Tertiary tholeiitic lavas drilled on Suðuroy, Faeroe Islands. 15-38 in *The deep drilling project 1980-1981 in the Faeroe Islands*. BERTHELSON, O, NOE-NYGAARD, A, and RASMUSSEN, J (editors). *Annales Societatis Scientiarum Faeroensis*, Supplementum IX.

HITCHEN, K, and RITCHIE, J D. 1987. Geological review of the West Shetland area. 737–749 in *Petroleum geology of northwest Europe, proceedings of the 3rd conference*. BROOKS, J, and GLENNIE, K W (editors). (London: Graham and Trotman.)

HOLLOWAY, S, REAY, D M, DONATO, J, and BEDDOE-STEPHENS, B. 1991. Distribution of granite and possible Devonian sediments in part of the East Shetland Platform, North Sea. *Journal of the Geological Society, London*, Vol. 148, 635-638.

HOLMES, A J, GRIFFITH, C E, and SCOTCHMAN, I C. 1999. The Jurassic petroleum system West of Britain Atlantic margin - an integration of tectonics, geochemistry and basin modelling. 1351–1365 in *Petroleum geology of northwest Europe, proceedings of the 5th conference.* FLEET, A J, and BOLDY, S A R (editors). (London: The Geological Society.)

HOSPERS, J, and EDIRIWEERA, K K. 1991. Depth and configuration of the crystalline basement in the Viking Graben area, Northern North Sea. *Journal of the Geological Society, London*, Vol. 148, 261-265.

IOC, IHO, and BODC. 2003. *Centenary Edition of the GEBCO Digital Atlas*. Published on CD-ROM on behalf of the Intergovernmental Oceanographic Commission and the International Hydrographic Organization as part of the General Bathymetric Chart of the Oceans. [Liverpool: British Oceanographic Data Centre]. See also http://www.gebco.net/.

JAPSEN, P. 2000. Investigation of multi-phase erosion using reconstructed shale trends based on sonic data. Sole Pit axis, North Sea. *Global and Planetary Change*, Vol. 24, 189–210.

JAPSEN, P, ANDERSEN, C, ANDERSEN, H L, ANDERSEN, M S, BOLDREEL, L O, MAVKO, G, MOHAMMED, N G, PEDERSEN, J M, PETERSEN, U K, RASMUSSEN, R, SHAW, F, SPRINGER, N, WAAGSTEIN, R, WHITE, R S, and WORTHINGTON, M. 2005. Preliminary results from investigations of seismic and petrophysical properties of Faroes basalts in the SeiFaBa project. 1462-1470 in *Petroleum Geology: North-West Europe and Global Perspectives - Proceedings of the 6th Petroleum Geology Conference*. DORÉ, A G and VINING, B (editors). (London: The Geological Society.)

JAPSEN, P, MUKERJI, T, and MAVKO, G. 2007. Constraints on velocity-depth trends from rock physics models. *Geophysical Prospecting*, Vol. 55, 135-154.

JOHNS, C R, and ANDREWS, I J. 1985. The petroleum geology of the Unst Basin. *Marine and Petroleum Geology*, Vol. 2, 361–372.

JØRGENSEN, O. 2006. The regional distribution of zeolites in the basalts of the Faroe Islands and the significance of zeolites as palaeo-temperature indicators. 123-156 in *Scientific results from the deepened Lopra-1 borehole, Faroe Islands*. CHALMERS, J A, and WAAGSTEIN, R (editors). *Bulletin of the Geological Survey of Denmark and Greenland*, No. 9.

KESER NEISH, J. 2003. *The Faroese region: a standard structural nomenclature system*. (Tórshavn, Faroe Islands: Faroese Geological Survey.)

KESER NEISH, J. 2005. Faroese area: structural interpretation of seismic data in a basalt environment. 131–145 *in* Faroe Islands Exploration Conference: Proceedings of the 1st Conference ZISKA, H, VARMING, T, and BLOCH, D (editors). *Annales Societatis Scientarum Færoensis Supplementum,* Vol. 43.

KESER NEISH, J, and ZISKA, H. 2005. Structure of the Faroe Bank Channel Basin, offshore Faroe Islands. 873-885 in *Petroleum Geology: North-West Europe and Global Perspectives - Proceedings of the 6th Petroleum Geology Conference*. DORÉ, A G and VINING, B (editors). (London: The Geological Society.)

KIMBELL, G S, GATLIFF, R W, RITCHIE, J D, WALKER, A S D, and WILLIAMSON, J P. 2004. Regional three-dimensional modelling of the NE Atlantic margin. *Basin Research*, Vol. 16, 259-278.

KIMBELL, G S, RITCHIE, J D, JOHNSON, H, and GATLIFF, R W. 2005. Controls on the structure and evolution of the NE Atlantic margin revealed by regional potential field imaging and 3D modelling. 933-945 in *Petroleum Geology: North-West Europe and Global Perspectives - Proceedings of the 6th Petroleum Geology Conference*. DORÉ, A G and VINING, B (editors). (London: The Geological Society.)

KIMBELL, G S, RITCHIE, J D, and HENDERSON, A F. 2010. Three-dimensional gravity and magnetic modelling of the Irish sector of the NE Atlantic margin. *Tectonophysics*, Vol. 486, 36-54.

KLEIN, E M, and LANGMUIR, C H. 1987. Global corrections of ocean ridge basalt chemistry with axial depth and crustal thickness. *Journal of Geophysical Research*, Vol. 92, 8089-8115.

KLEMPERER, S L, and HOBBS, R W. 1991. *The BIRPS Atlas. Deep seismic reflection profiles around the British Isles*. (Cambridge: Cambridge University Press.)

KLINGELHÖFER, F, EDWARDS, R A, HOBBS, R W, and ENGLAND, R W. 2005. Crustal structure of the NE Rockall Trough from wide-angle seismic data modelling. *Journal of Geophysical Research*, Vol. 110, B11105.

KORENAGA, J, HOLBROOK, W S, DETRICK, R S, and KELEMAN, P B. 2001. Gravity anomalies and crustal structure at the southeast Greenland margin. *Journal of Geophysical Research*, Vol. 106, 8853-8870.

LAU , K W H, WHITE, R S, and CHRISTIE, P A F. 2009. Constraining basalt thickness and sub-basalt velocities by combined analysis of ocean-bottom seismic and streamer data. *Presentation ot the 3rd Faroe Islands Exploration Conference, Tórshavn, Faroe Islands, 15-16 September 2009*.

LUNDIN, E R, and DORÉ, A G. 2002. A tectonic model for the Norwegian passive margin with implications for the NE Atlantic: Early Cretaceous to break-up. *Journal of the Geological Society, London*, Vol. 154, 545-550.

MOY, D J, and IMBER, J. 2009. A critical analysis of the structure and tectonic significance of rift-oblique lineaments ('transfer zones') in the Mesozoic-Cenozoic succession of the Faroe-Shetland Basin, NE Atlantic margin. *Journal of the Geological Society, London*, Vol. 166, 831-844.

NIU, Y, and BATIZA, R. 1991. Insitu densities of MORB melts and residual mantle: implications for buouyancy forces beneath mid-ocean ridges. *Journal of Geology*, Vol. 99, 767-775.

NØTTVEDT, A, BERGE, A M, DAWERS, N H, FÆRSETH, R B, HÄGER, K O, MANGERUD, G, and PUIGDEFABREGAS, C. 2000. Syn-rift evolution and resulting plays models in the Snorre-H area, northern North Sea. 179-218 *in* Dynamics of the Norwegian Margin. NØTTVEDT, A (editor). *Geological Society of London Special Publication*, Vol. 167.

OLAFSSON, I, SUNDVOR, E, ELDHOLM, O, and GRUE, K. 1992. Møre Margin: Crustal structure from analysis of expanded spread profiles. *Marine Geophysical Researches*, Vol. 14, 137-162.

OLDENBURG, D W. 1974. The inversion and interpretation of gravity anomalies. *Geophysics*, Vol. 39, 526-536.

PARKER, R L. 1972. The rapid calculation of potential anomalies. *Geophysical Journal of the Royal Astronomical Society*, Vol. 31, 447-455.

PARKIN, C J, and WHITE, R S. 2008. Influence of the Iceland mantle plume on oceanic crust generation in the North Atlantic. *Geophysical Journal International*, Vol. 173, 168-188.

PARKIN, C J, LUNNON, Z C, WHITE, R S, CHRISTIE, P A F, and ISIMM TEAM. 2007. Imaging the pulsing Iceland mantle plume through the Eocene. *Geology*, Vol. 35, 93-96.

PASSEY, S, and HITCHEN, K. 2011. Cenozoic (igneous). 209-228 in *United Kingdom Offshore Regional Report: The geology of the Faroe-Shetland Basin and adjacent areas*. RITCHIE , J D, ZISKA, H, JOHNSON, H, and EVANS, D (editors). (Keyworth, Nottingham: British Geological Survey.)

PLANKE, S, ALVESTAD, E, and ELDHOLM, O. 1999. Seismic characteristics of basaltic extrusive and intrusive rocks. *The Leading Edg*e, Vol. 19, 342–348.

REYNISSON, R F, EBBING, J, and SKILBREI, J R. 2009. The use of potential field data in revealing the basement structure in sub-basaltic settings. An example from the Møre margin, offshore Norway. *Geophysical Prospecting*, Vol. 57, 753-771.

RIISAGER, P, RIISAGER, J, ABRAHAMSEN, N, and WAAGSTEIN, R. 2002. New palaeomagnetic pole and magnetostratigraphy of Faroe Islands flood volcanic, North Atlantic igneous province. *Earth and Planetary Science Letters*, Vol. 201, 261-276.

RIISHUUS, M S, PEATE, D W, TEGNER, C, WILSON, J R, and BROOKS, C K. 2008. Petrogenesis of cogenetic silica-oversaturated and -undersaturated syenites by periodic recharge in a crustally contaminated magma chamber: the Kangerlussuaq Intrusion, East Greenland. *Journal of Petrology*, Vol. 49, 493-522.

RITCHIE, J D, JOHNSON, H, and KIMBELL, G S. 2003. The nature and age of Cenozoic contractional deformation within the NE Faroe-Shetland Basin. *Marine and Petroleum Geology*, Vol. 20, 399-409.

RITCHIE, J D, ZISKA, H, KIMBELL, G S, QUINN, M, and CHADWICK, R A. 2011. Structure. 9-70 in *United Kingdom Offshore Regional Report: The geology of the Faroe-Shetland Basin and adjacent areas*. RITCHIE, J D, ZISKA, H, JOHNSON, H, and EVANS, D (editors). (Keyworth, Nottingham: British Geological Survey.)

ROBERTS, A W, WHITE, R S, LUNNON, Z C, CHRISTIE, P A F, SPITZER, R, and ISIMM TEAM. 2005. Imaging magmatic rocks on the Faroes margin. 755-766 in *Petroleum Geology: North-West Europe and Global Perspectives - Proceedings of the 6th Petroleum Geology Conference*. DORÉ, A G and VINING, B (editors). (London: The Geological Society.)

ROBERTS, A M, CORFIELD, R I, KUSZNIR, N J, MATTHEWS, S J, HANSEN, E-K, and HOPPER, J. 2009a. Mapping palaeostructure and palaeobathymetry along the Norwegian Atlantic continental margin: Møre and Vøring basins. *Petroleum Geoscience*, Vol. 15, 27-43.

ROBERTS, A W, WHITE, R S, and CHRISTIE, P A F. 2009b. Imaging igneous rocks on the North Atlantic rifted continental margin. *Geophysical Journal International*, Vol. 179, 1024-1038.

ROBINSON, A M, CARTWRIGHT, J, BURGESS, P M, and DAVIES, R J. 2004. Interactions between topography and channel development from 3D seismic analysis: an example from the Tertiary of the Flett Ridge, Faroe–Shetland Basin, UK. 73–82 *in* 3D seismic technology: application to the exploration of sedimentary basins. DAVIES, R J, CARTWRIGHT, J A, STEWART, S A, LAPPIN, M, and UNDERHILL, J R (editors). *Geological Society of London Memoir*, No. 29.

ROHRMAN, M. 2007. Prospectivity of volcanic basins: Trap delineation and acreage de-risking. *Bulletin of the American Association of Petroleum Geologists*, Vol. 91, 915-939.

RUMPH, B, REAVES, C M, ORANGE, V G, and ROBINSON, D L. 1993. Structuring and transfer zones in the Faeroe Basin in a regional context. 999-1009 in *Petroleum Geology of Northwest Europe: Proceedings of the 4th Conference*. PARKER, J R (editor). (London: the Geological Society.)

SALEM, A, WILLIAMS, S, FAIRHEAD, J D, RAVAT, D, and SMITH, R. 2007. Tilt-depth method: A simple depth estimation method using first-order magnetic derivatives. *The Leading Edge*, Vol. 26, 1502-1505.

SANDWELL, D T, and SMITH, W H F. 2009. Global marine gravity from retracked Geosat and ERS-1 altimetry: ridge segmentation versus spreading rate. *Journal of Geophysical Research*, Vol. 114, B01411, doi:10.1029/2008JB006008.

SCHLUMBERGER. 1989. *Log Interpretation Principles/Applications*. (Houston: Schlumberger Educational Services.)

SCHRØDER, N F. 1971. Magnetic anomalies around the Faroe Islands. *Fróðskaparrit*, Vol. 19, 20-29.

SCLATER, J G, and CHRISTIE, P A F. 1980. Continental stretching: an explanation of the post-mid-Cretaceous subsidence of the central North Sea basin. *Journal of Geophysical Research*, Vol. 85, 3711–3739.

SMALLWOOD, J R, and MARESH, J. 2002. The properties, morphology and distribution of igneous sills: modelling, borehole data and 3D seismic from the Faroe-Shetland area. 271-306 in *The North Atlantic Igneous Province: Stratigraphy, Tectonic, Volcanic and Magmatic Processes*. JOLLEY, D W, and BELL, B R (editors). *Geological Society, London, Special Publications*, No. 197.

SMALLWOOD, J R, TOWNS, M J, and WHITE, R S. 2001. The structure of the Faroe-Shetland Trough from integrated deep seismic and potential field modelling. *Journal of the Geological Society, London*, Vol. 158, 409-412.

SMALLWOOD, J R, PRESCOTT, D, and KIRK, W. 2004. Alternatives to Paleocene exploratioin West of Shetland: a case study. *Scottish Journal of Geology*, Vol. 40, 131-143.

SMITH, K, WHITLEY, P W, KIMBELL, G S, JOHNSON, H, and KUBALA, M. 2009. Enhancing the prospectivity of the Wyville Thomson Ridge. 286–302 *in Faroe Islands Exploration Exploration Conference: Proceedings of the 2nd Conference*. VARMING, T, and ZISKA, H (editors). *Annales Societatis Scientiarum Færoensis,* Vol. 50.

SNYDER, D, and HOBBS, R. 1999. *The BIRPS Atlas II. A Second Decade of Deep Seismic Reflection Profiling.* (London: The Geological Society.) On CD-ROM.

SRIVASTAVA, S P, VOPPEL, D, and TUCHOLKE, B. 1988. *Geophysical Atlas of the North Atlantic 50º to 72ºN and 0º to 65º W*. (Hamburg: Deutsches Hydrographisches Institut.)

STOKER, M S, and VARMING, T. 2011. Cenozoic (Sedimentary). 151-208 in *United Kingdom Offshore Regional Report: The geology of the Faroe-Shetland Basin and adjacent areas*. RITCHIE , J D, ZISKA, H, JOHNSON, H, and EVANS, D (editors). (Keyworth, Nottingham: British Geological Survey.)

STOKER, M S, PRAEG, D, HJELSTUEN, B O, LABERG, J S, NIELSON, T and SHANNON, P M. 2005. Neogene stratigraphy and the sedimentary and oceanographic development of the NW European Atlantic margin. *Marine and Petroleum Geology*, Vol. 22, 977-1005.

SWEETMAN, S. 1997. The integration of seismic interpretations with gravity and magnetic 2-D modelling — An example from offshore Faroes area. *The Leading Edge*, 15–20.

TEGNER, C, BROOKS, C K, DUNCAN, R A, HEISTER, L E, and BERNSTEIN, S. 2008. ^{40}Ar-^{39}Ar ages of intrusions in East Greenland: Rift-to-drift transition over the Iceland hotspot. *Lithos*, Vol. 101, 480-500.

THOMSON, K. 2007. Determining magma flow in sills, dykes and laccoliths and their implications for sill emplacement mechanisms. *Bulletin of Volcanology*, Vol.70, 183-201.

TRUDE, J, CARTWRIGHT, J, DAVIES, R J, and SMALLWOOD, J. 2003. New technique for dating igneous sills. *Geology*, Vol. 31, 813-816.

VERGARA, L, WREGLESWORTH, I, TRAYFOOT, M, and RICHARDSEN, G. 2001. The distribution of Cretaceous and Paleocene deep-water reservoirs in the Norwegian Sea basins. *Petroleum Geoscience*, Vol. 7, 395-408.

VERHOEF, J, ROEST, W R, MACNAB, R, ARKANI-HAMED, J, ET AL. 1996. Magnetic anomalies of the Arctic and North Atlantic Oceans and adjacent land areas. *Geological Survey of Canada Open File Report*, No. 3125a.

WESSEL, P, and SMITH, W H F. 1996. A Global, Self-consistent, Hierarchical, High-Resolution Shoreline Database. *Journal of Geophysical Research*, Vol. 101, 8741-8743.

WHITE, R S, SMITH, L K, ROBERTS, A W, CHRISTIE, P A F, KUSZNIR, N J, and the iSIMM Team. 2008. Lower crustal intrusion on the North Atlantic continental margin. *Nature*, Vol. 452, 460-464.

ZISKA, H, and MORGAN, R. 2005. Can palaeomagnetism be used as a mapping tool in basalt provinces. *EAGE 67th Conference and Exhibition, Madrid, Spain, 13-16 June 2005. Abstract volume*. Paper G039.

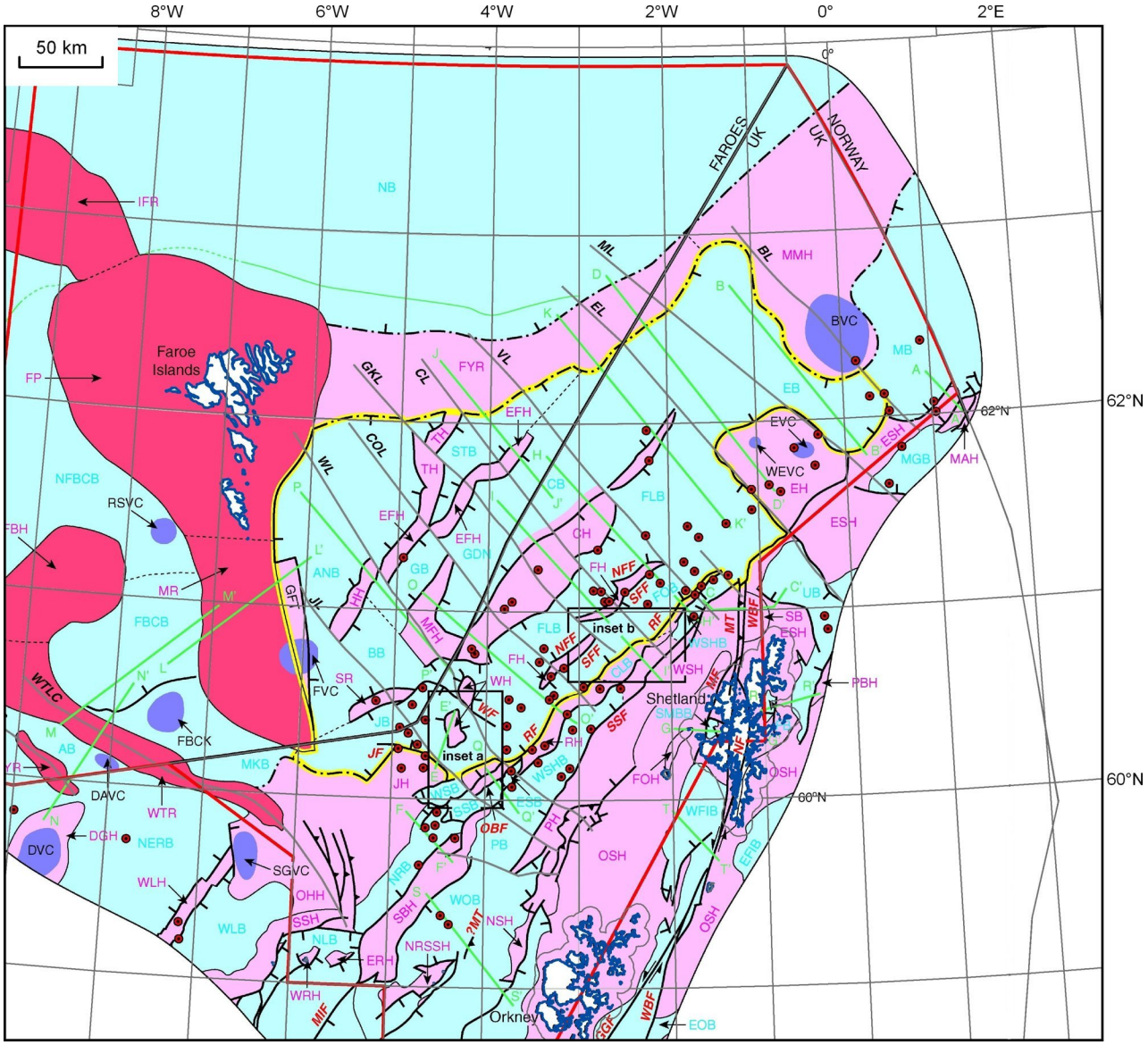

Figure 1 Structural elements map from the Faroe-Shetland Basin regional report (Ritchie,et al., 2011). See Appendix 1 for a key to the abbreviations.

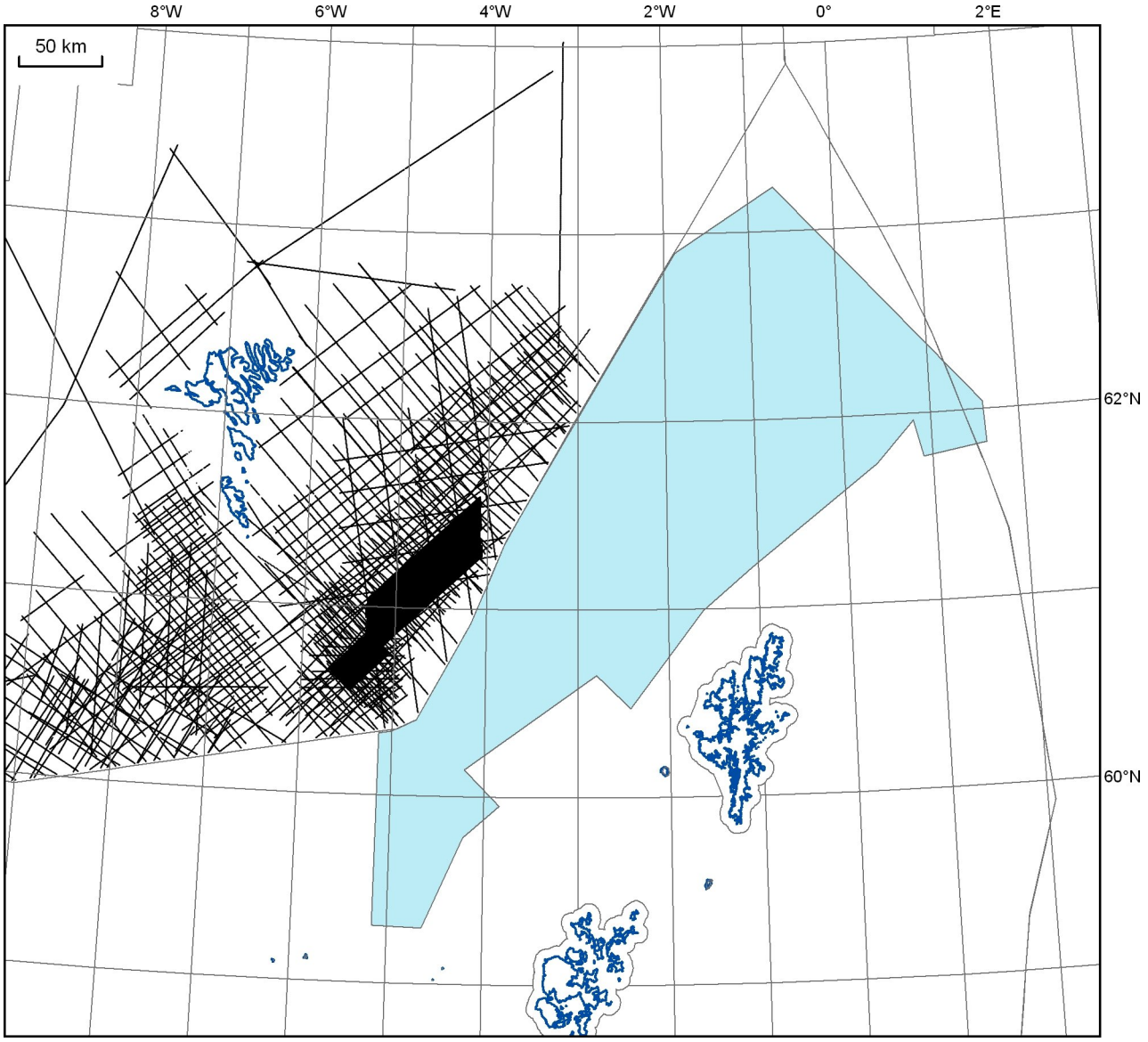

Figure 2 Location of the Faroe-Shetland Consortium seismic database. Blue polygon indicates the approximate area covered by the UK component.

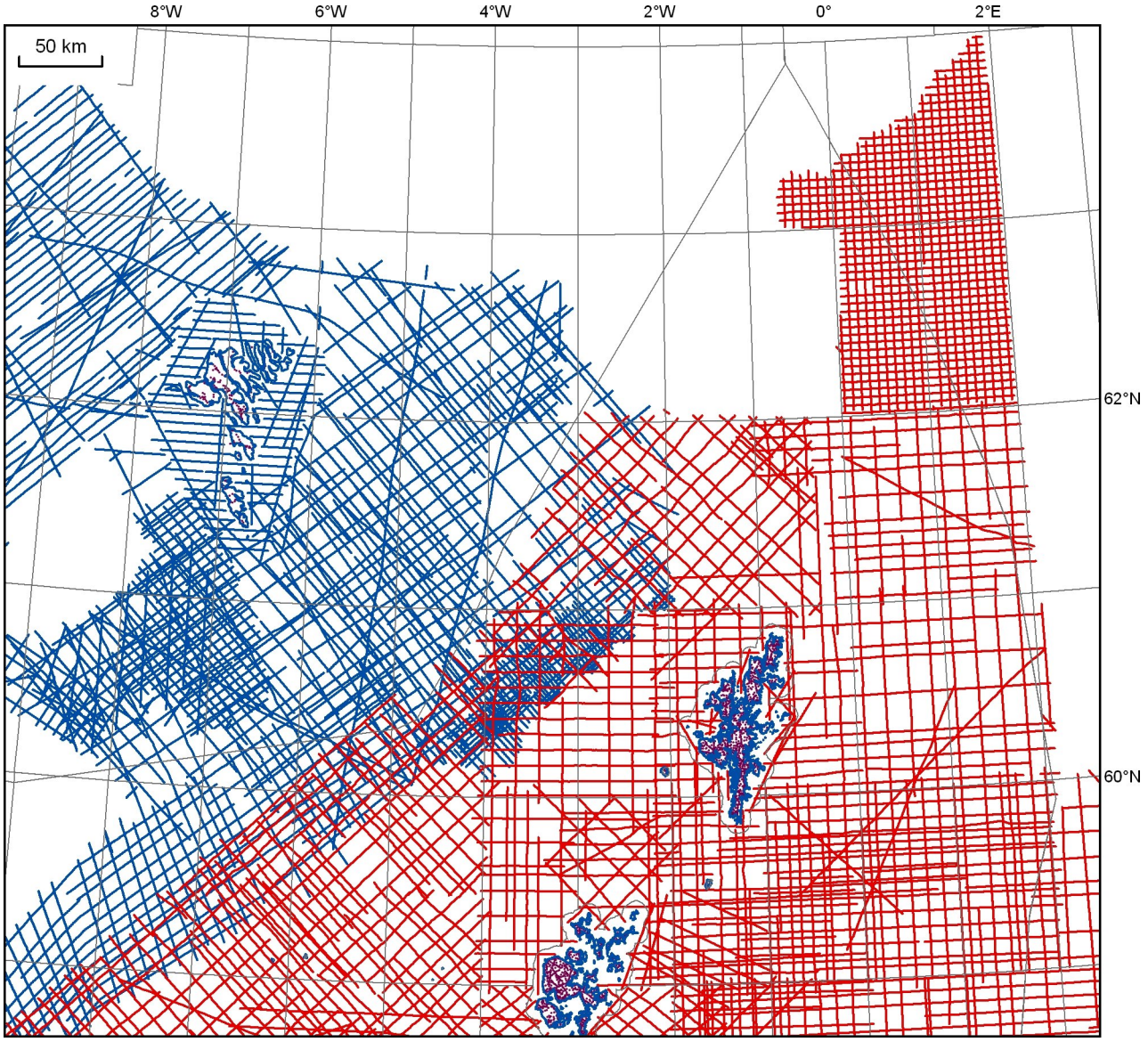

Figure 3 Distribution of gravity data points. Blue = released Faroese marine survey data + extensions of WesternGeco lines into UK waters; red = BGS marine survey data; purple = land stations (BGS on Orkney and Shetland and KMS on Faroe Islands). Blank areas were filled with satellite-derived data (Sandwell and Smith, 2009).

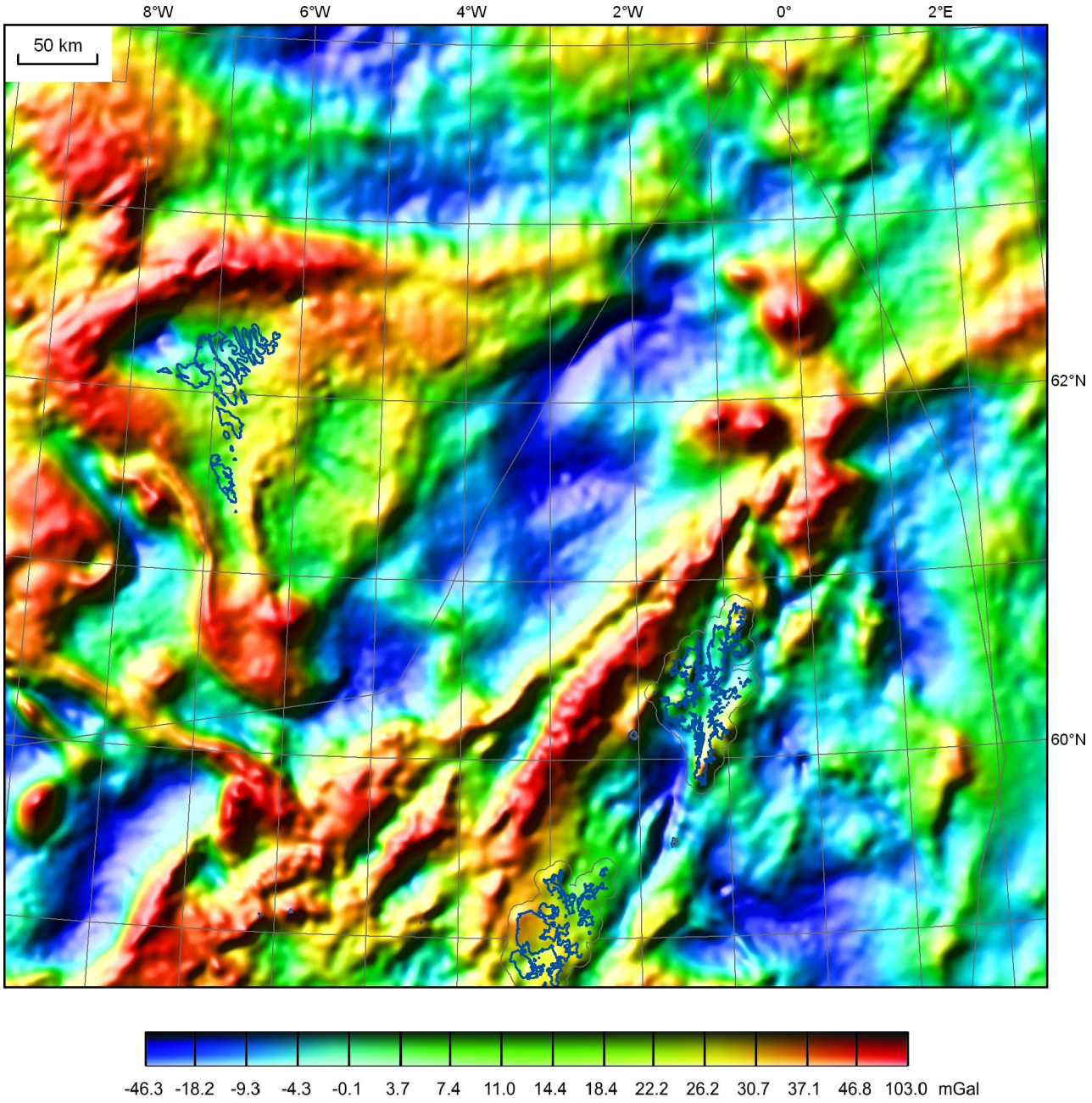

Figure 4 Free-air gravity anomaly (Bouguer anomaly onshore). Colour shaded-relief image with illumination from the north-west.

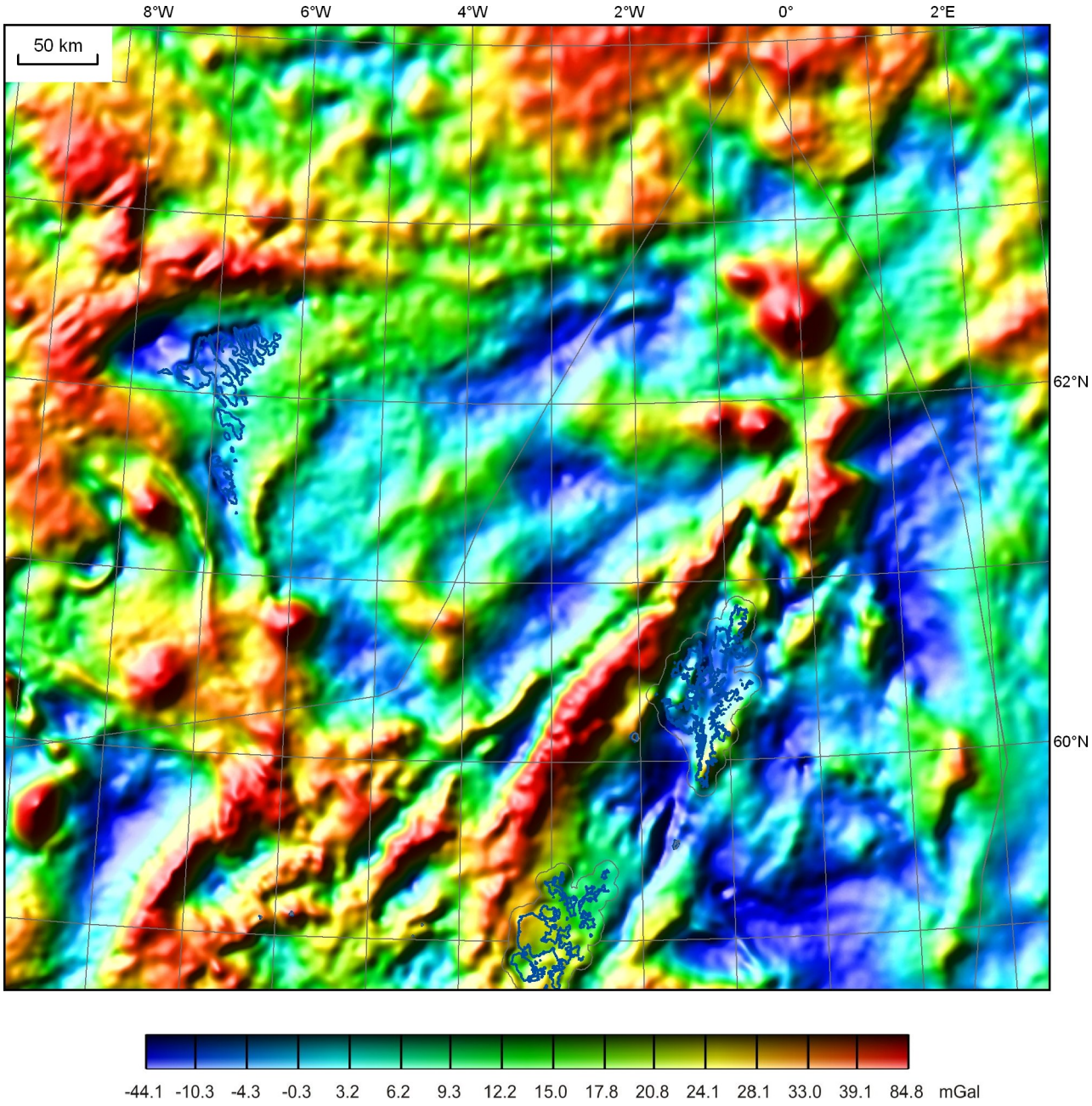

Figure 5 Isostatically corrected Bouguer gravity anomaly. Colour shaded-relief image with illumination from the north-west.

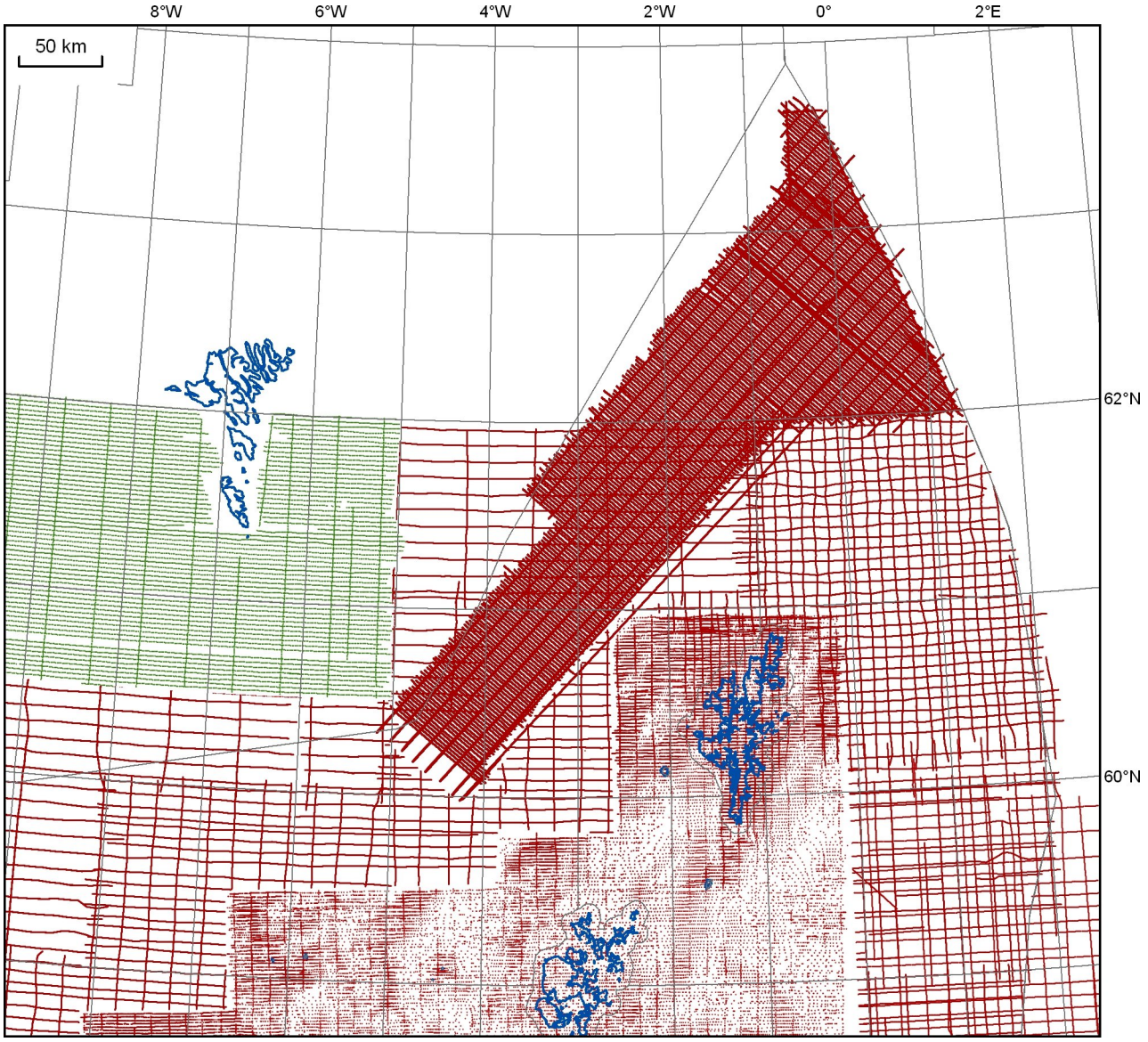

Figure 6 Location of magnetic data points. Brown = BGS airborne and marine data; green = Project Magnet airborne data. Blank areas were filled using data from the GAMMAA5 compilation (Verhoef et al., 1996).

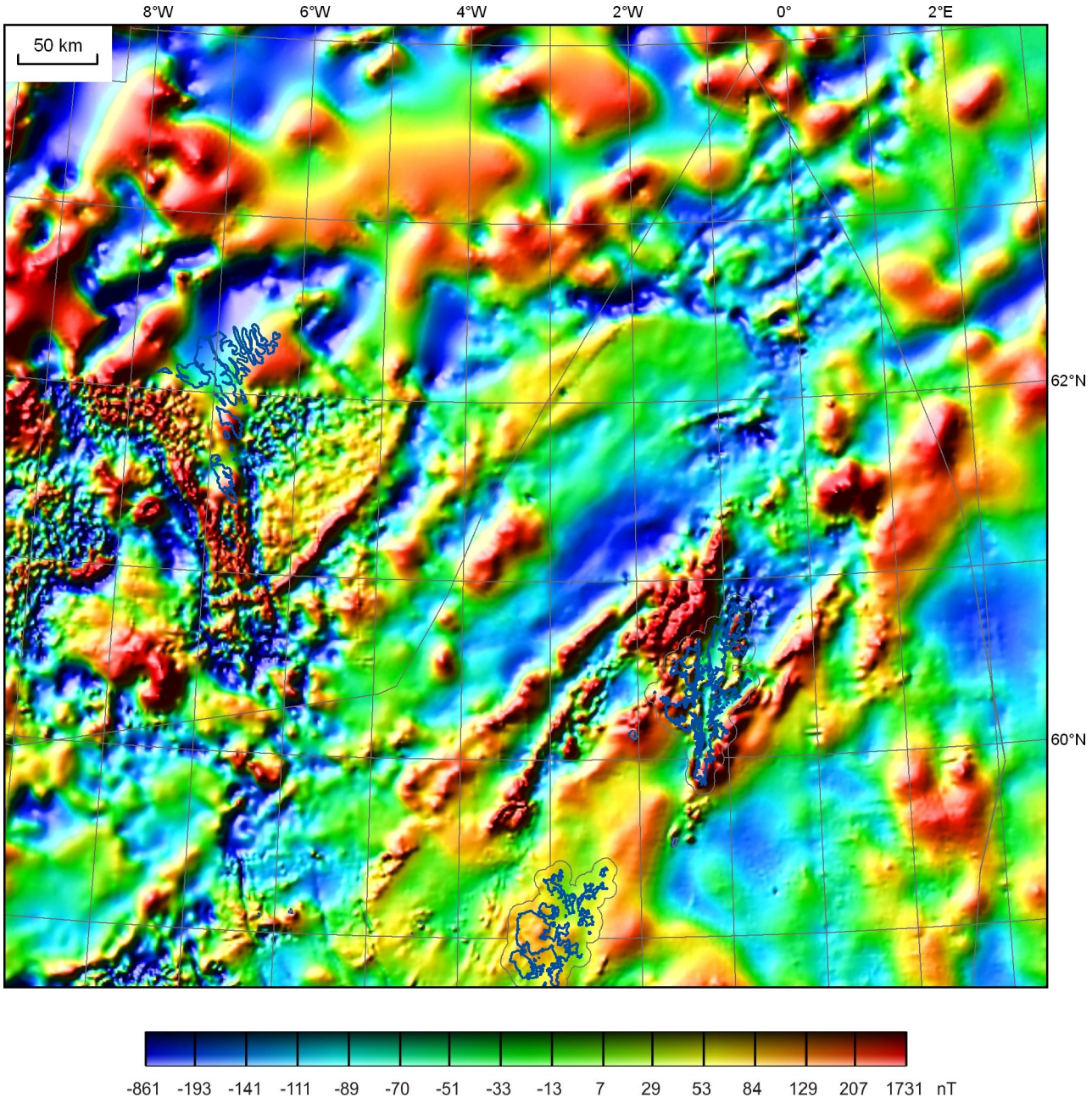

Figure 7 Total magnetic field variations. Colour shaded-relief image with illumination from the north-west.

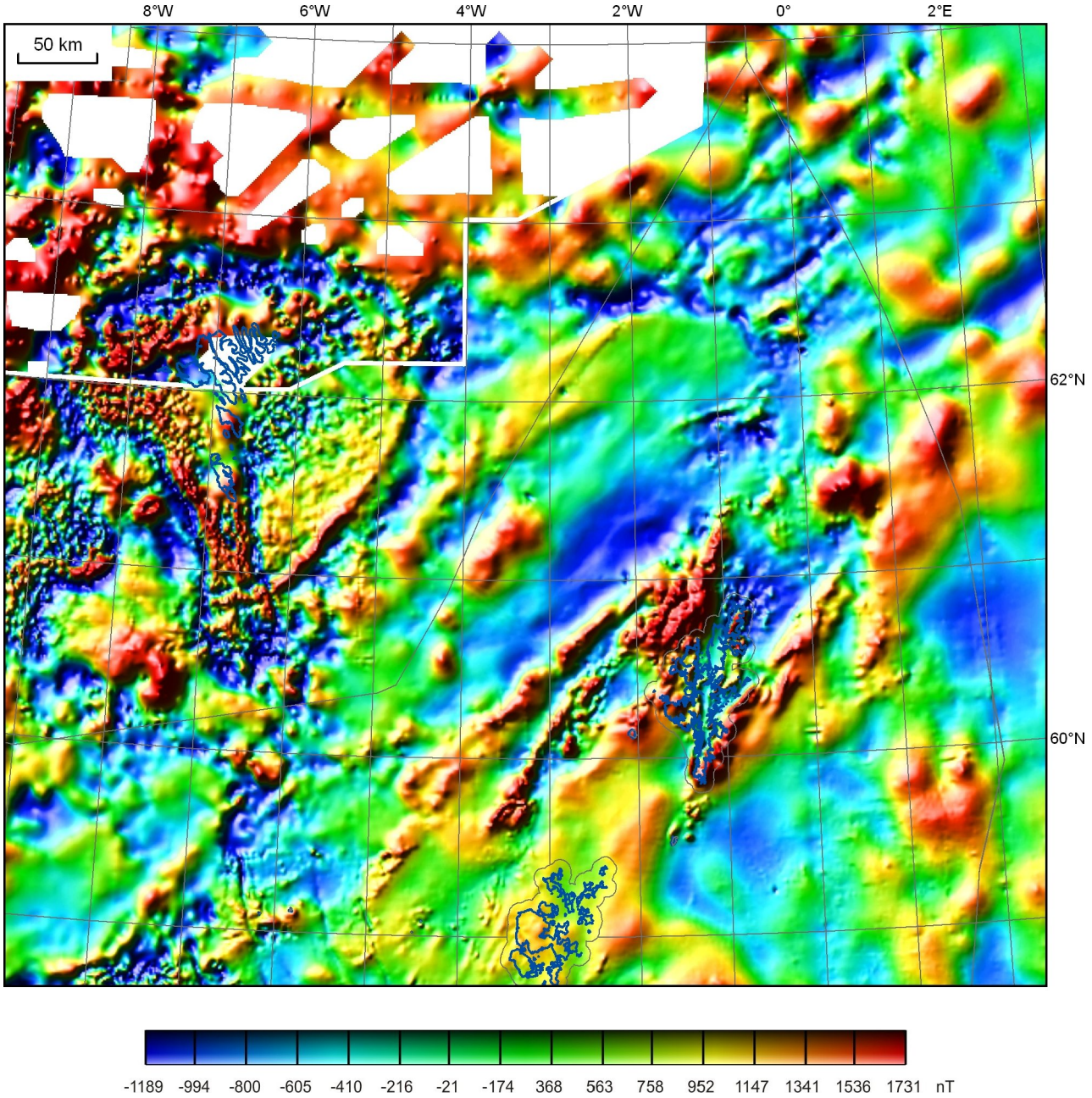

Figure 8 Total magnetic field variations from an alternative magnetic compilation, which substitutes released marine magnetic data to the north of the Faroe Islands. Colour shaded-relief image with illumination from the north-west.

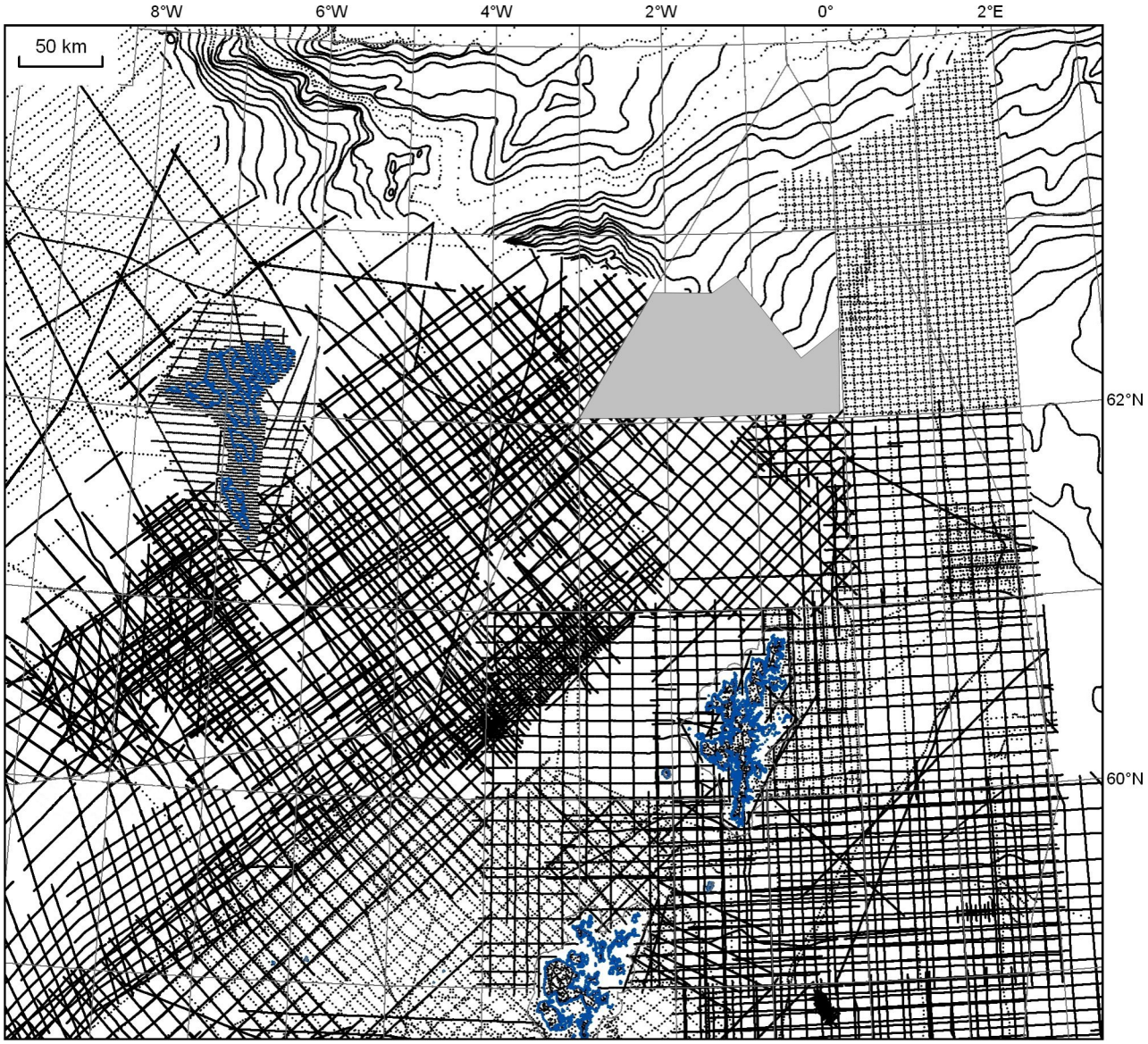

Figure 9 Location of topographic/bathymetric data points. Data sources include: BGS + released Faroese surveys; WesternGeco lines extending into UK waters; surveys conducted by Kort og Matrikelstyrelsen; contours from the GEBCO Digital Atlas (IOC, IHO and BODC, 2003); and the National Geophysical Data Center GLOBE database. The area within the grey polygon was based on data from seismic surveys in the FSC UK database.

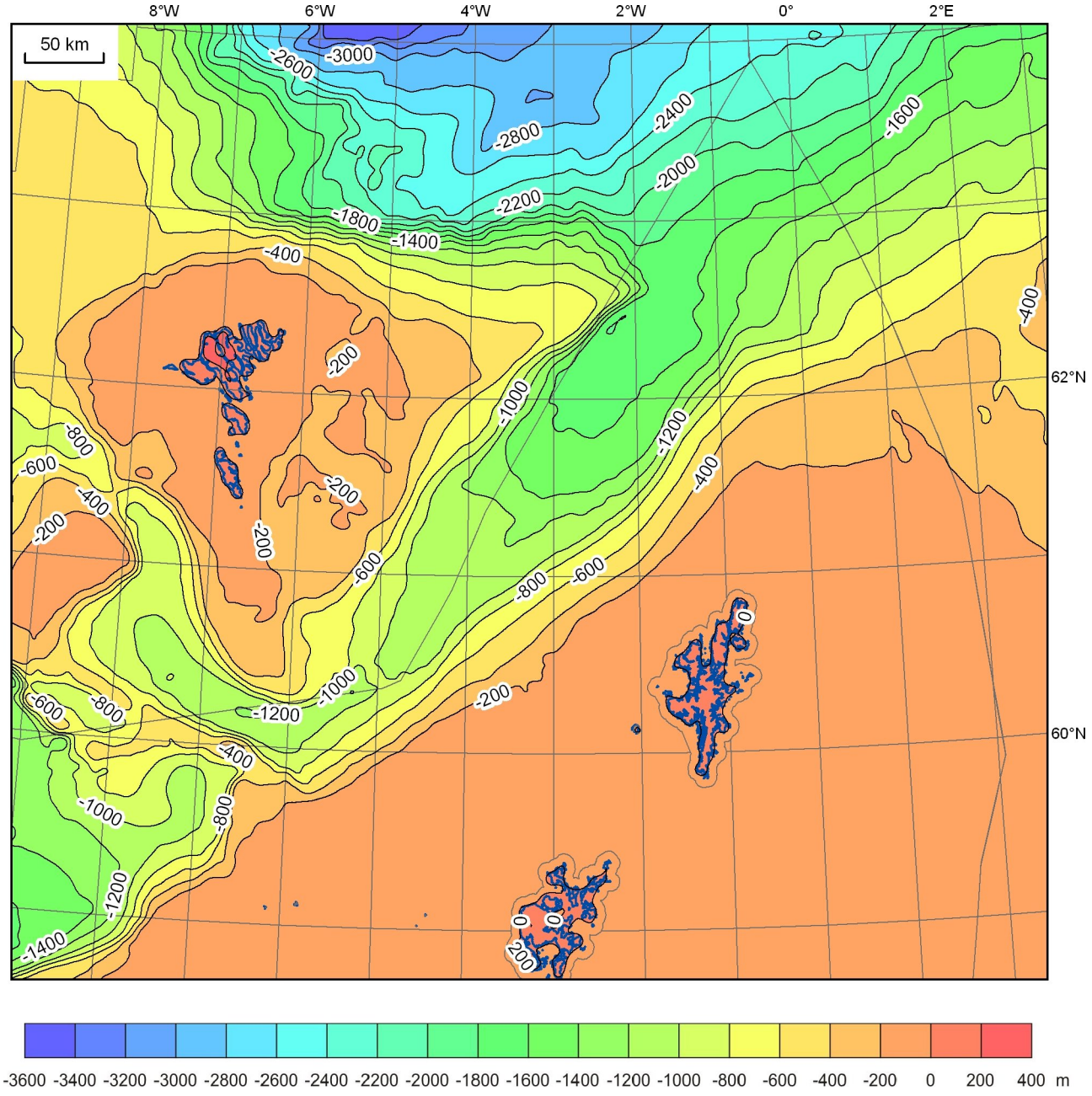

Figure 10 Topographic/bathymetric map of the model area

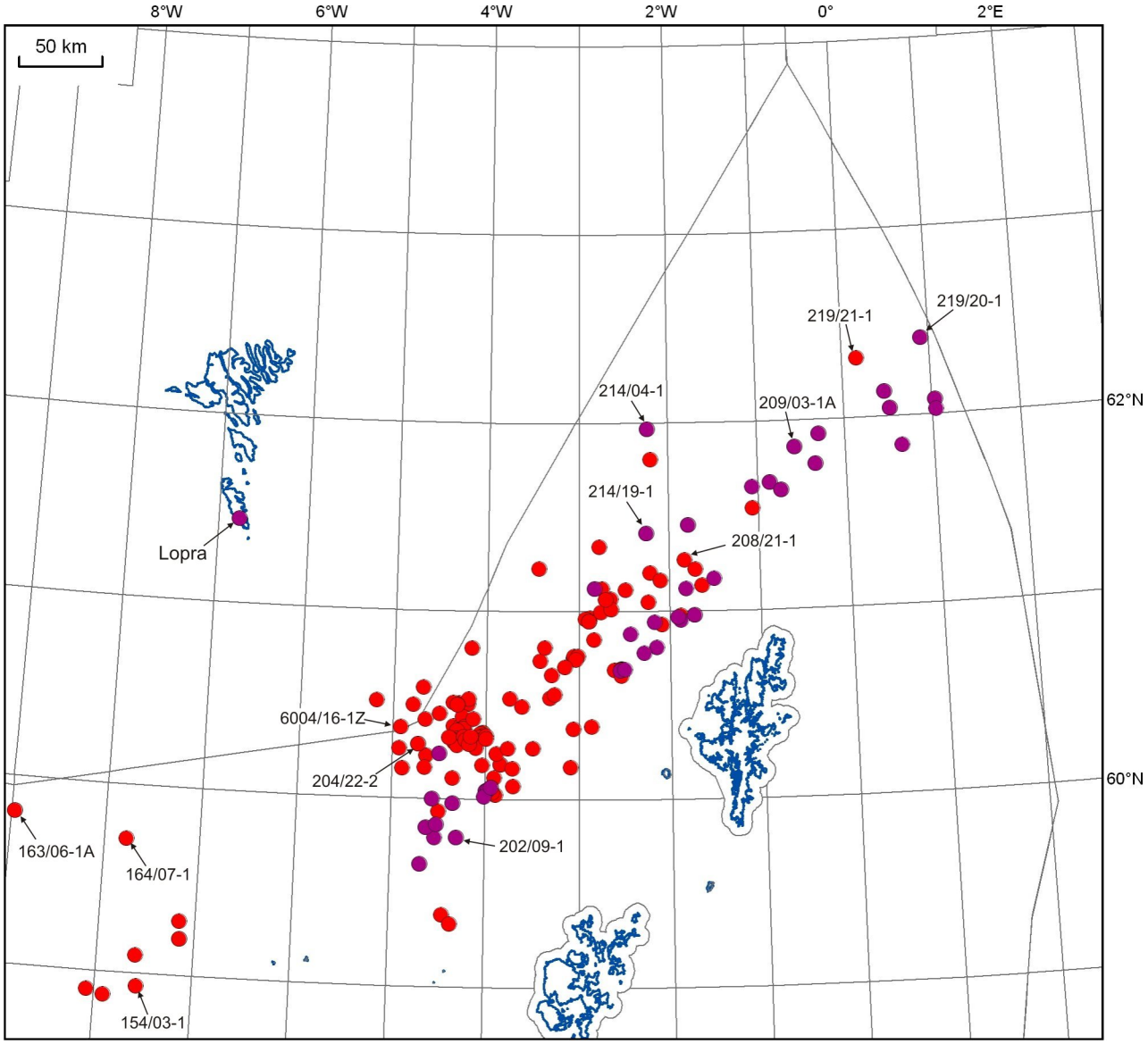

Figure 11 Locations of wells with digital geophysical logs. Wells in purple have vertical seismic profiles. Data from labelled wells are illustrated in other figures in this report.

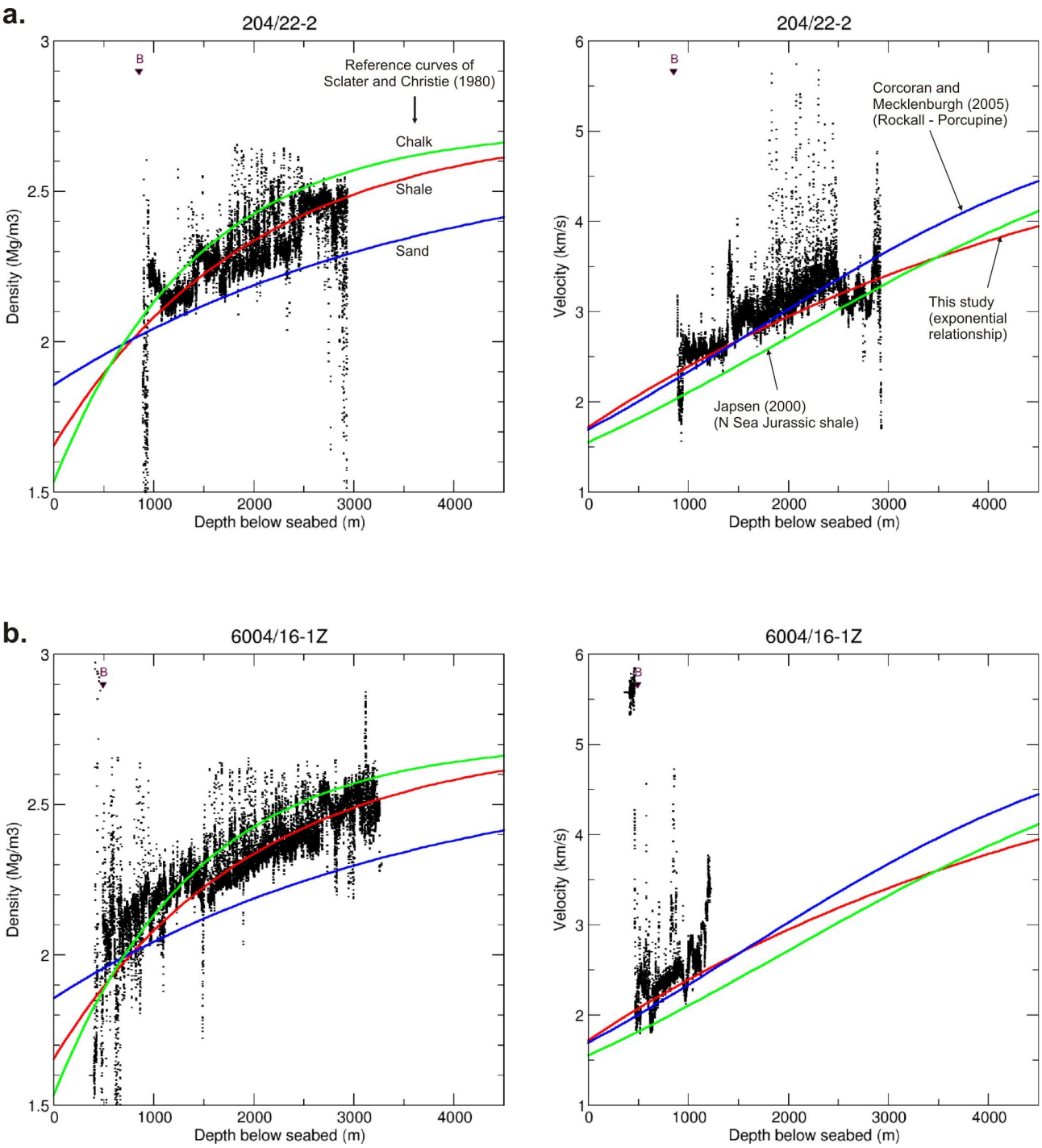

Figure 12 Examples of density and velocity log data from wells in the Faroe-Shetland region (a) 204/22-2, (b) 6004/16-1Z. Alternative compaction curves are included for comparison (labelled in (a)). B = top Balder Formation. For well locations see Figure 11.

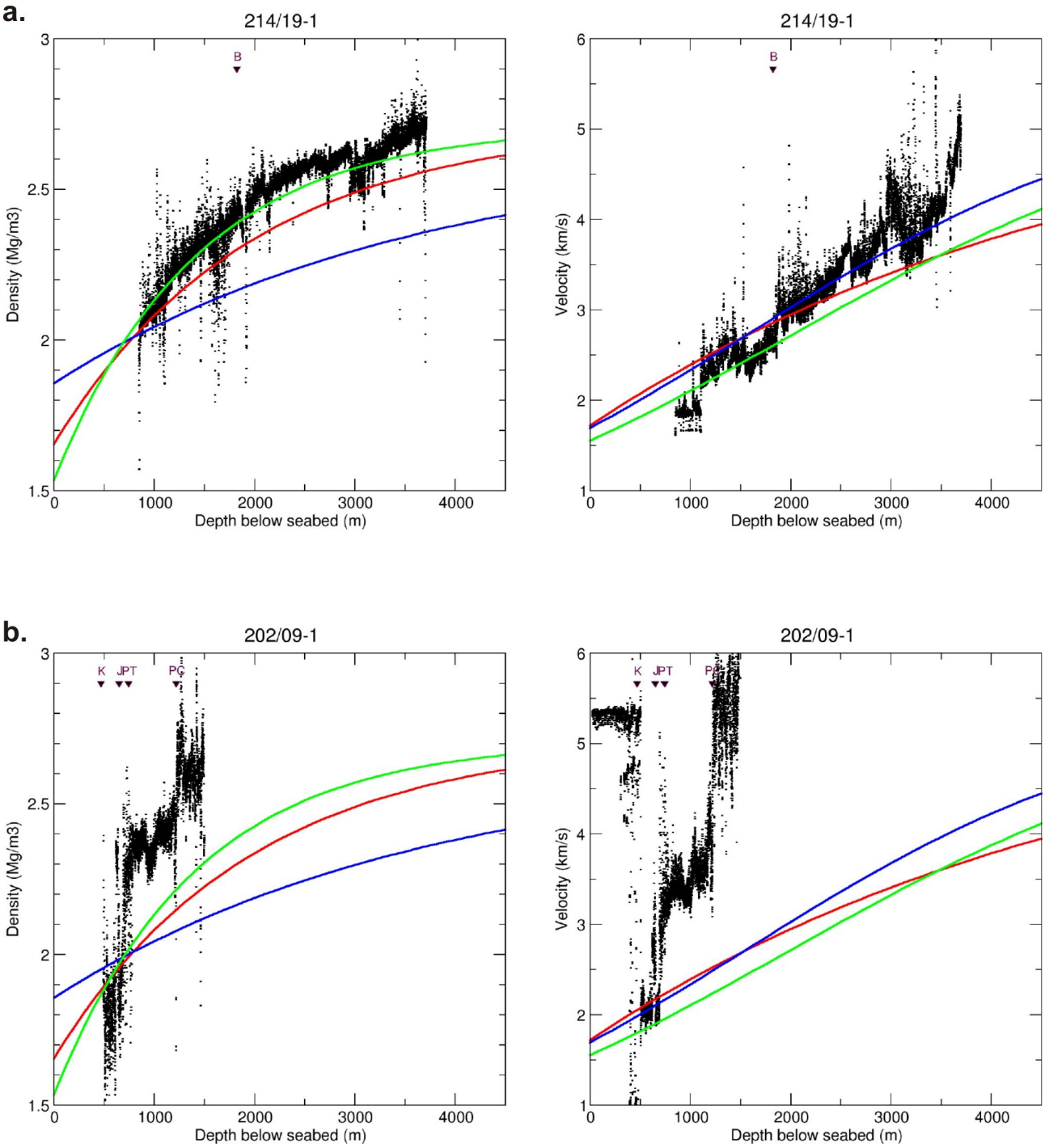

Figure 13 Examples of density and velocity log data from wells in the Faroe-Shetland region (a) 214/19-1, (b) 202/09-1. Alternative compaction curves are included for comparison (see Figure 12a for description). B = Top Balder Formation; J = Top Jurassic; PT = Top Permo-Triassic; PC = Top Precambrian. For well locations see Figure 11.

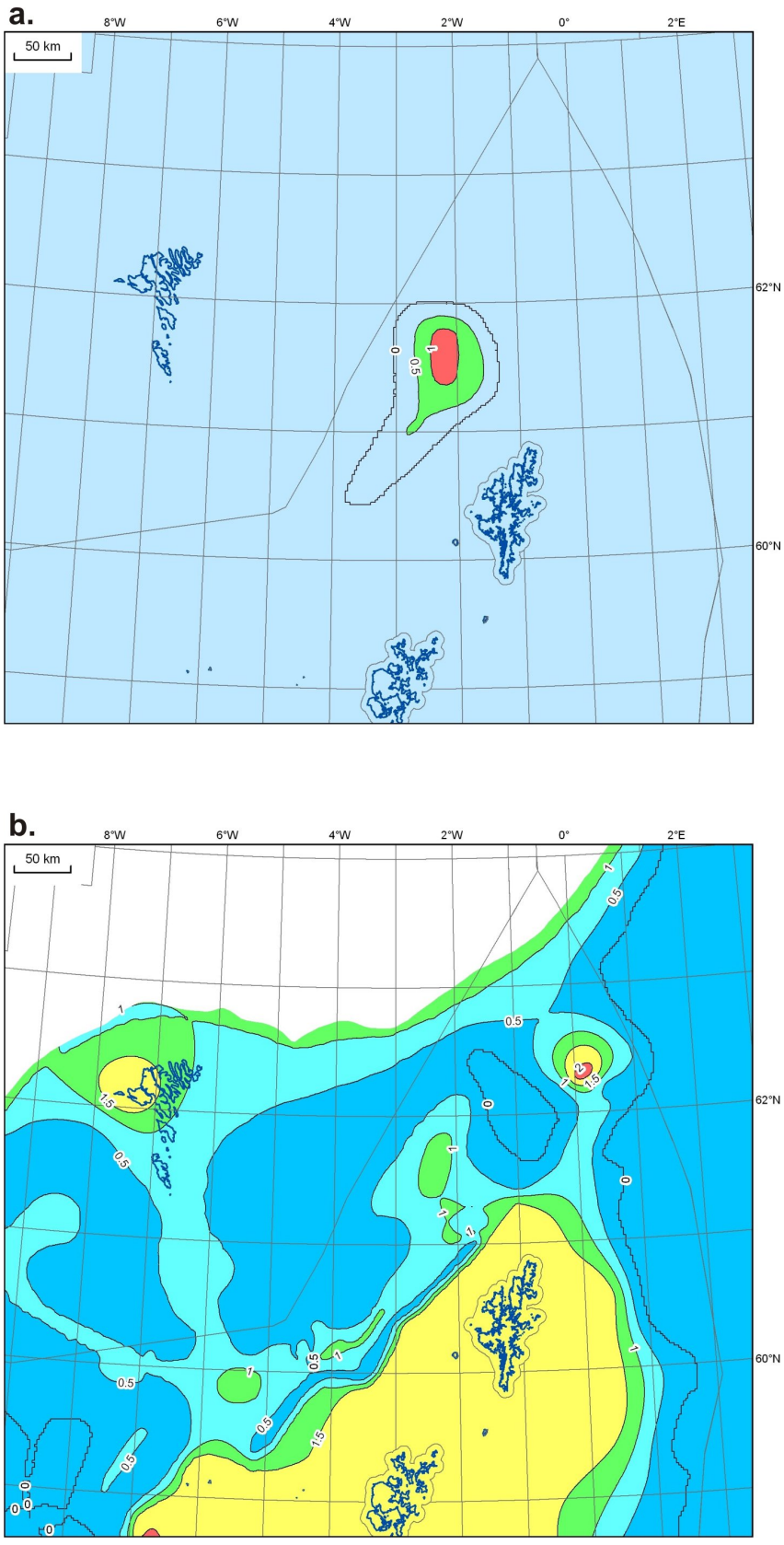

Figure 14 Offsets (in km) applied to the normal density-depth relationship to allow for overcompaction and/or lithological factors in (a) pre-volcanic Cenozoic sedimentary rocks, and (b) pre-Cenozoic sedimentary rocks.

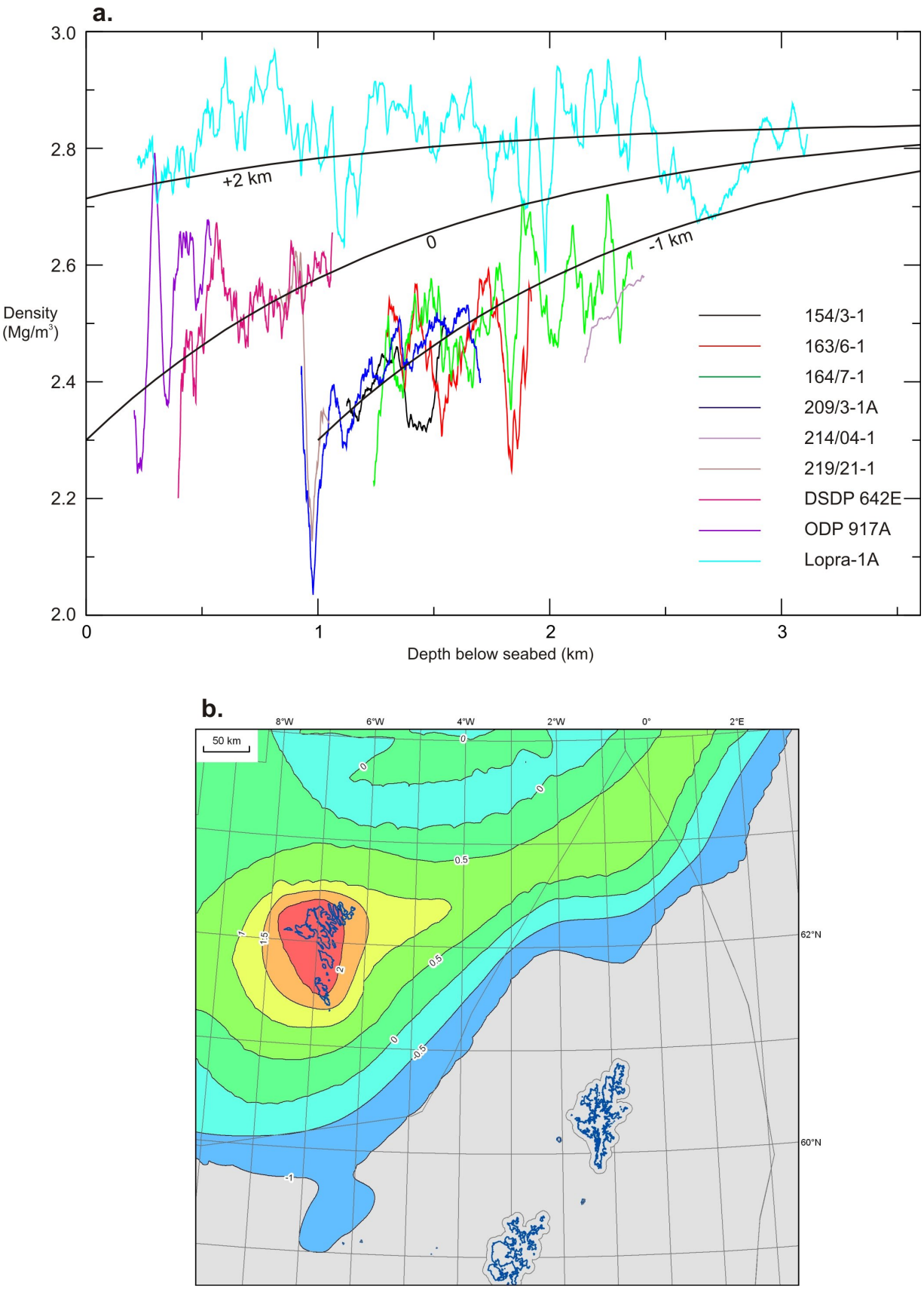

Figure 15 (a) Density logs through volcanic sequences in the Faroe-Shetland and north Rockall areas. Data have been smoothed by application of a 50 m moving average filter. (b) Map of assumed offset to the nominal reference curve (indicated by the black line with zero offset in (a)). For well locations see Figure 11.

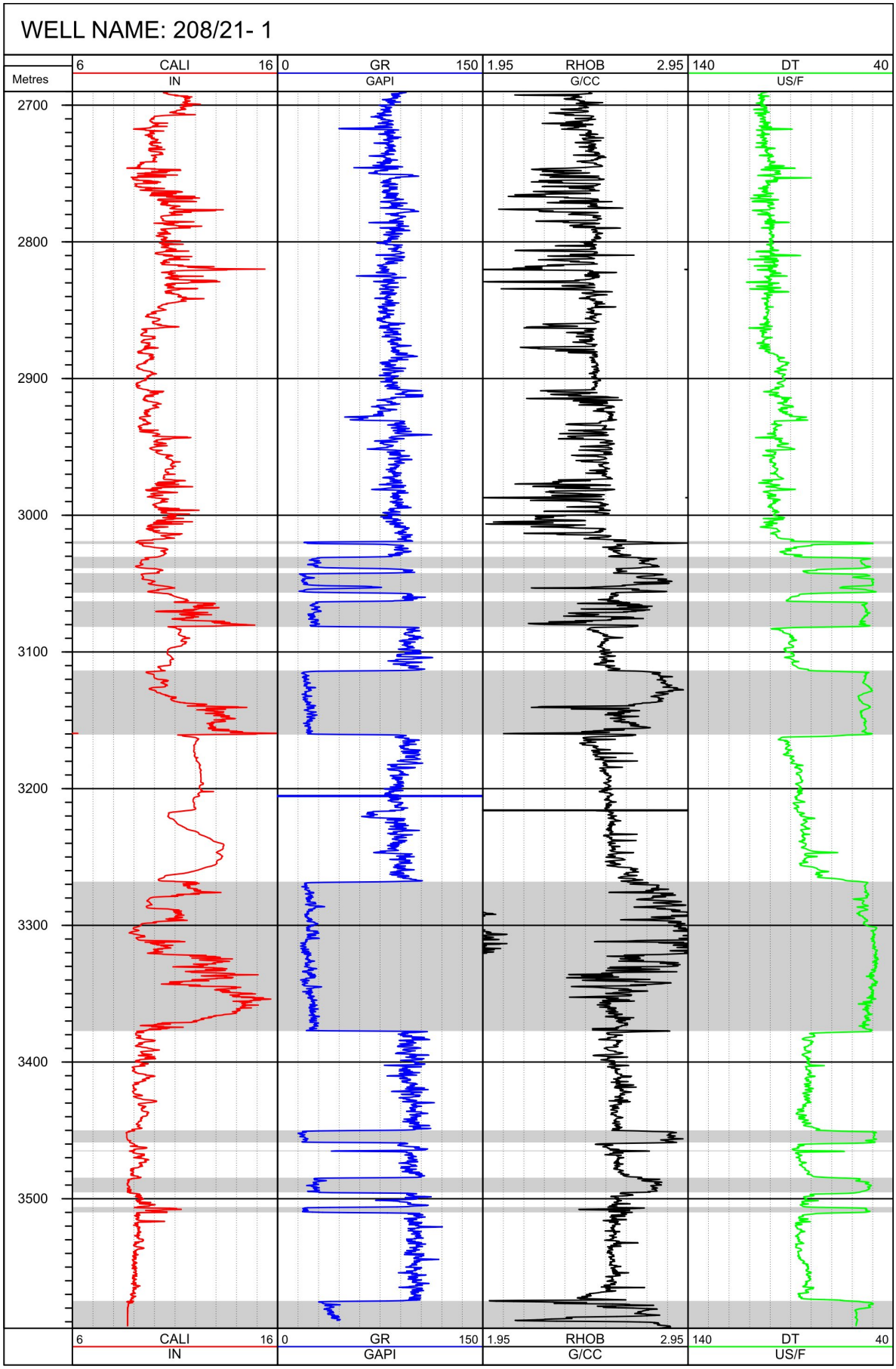

Figure 16 Geophysical logs through sills (indicated by grey bands) in well 208/21-1. CALI = caliper; GR = gamma ray; RHOB = density; DT = sonic transit time. Well location in Figure 11.

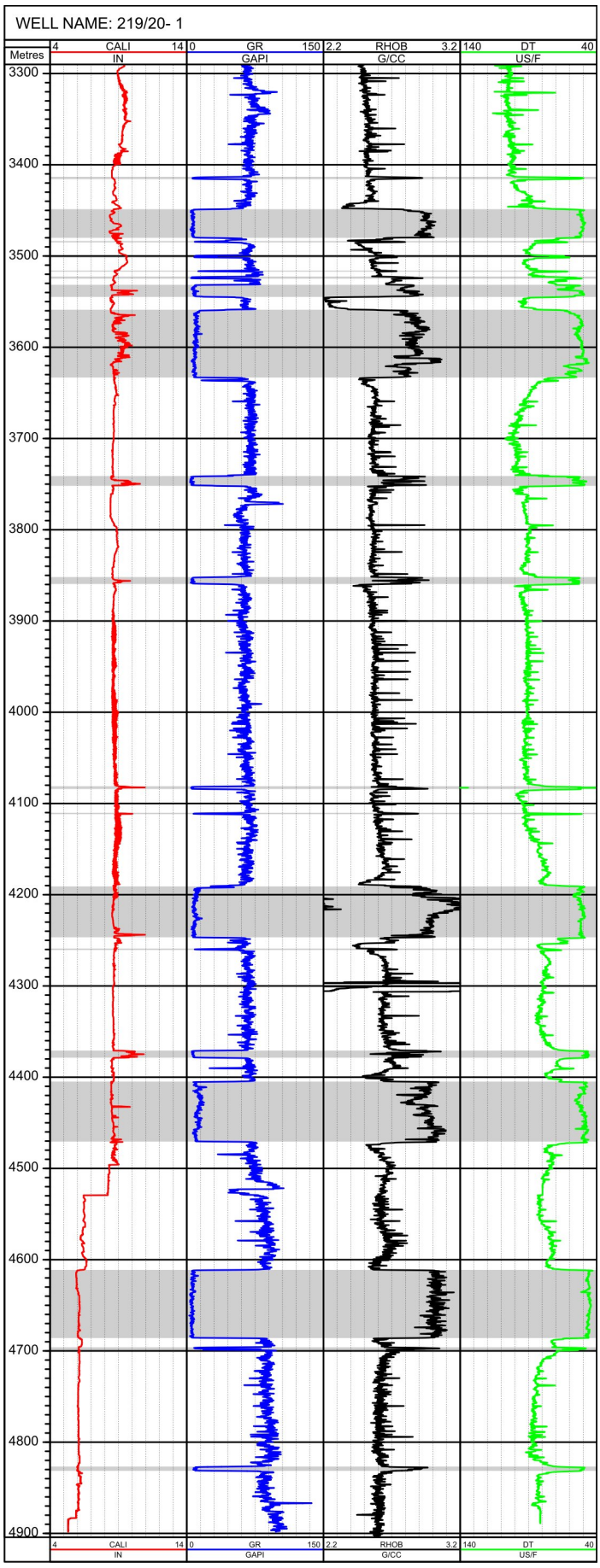

Figure 17 Geophysical logs through sills (indicated by grey bands) in well 219/20-1. CALI = caliper; GR = gamma ray; RHOB = density; DT = sonic transit time. Well location in Figure 11.

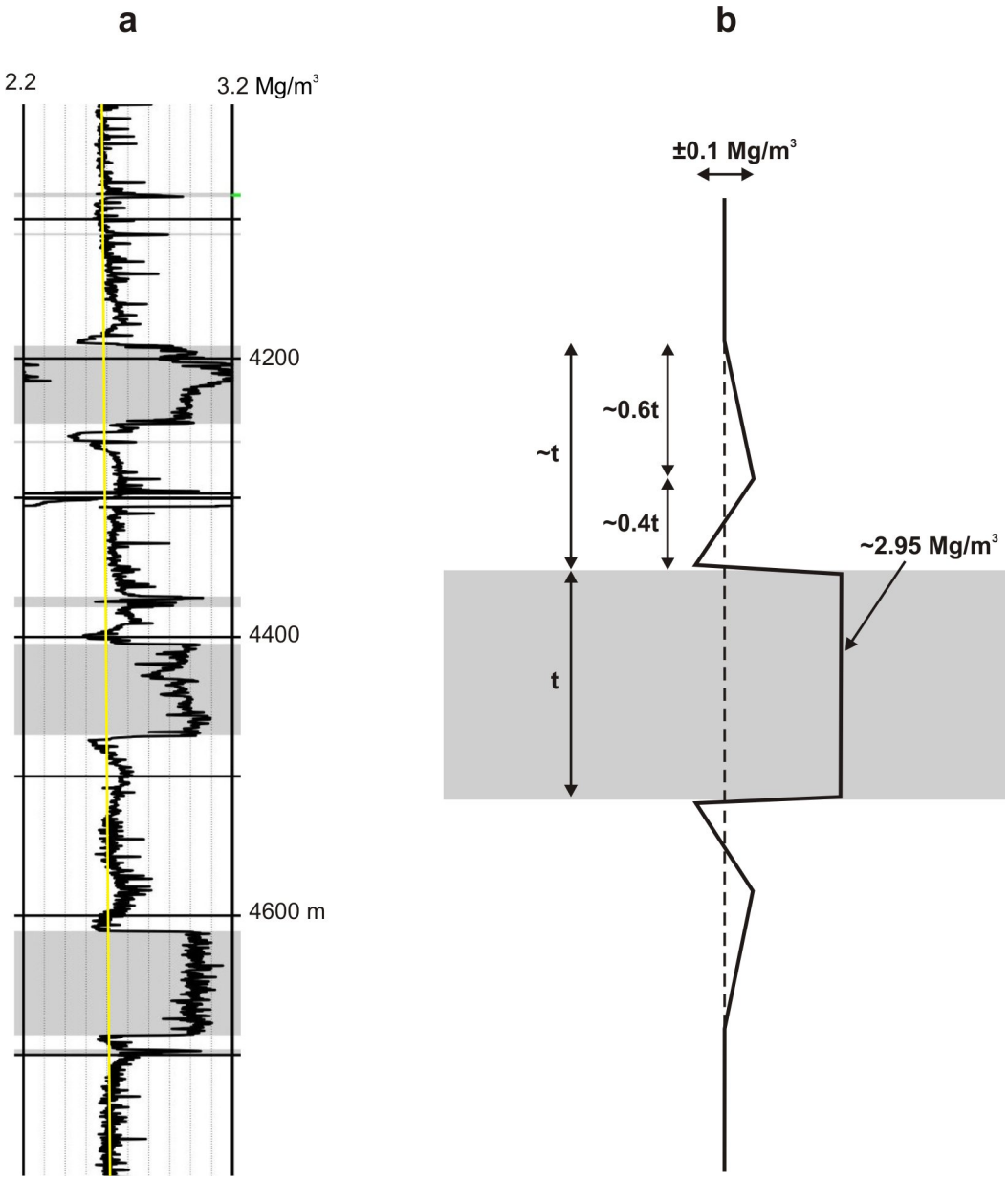

Figure 18 (a) Detail of density log through lower sills in 219/20-1. The yellow line indicates the approximate 'baseline' density trend within sedimentary rocks away from the sill margins. (b) Schematic representation of density variation across a sill and adjacent country rock.

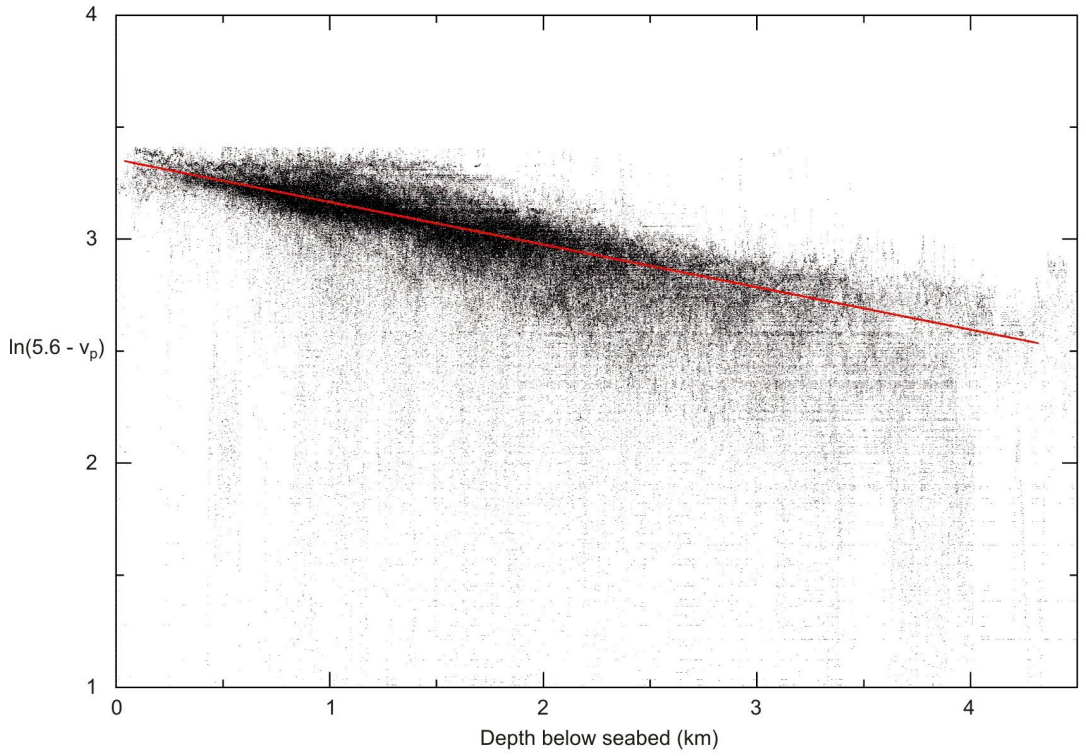

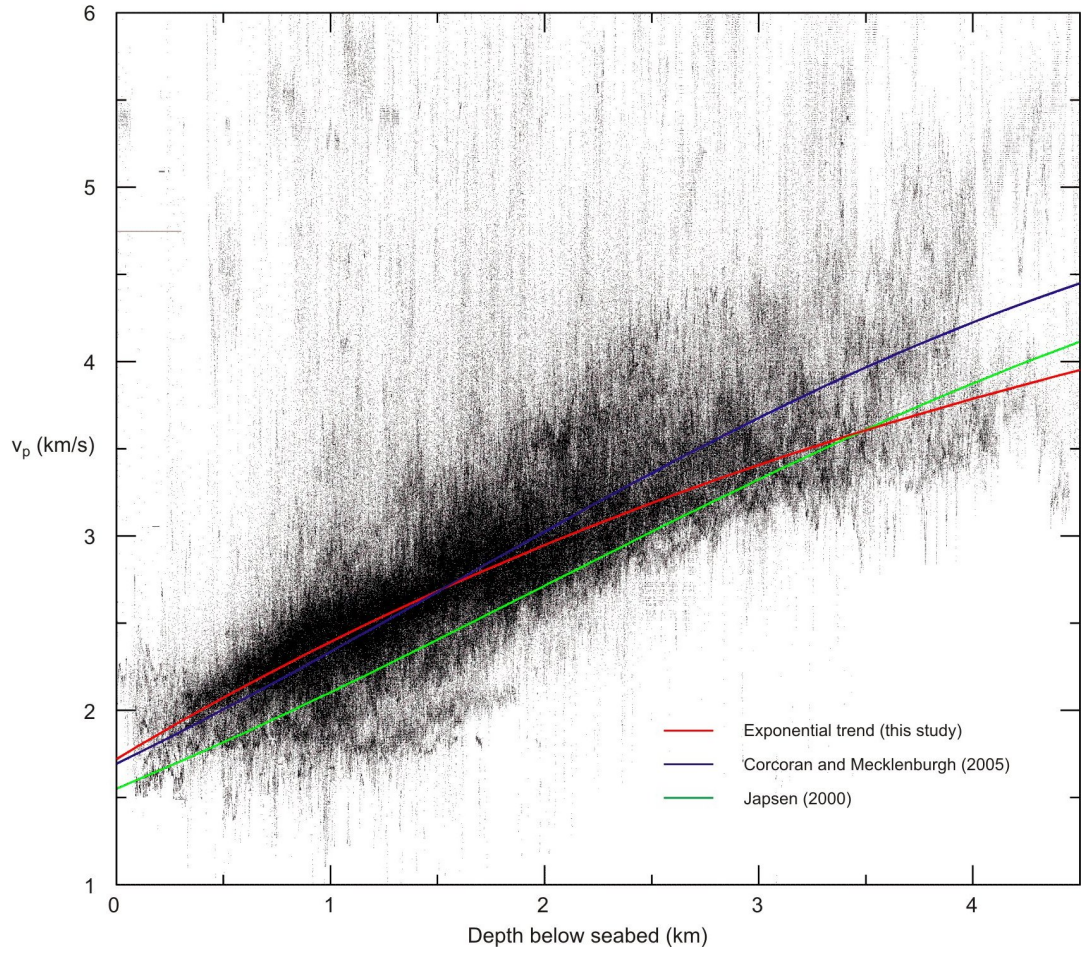

Figure 19 Merged velocity data from wells in the Faroe-Shetland region plotted on a logarithmic scale (top panel) and as a conventional velocity-depth relationship (bottom panel). The red lines in the two panels are equivalent.

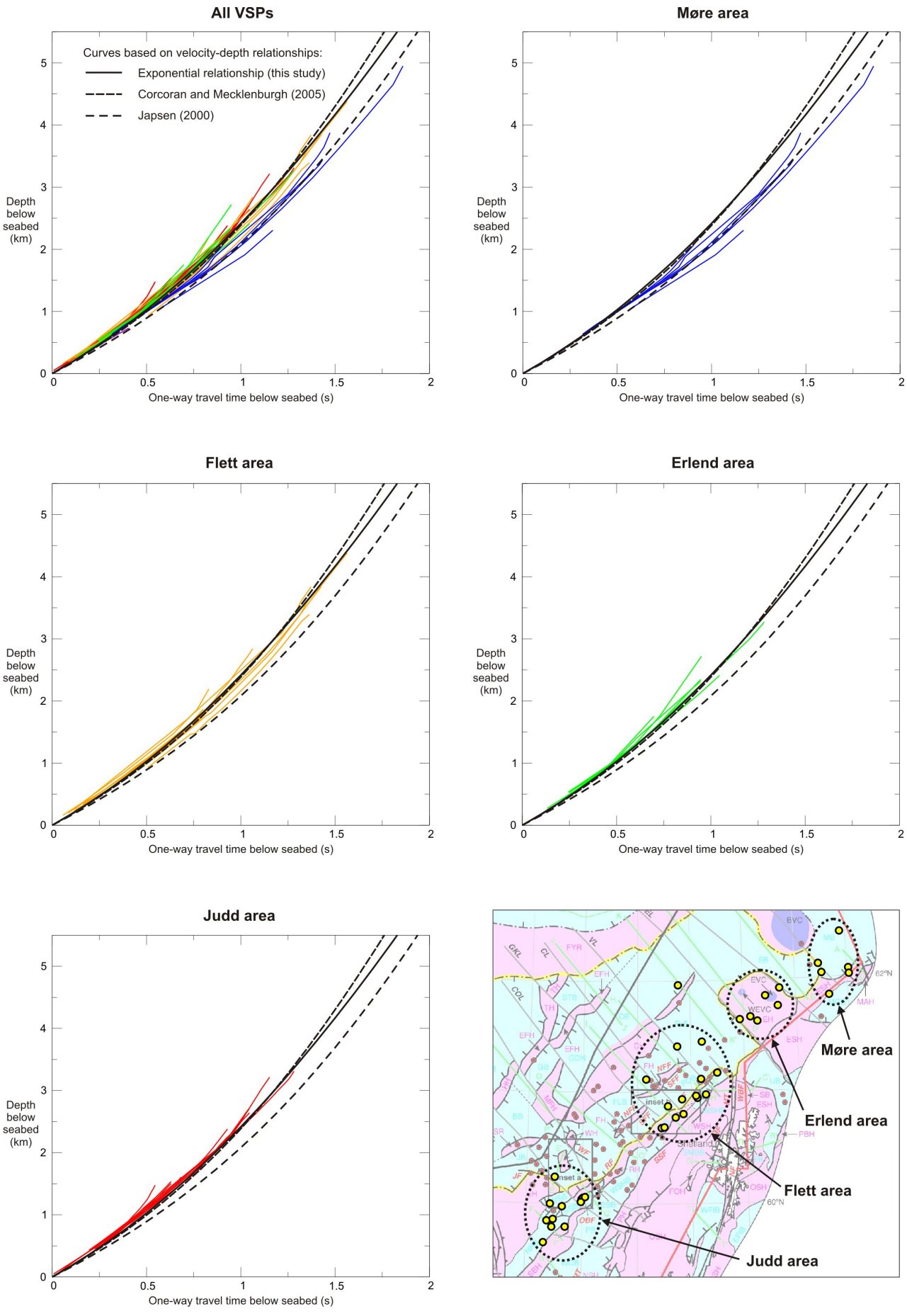

Figure 20 Vertical seismic profiles (coloured lines) from the Faroe-Shetland region compared with different reference curves.

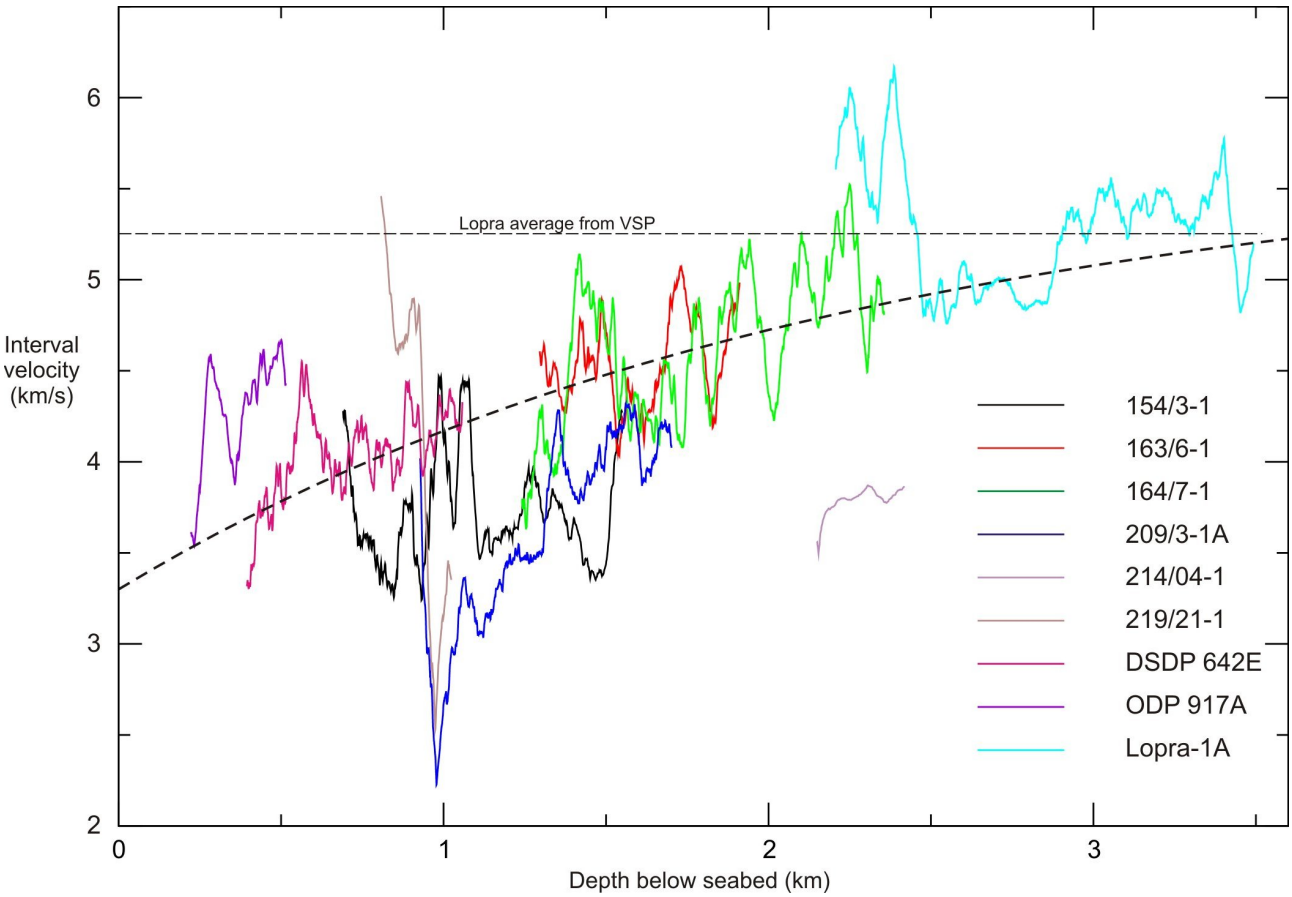

Figure 21 Velocity profiles through volcanic sequences in the Faroe-Shetland and north Rockall areas. Slowness data were smoothed using a 50 m moving average filter prior to conversion to velocity. The dashed line is the nominal velocity-depth relationship assumed in the depth conversion.

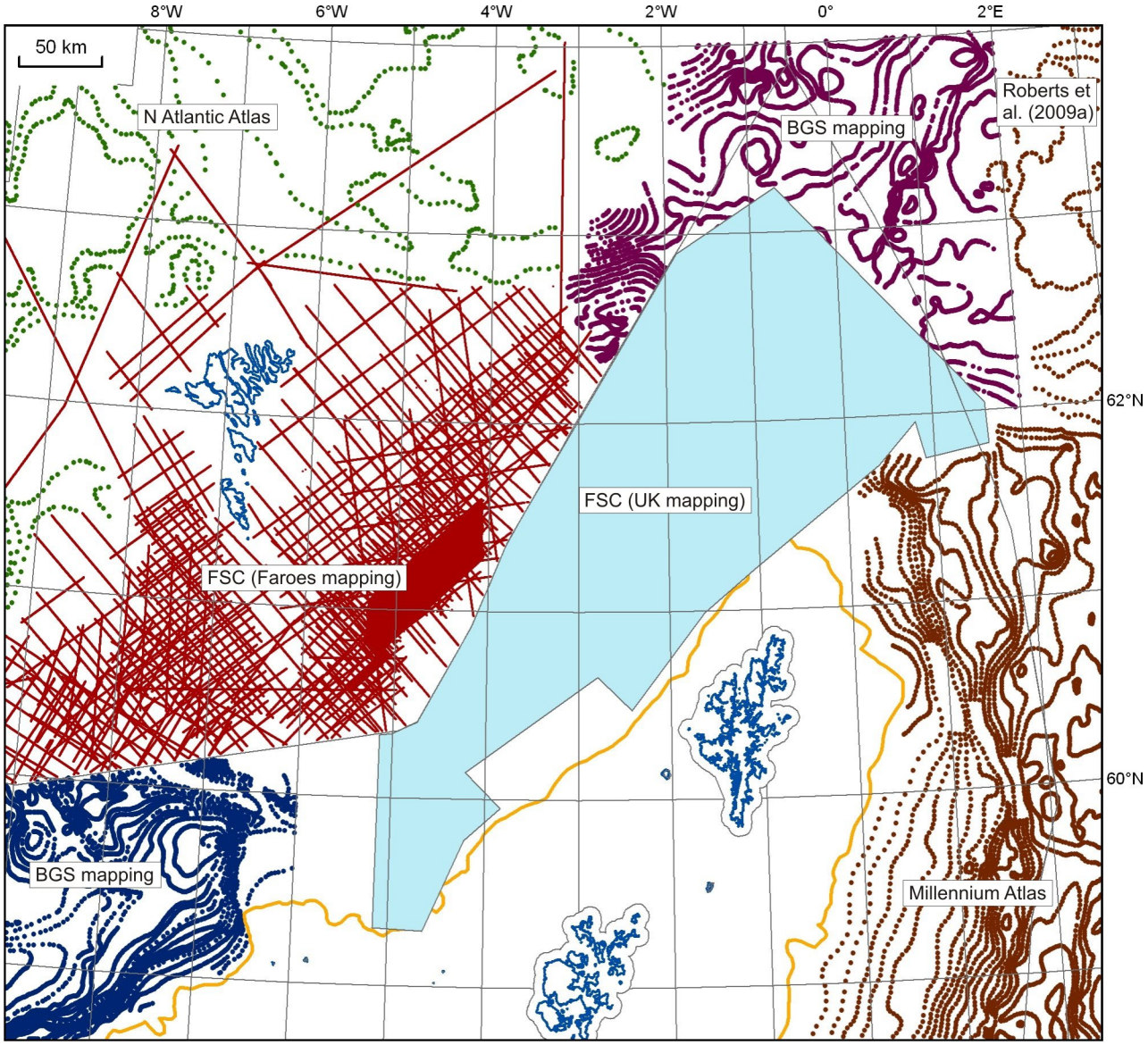

Figure 22 Data sources for the top volcanics / top Balder Formation compilation

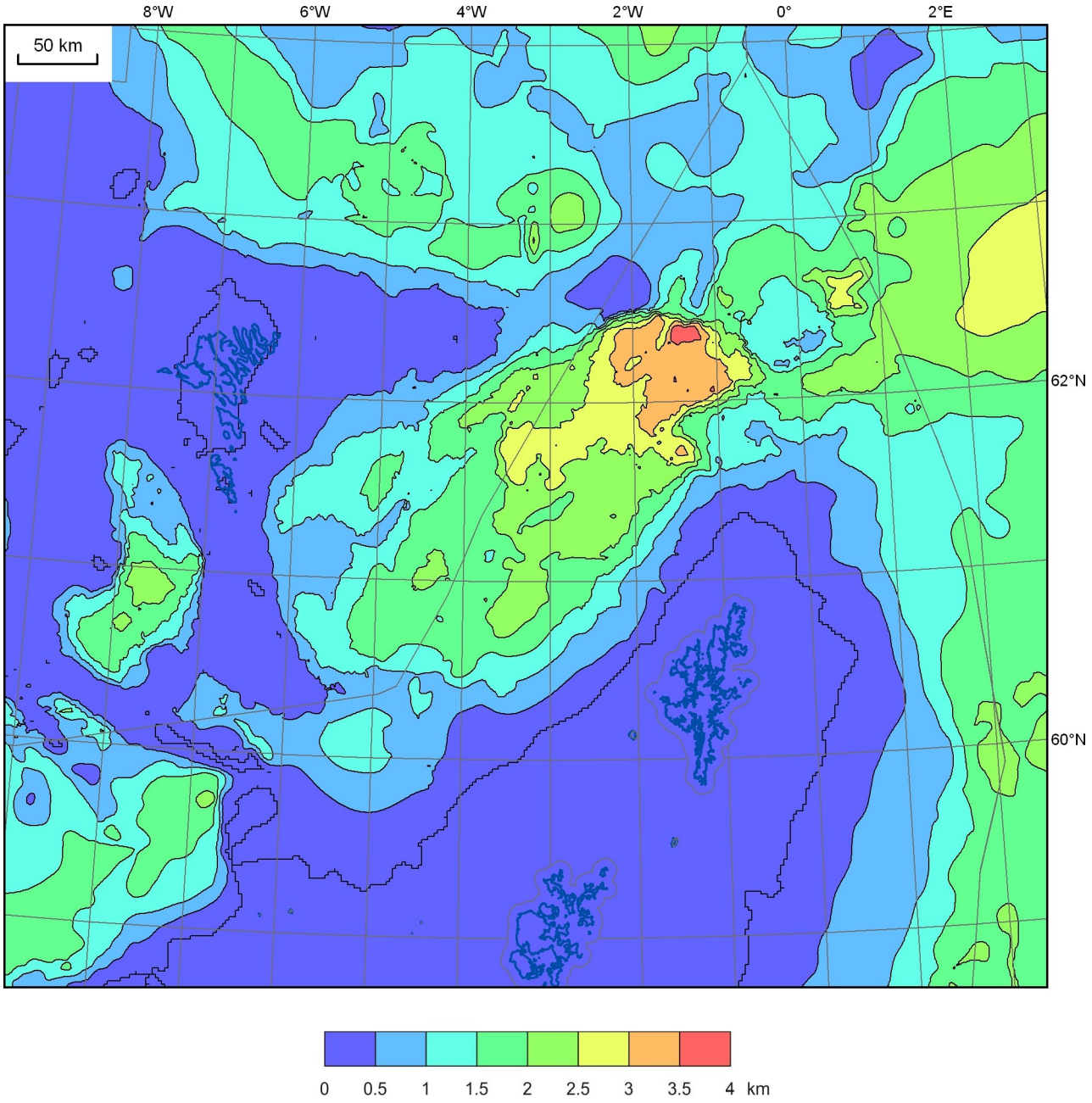

Figure 23 Thickness of post-volcanic sedimentary rocks

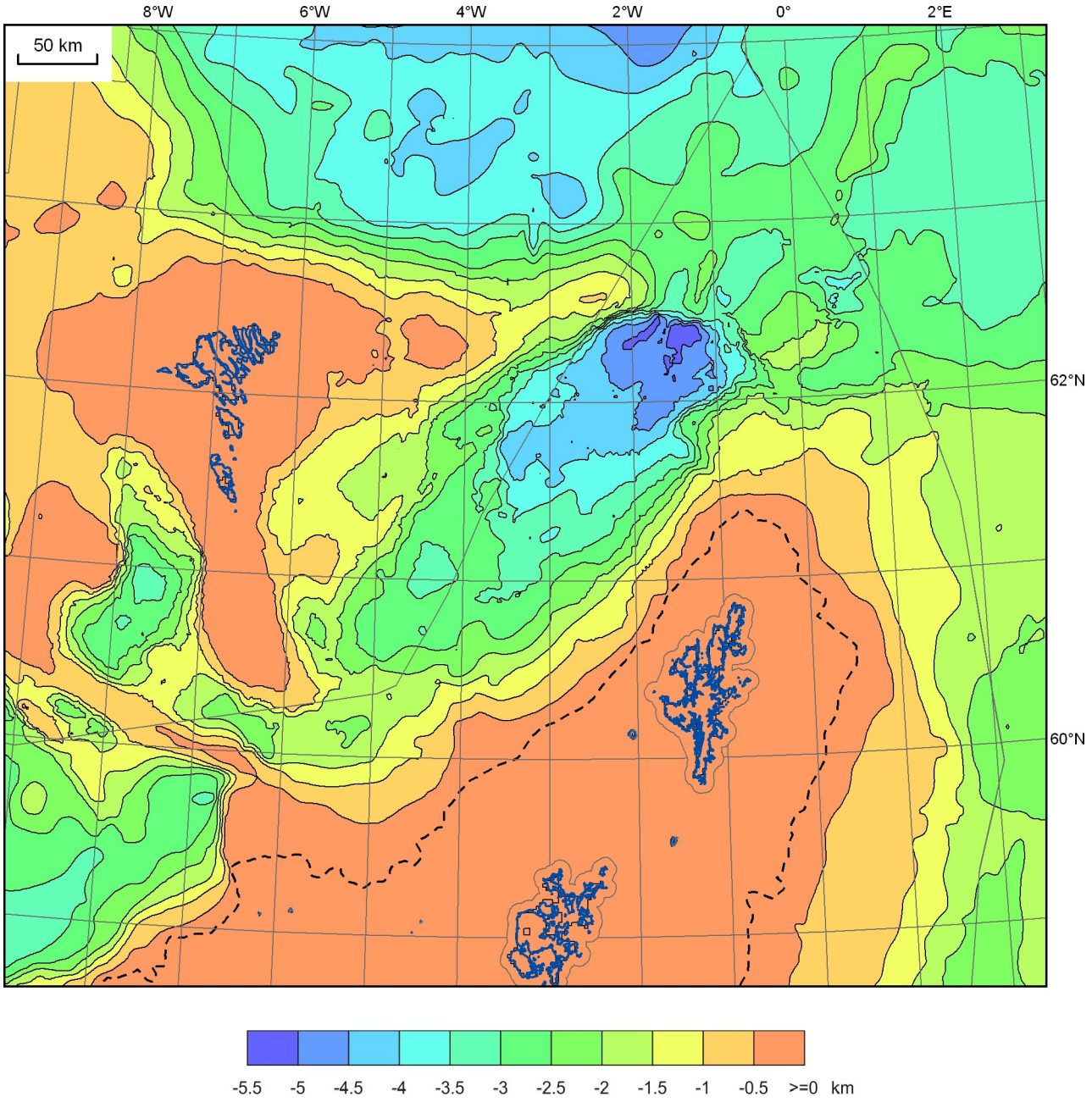

Figure 24 Top volcanics / Balder Formation. The dashed line indicates the limit of this unit in the Orkney - Sheltland area.

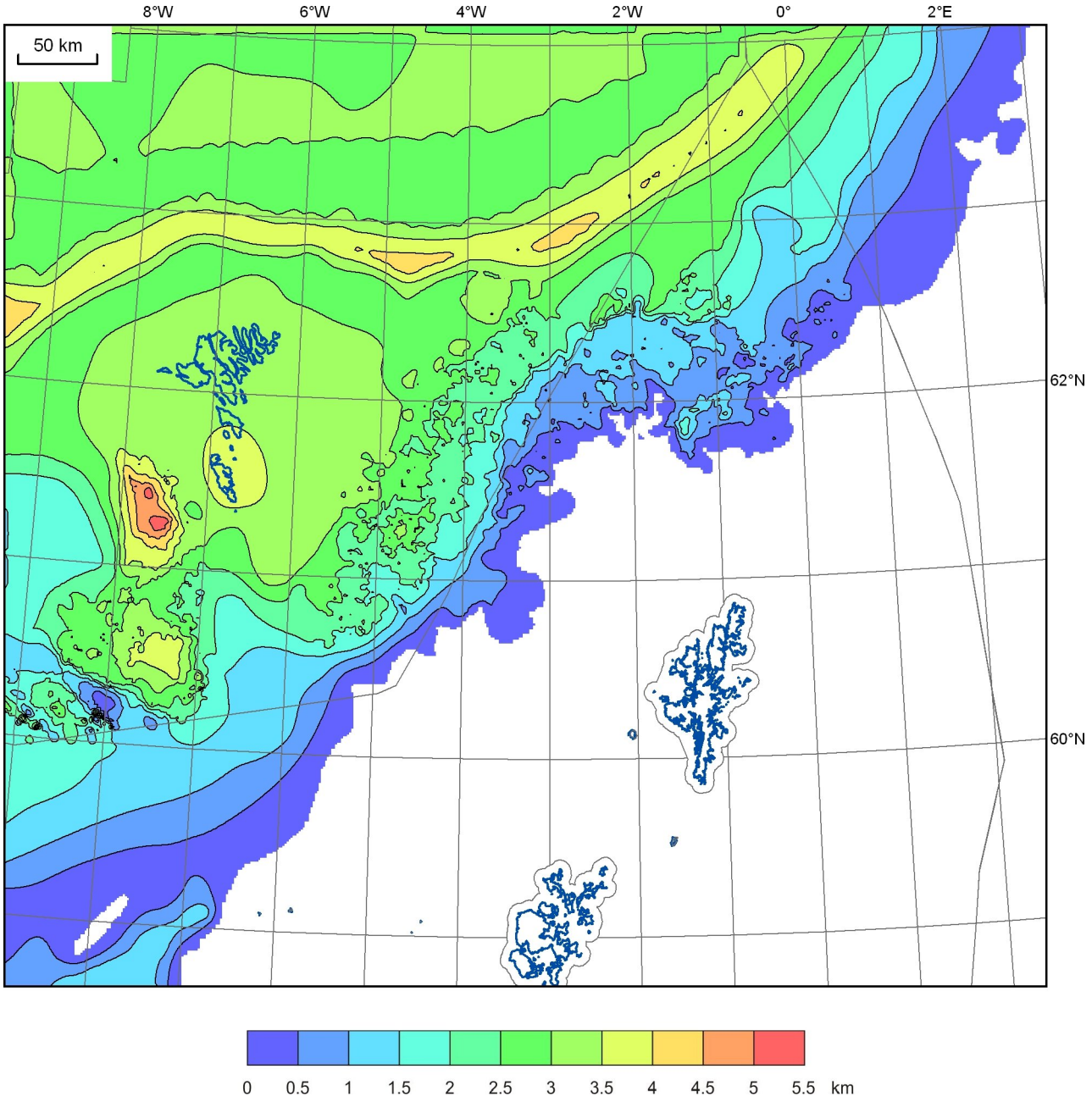

Figure 25 Thickness of volcanic sequence (+ oceanic layer 2)

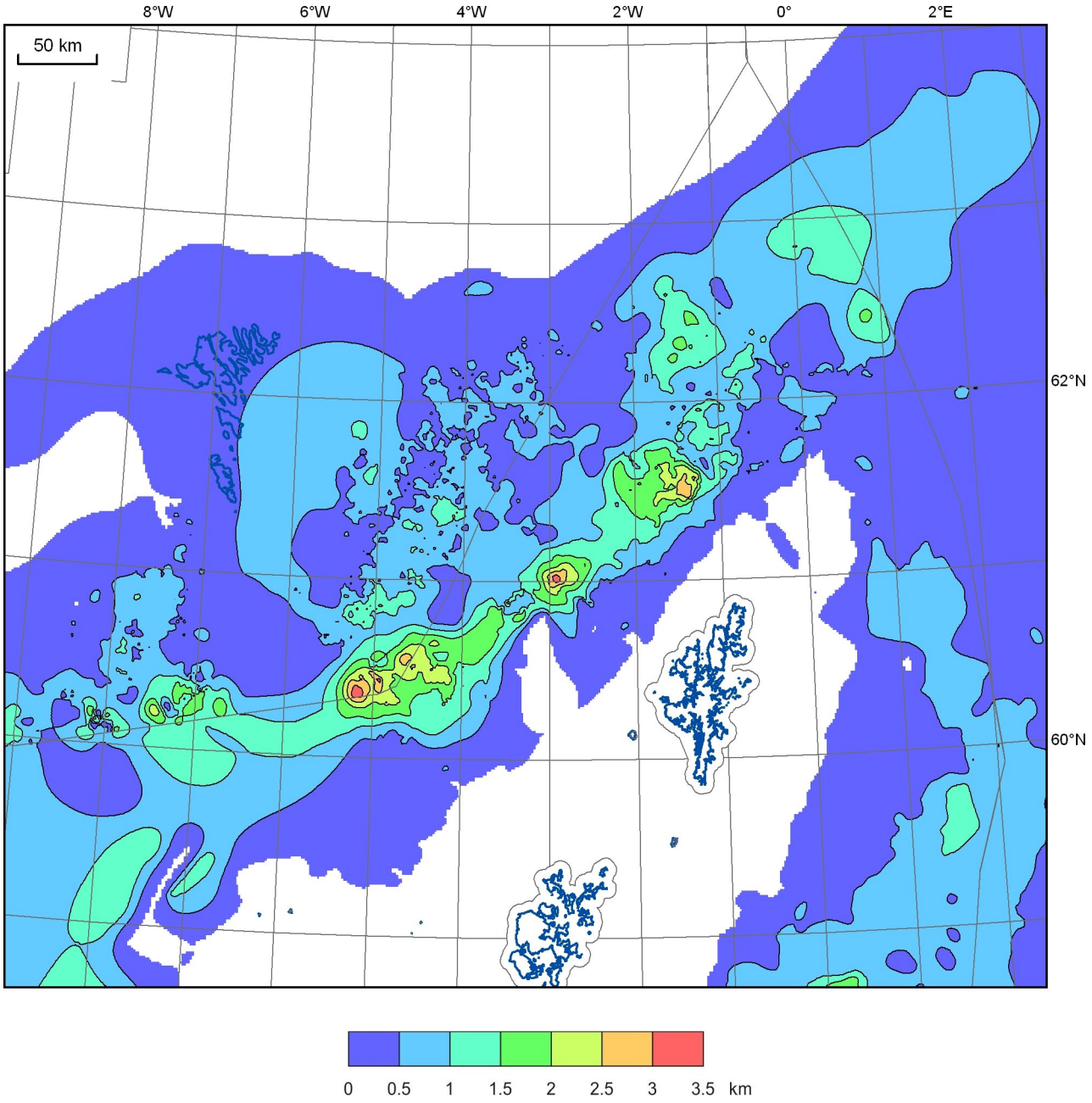

Figure 26 Thickness of pre-volcanic sedimentary rocks

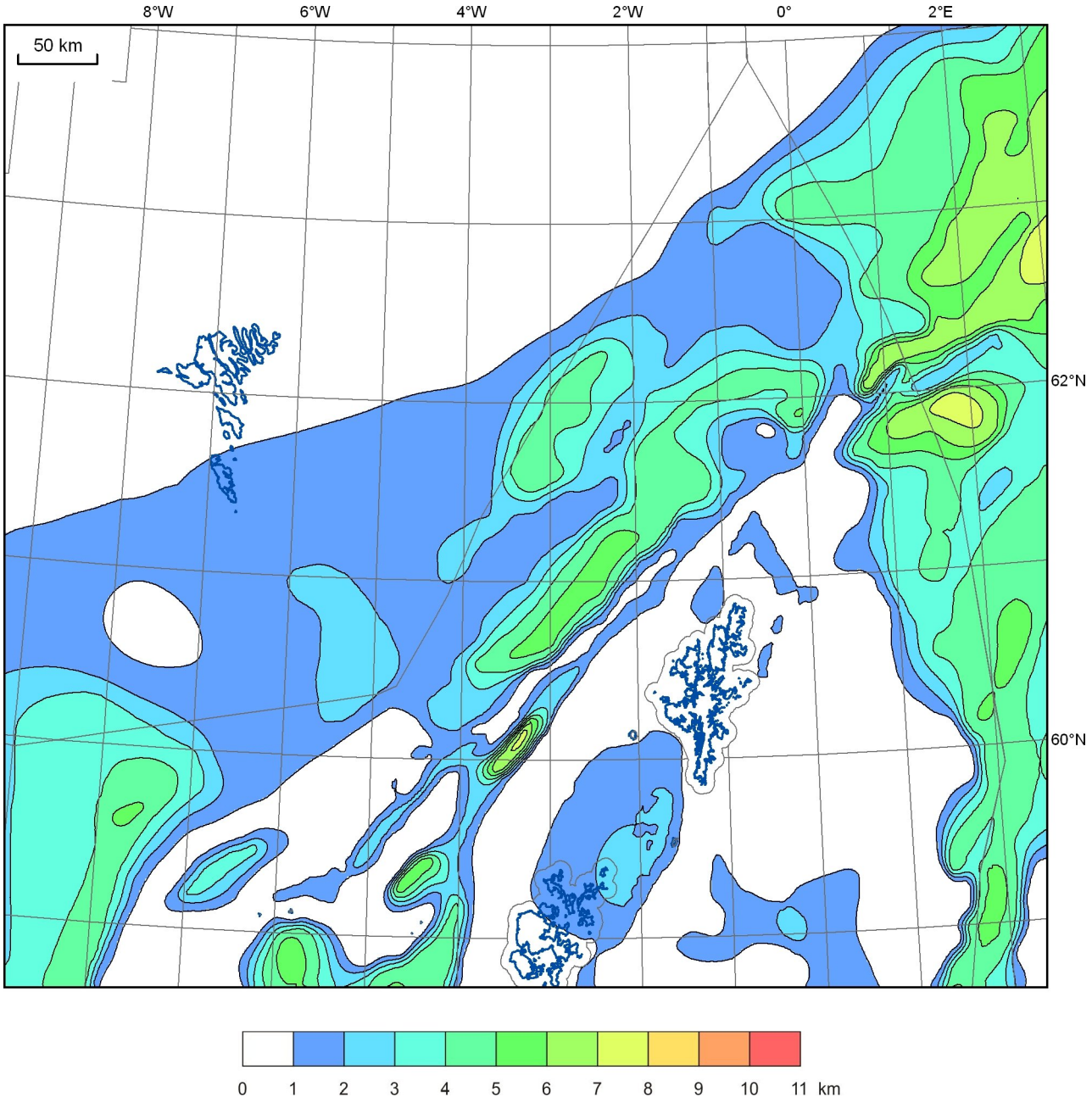

Figure 27 Initial model for the thickness of the pre-Cenozoic sedimentary rocks

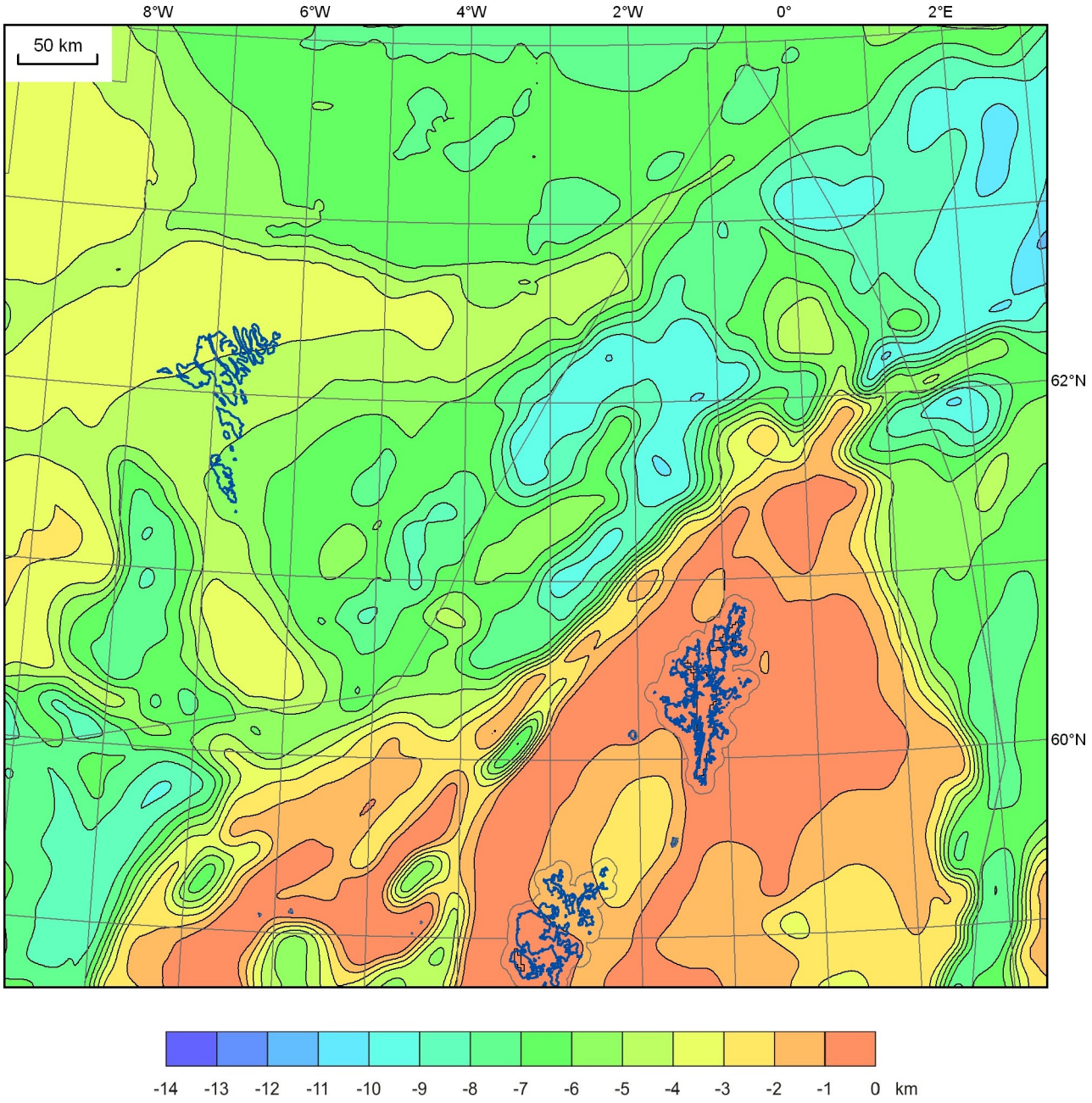

Figure 28 Initial model for the depth to top basement

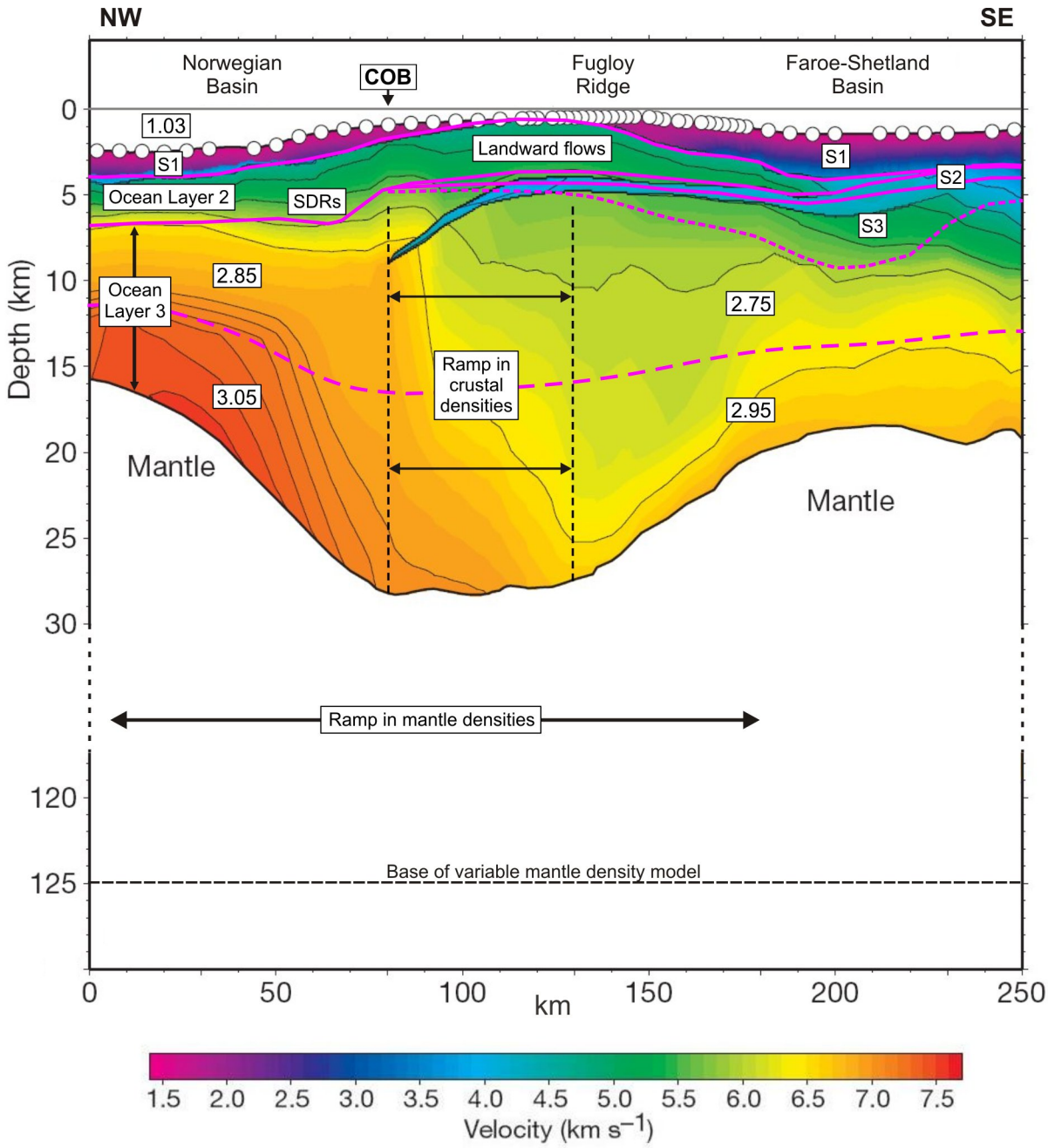

Figure 29 Schematic horizons from the 3D model superimposed on the iSIMM velocity model of White et al. (2008; adapted by permission from Macmillan Publishers Ltd., Nature, Vol. 452, p. 461). Sedimentary units: S1 = post-volcanic sediments; S2 = pre-volcanic Cenozoic sediments; S3 = pre-Cenozoic sediments. Numbers indicate densities in Mg/m^3. COB = continent-ocean boundary.

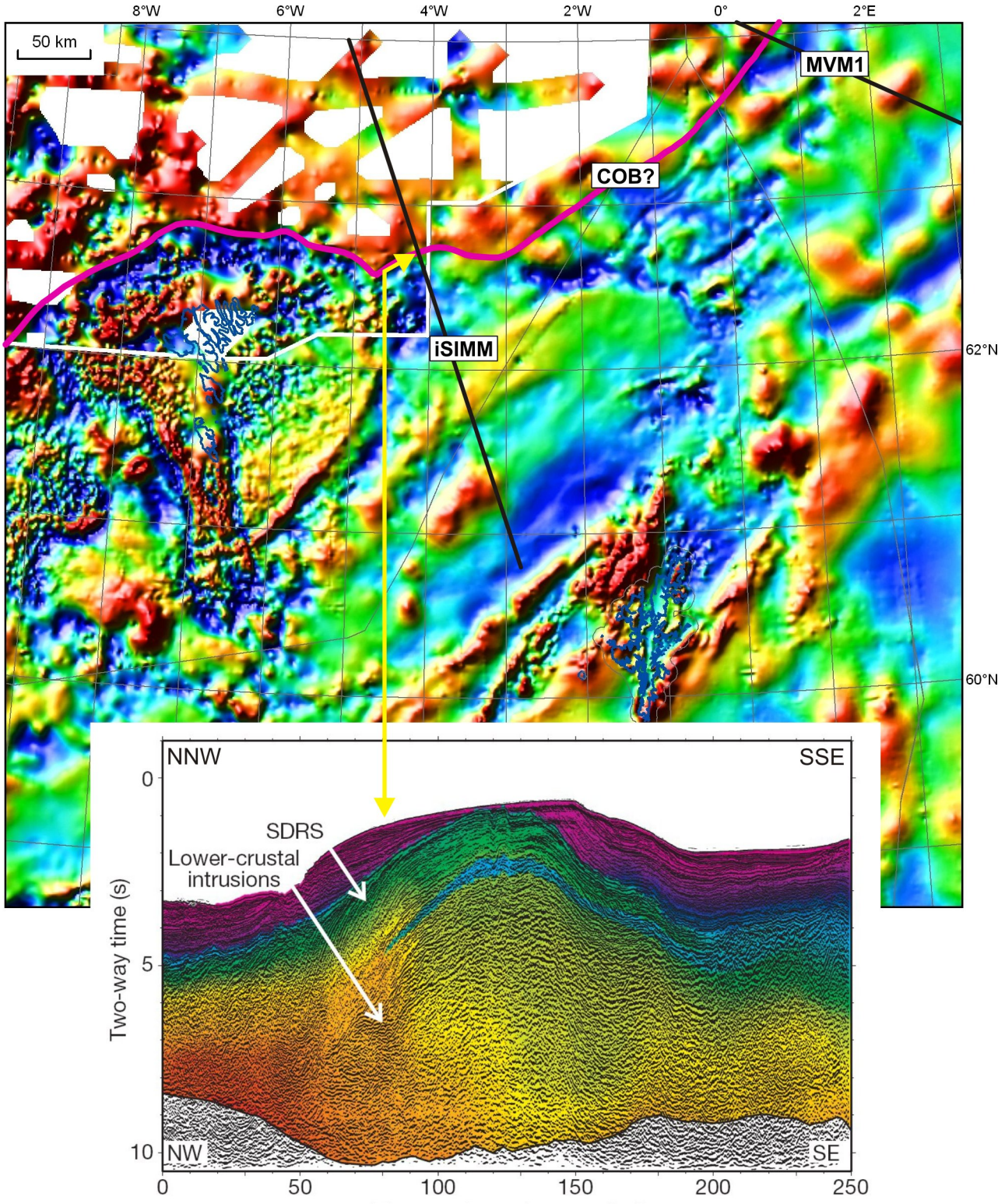

Figure 30 Magnetic image showing the assumed location of the continent-ocean boundary, constrained by the iSIMM and MVM1 seismic transects and interpolated/extrapolated using the magnetic anomaly pattern. The iSIMM seismic reflection section and velocity model (colours) is from White et al. (2008); see Figure 29 for colour scale and acknowledgments.

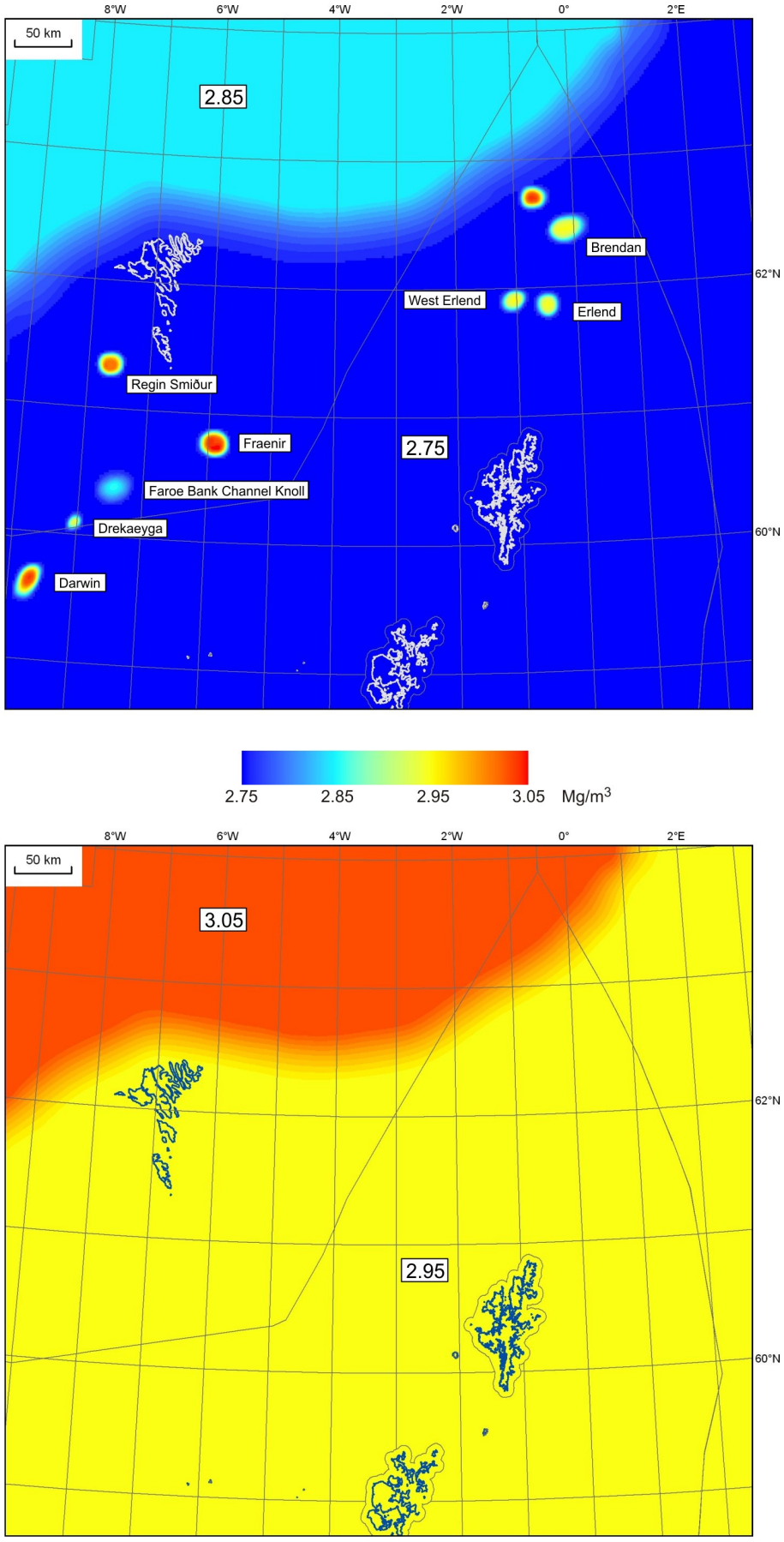

Figure 31 Assumed densities for the upper (top panel) and lower (bottom panel) crust

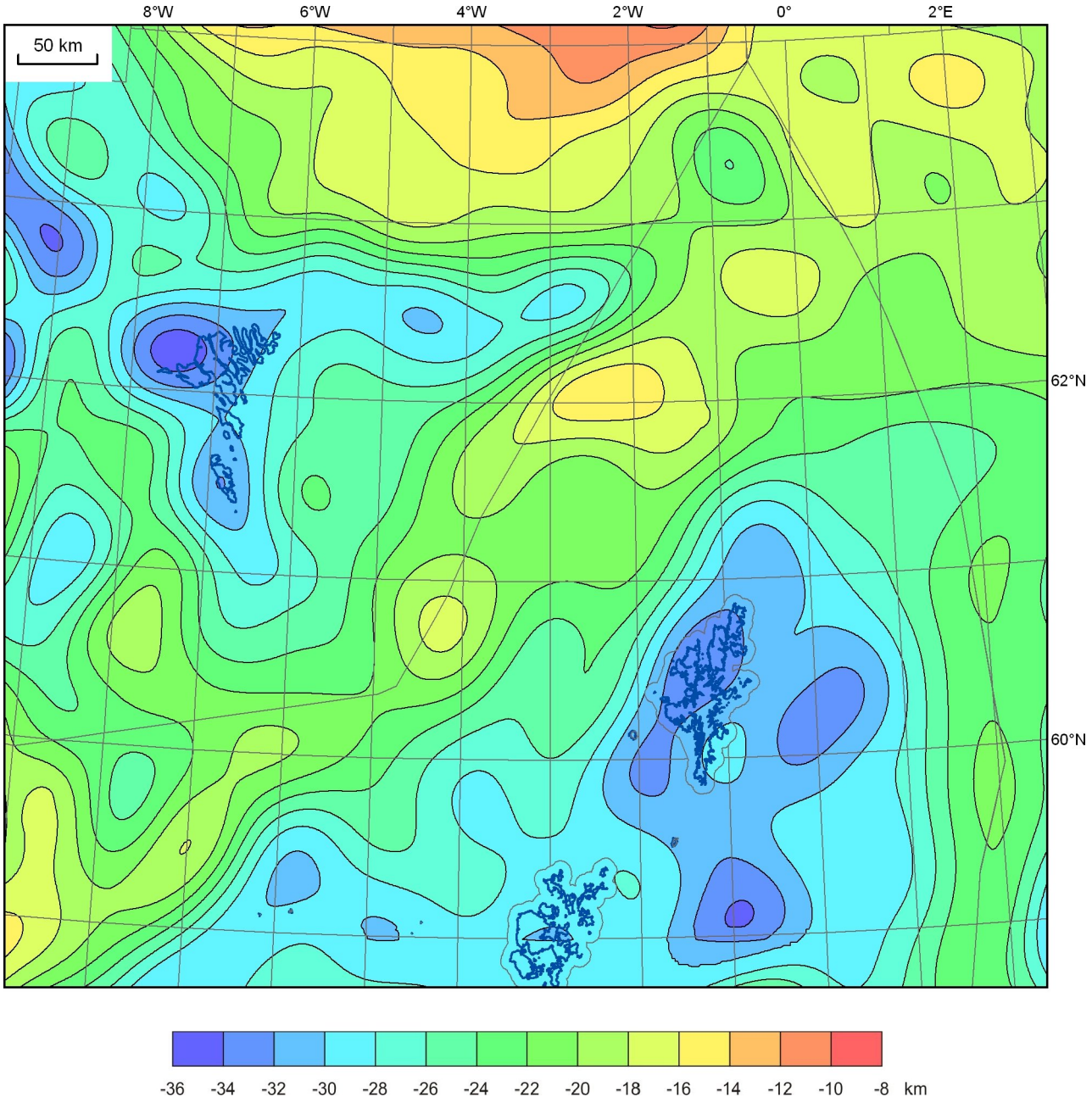

Figure 32 Depth to Moho in the optimised model

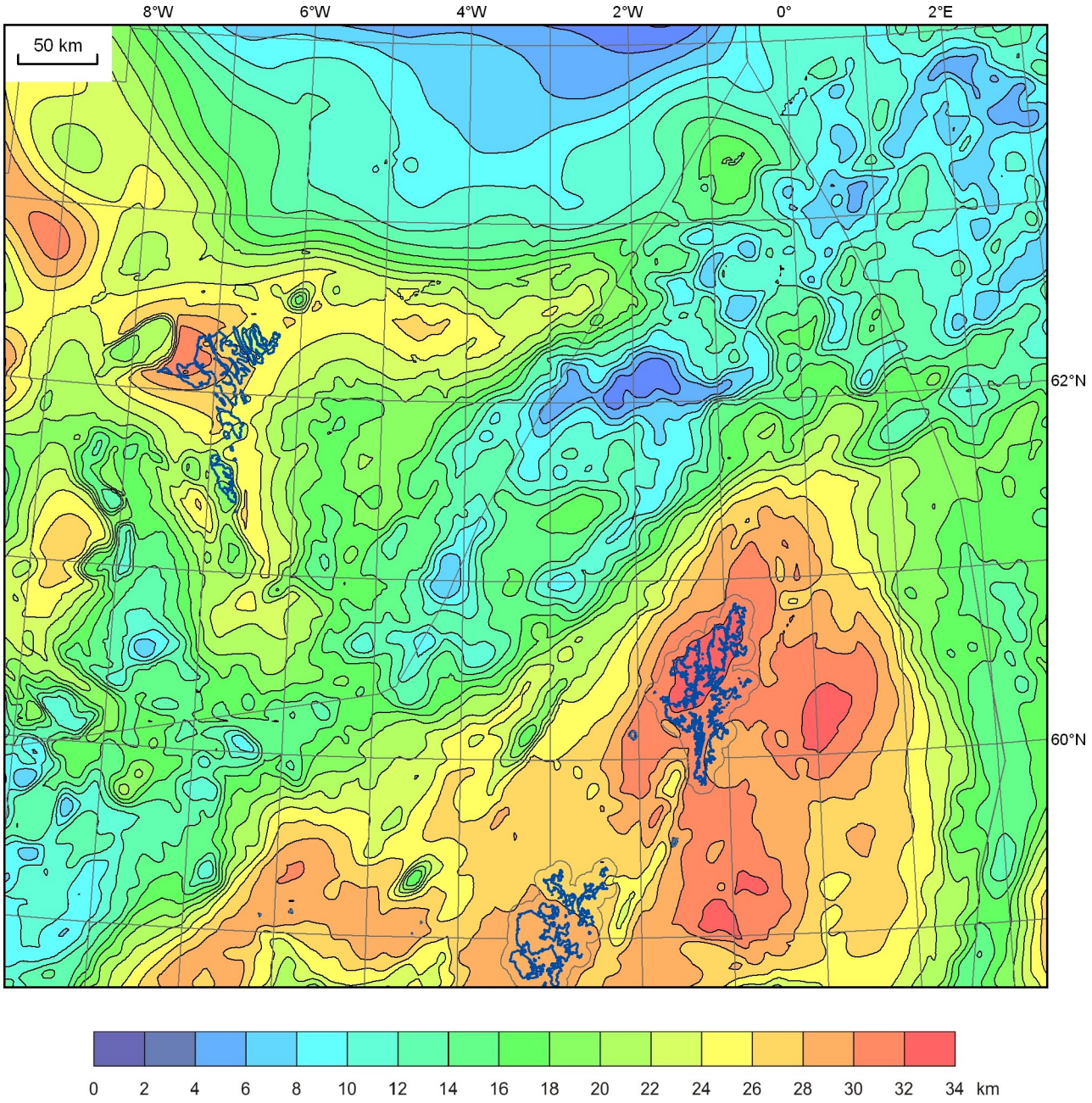

Figure 33 Thickness of crystalline crust in the optimised model

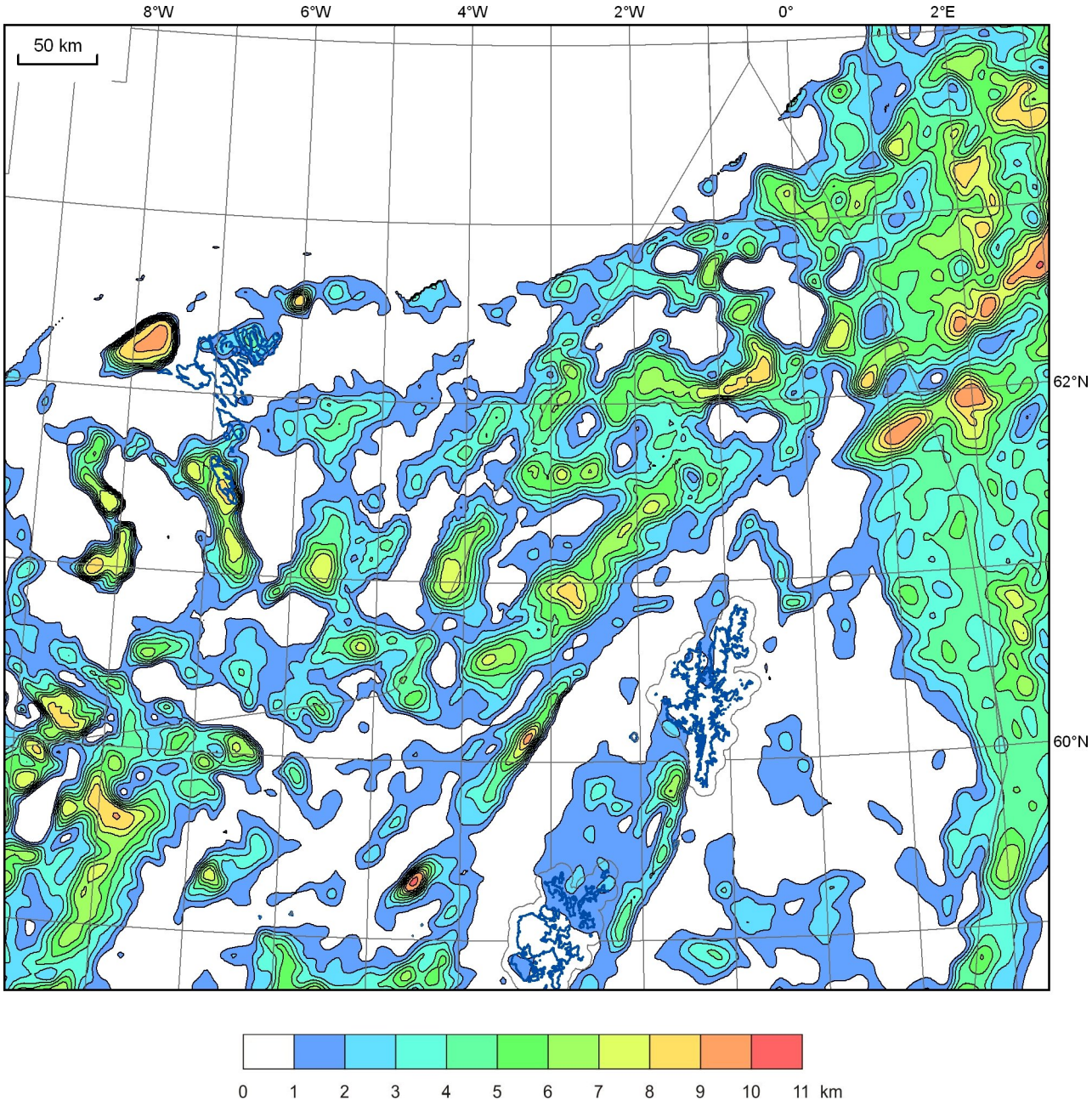

Figure 34 Optimised thickness of pre-Cenozoic sedimentary rocks

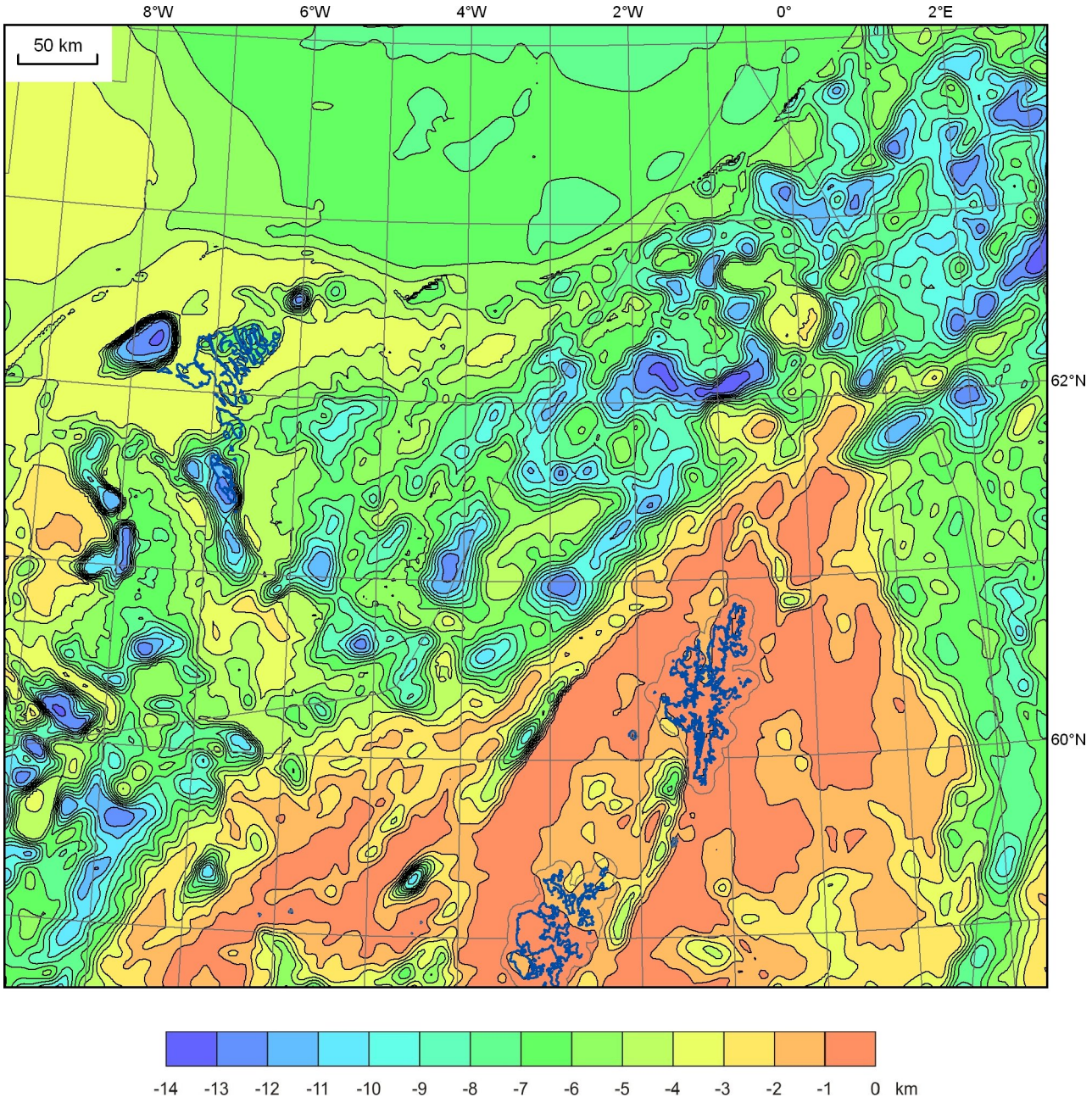

Figure 35 Optimised depth to basement

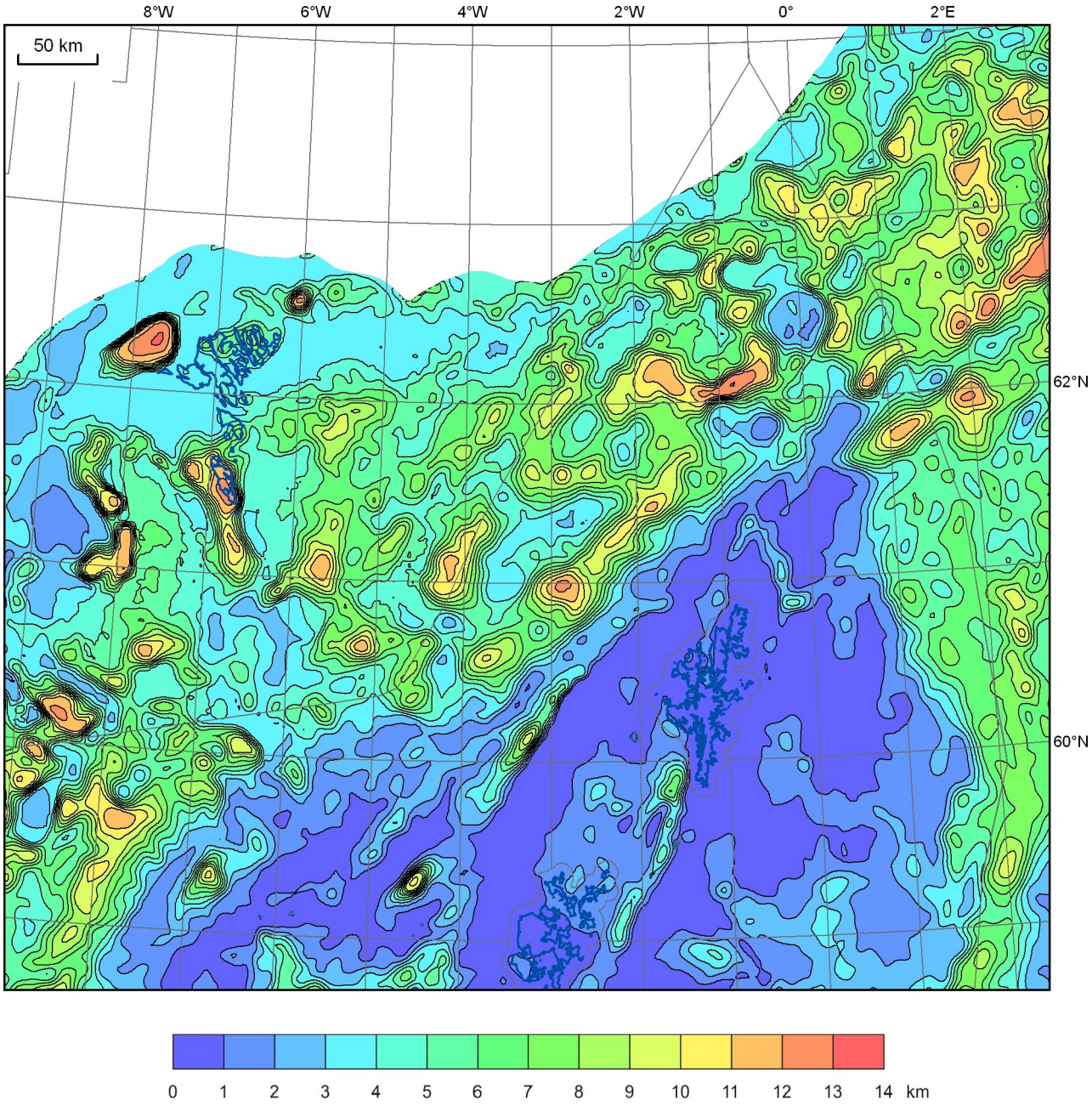

Figure 36 Optimised total cover sequence thickness

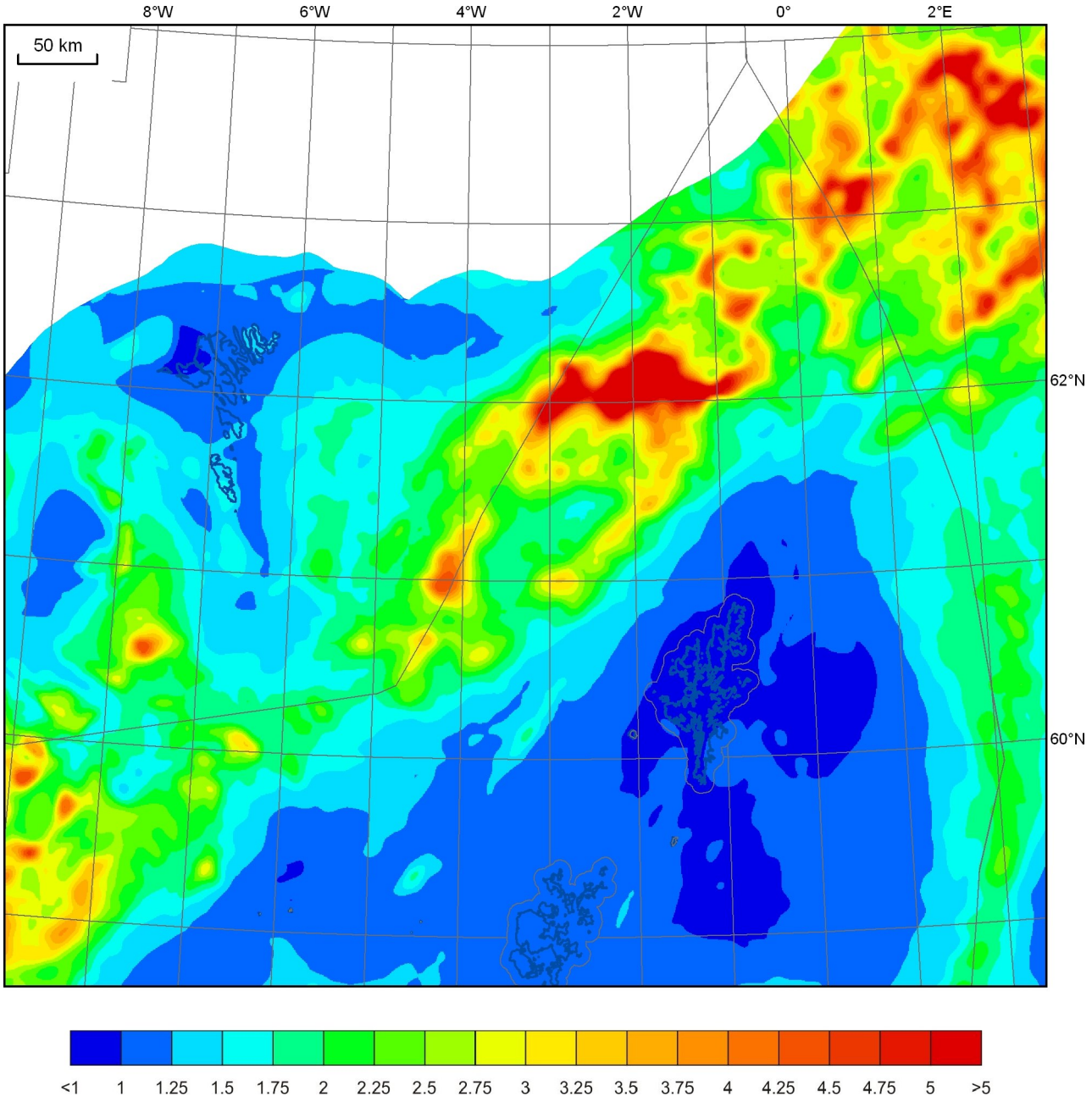

Figure 37 Apparent extension factor (derived from thickness of crystalline crust in the optimised model)

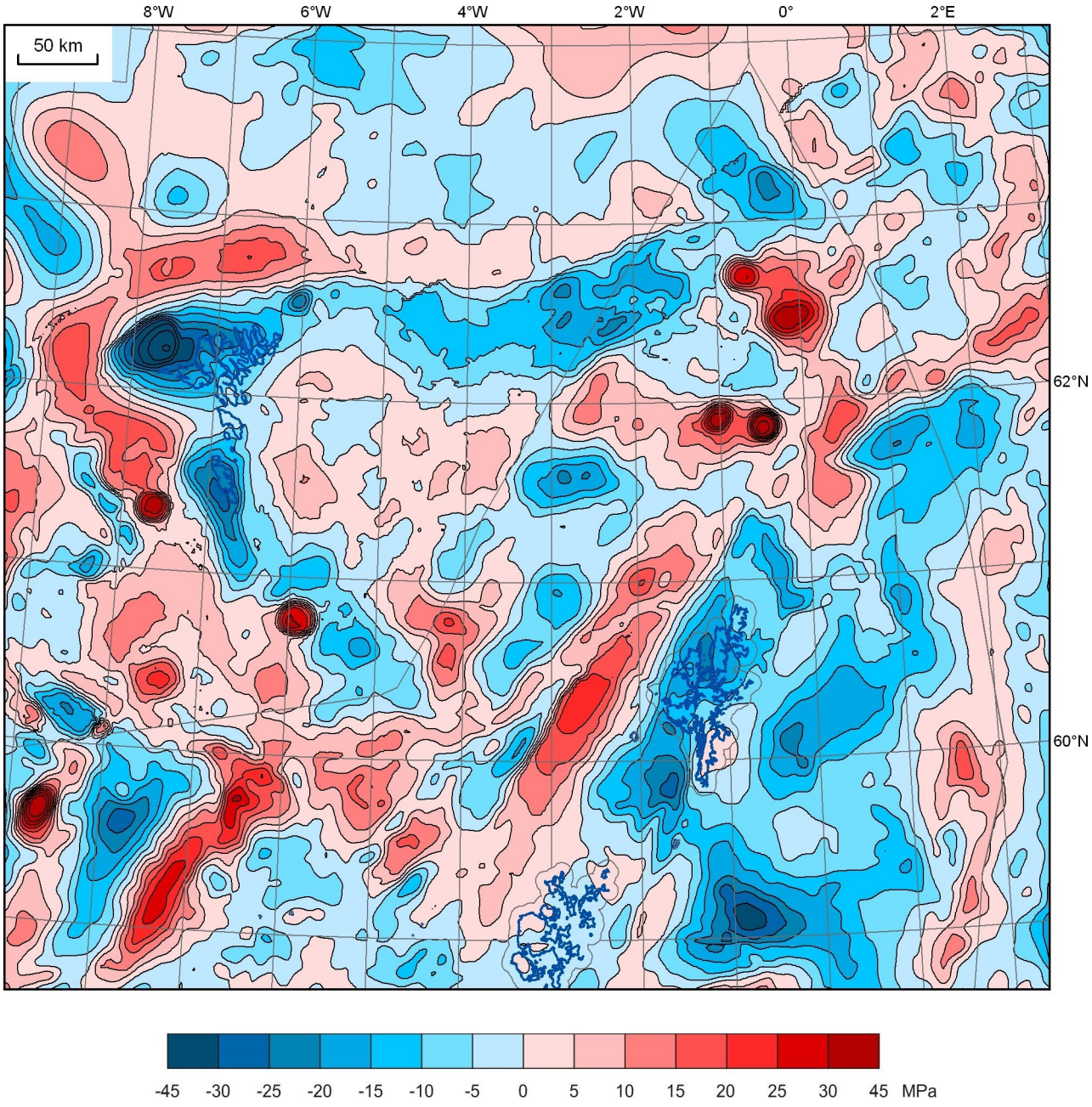

Figure 38 Load anomaly (departures from local isostasy) of the optimised model

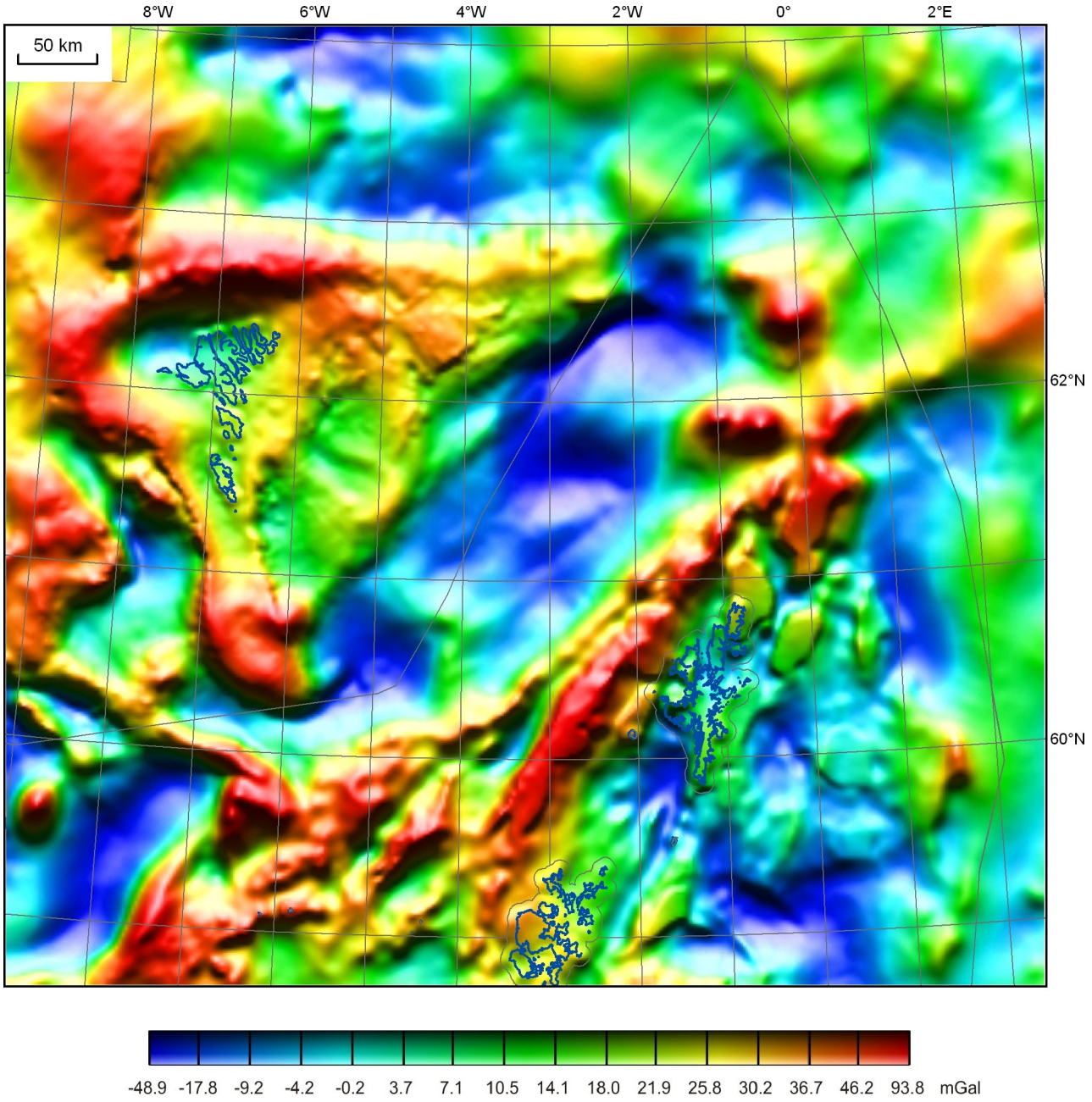

Figure 39 Calculated gravity field over the optimised model. Colour shaded-relief image with illumination from the north.

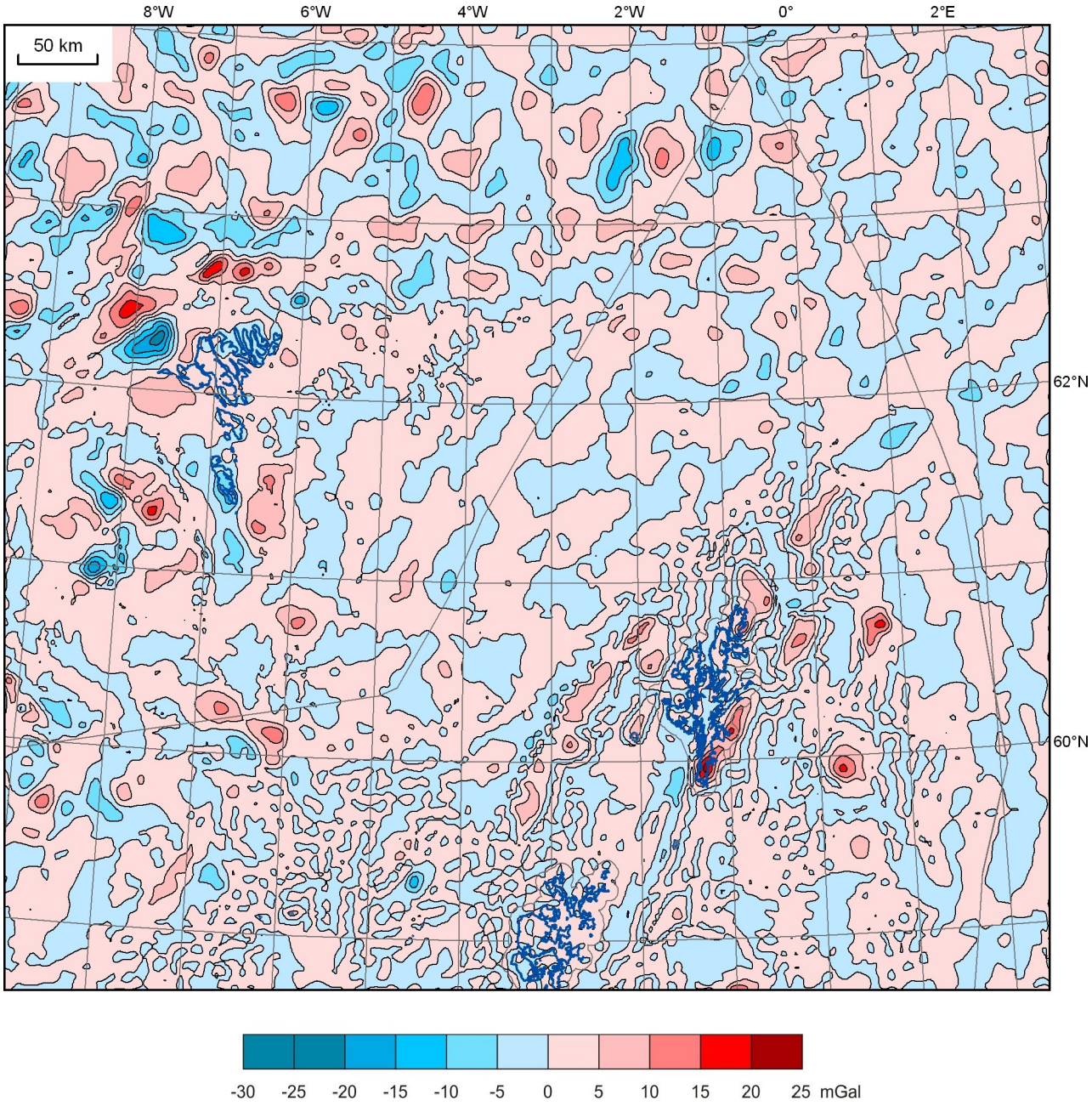

Figure 40 Residual gravity anomalies over the optimised model

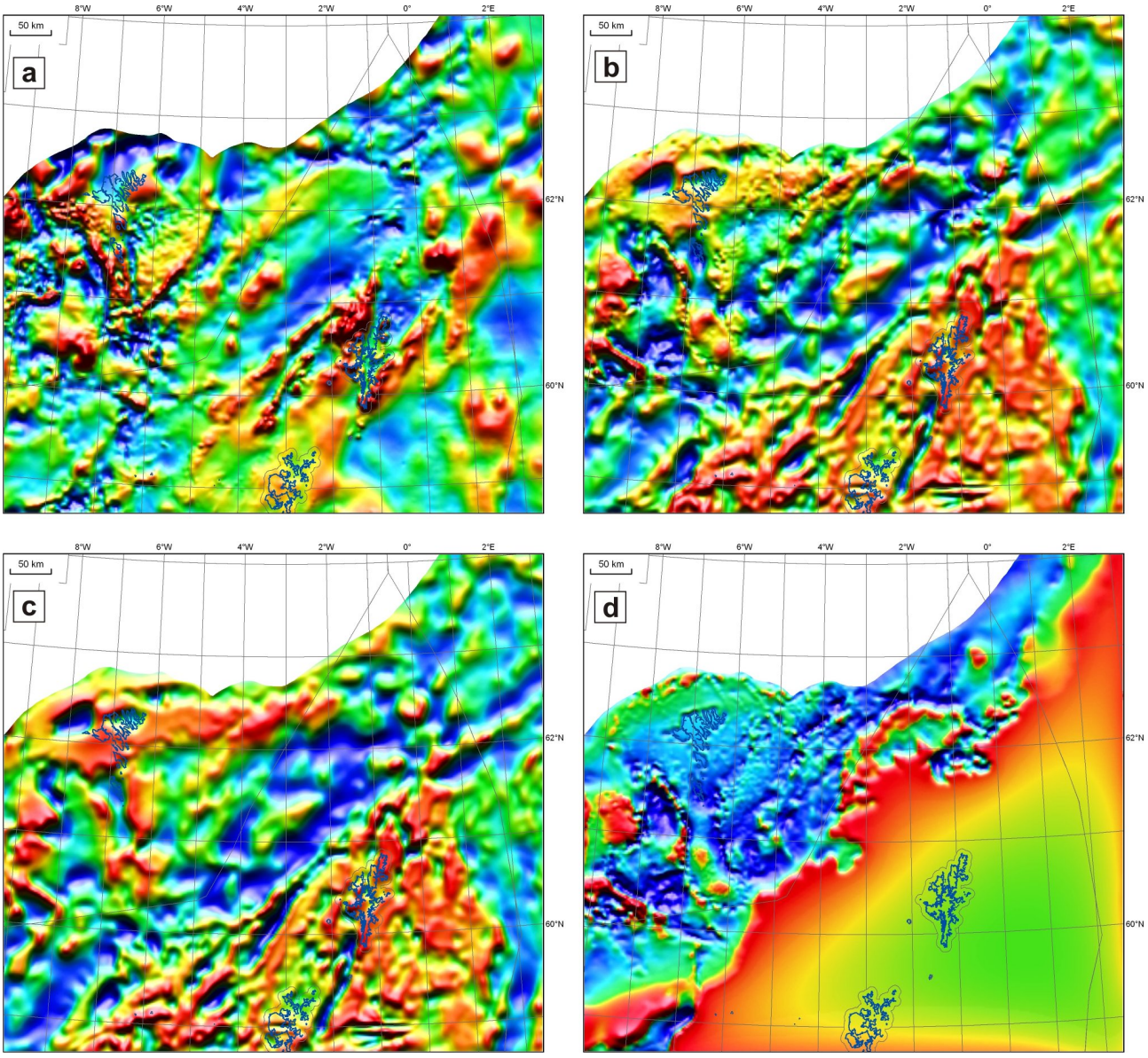

Figure 41 Results of magnetic modelling. (a) Observed magnetic field; (b) Forward magnetic model; (c) Forward magnetic model (just the basement component); (d) Forward magnetic model (just the volcanic component). All fields have been upward continued by 1 km to suppress the shortest wavelength features. Images employ equal colour area and illumination from the north.

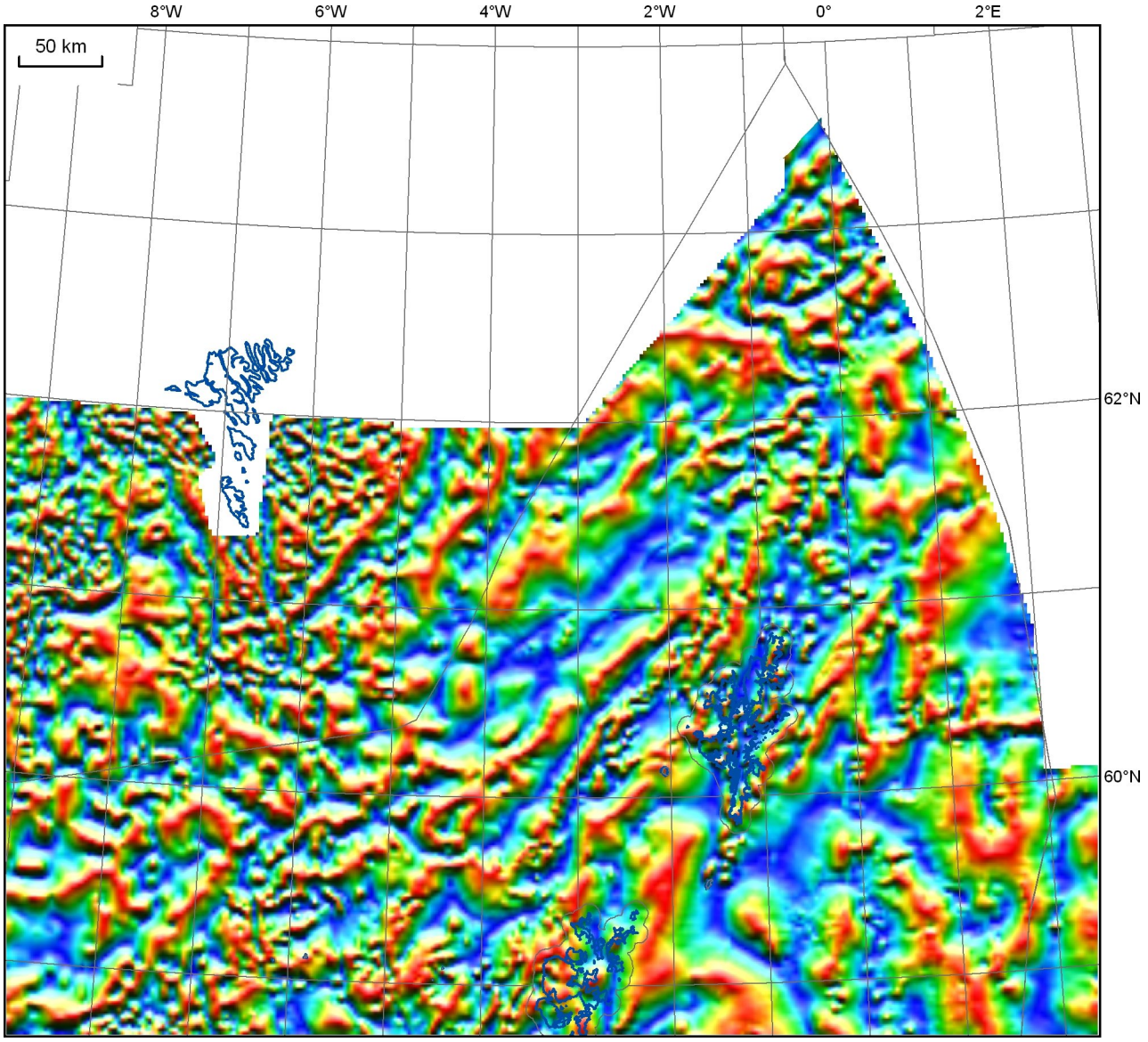

Figure 42 Image of the magnetic tilt-angle (over the area with adequate magnetic data coverage). Data lie within the range -90º and +90º; low values in blue and high values in red. Illumination is from the north.

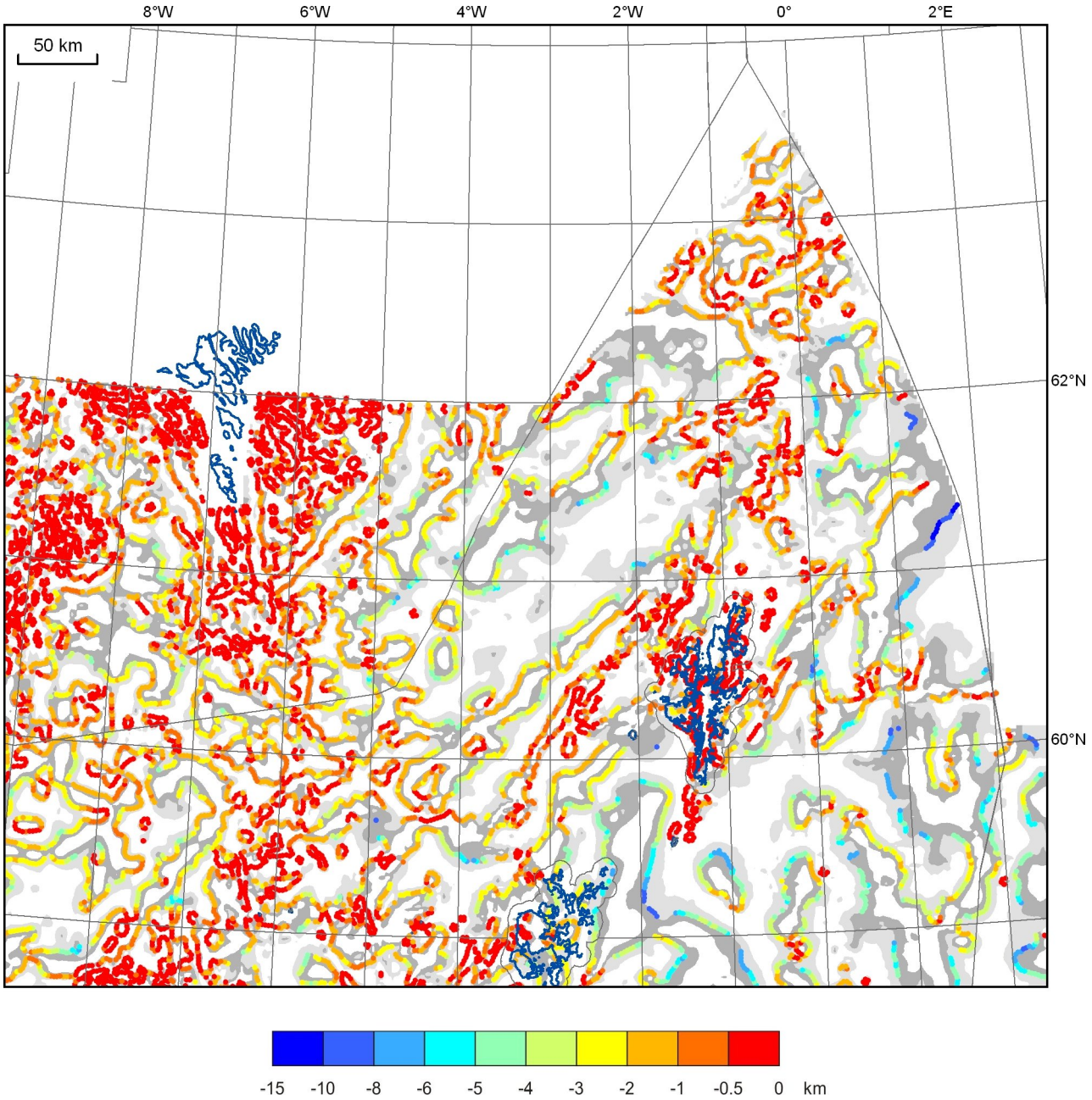

Figure 43 Apparent source depths calculated from the tilt derivative by the method of Salem et al. (2007). The zone with tilt-angles between -45° and 0° is shown in pale grey and that between 0° and +45° in dark grey.

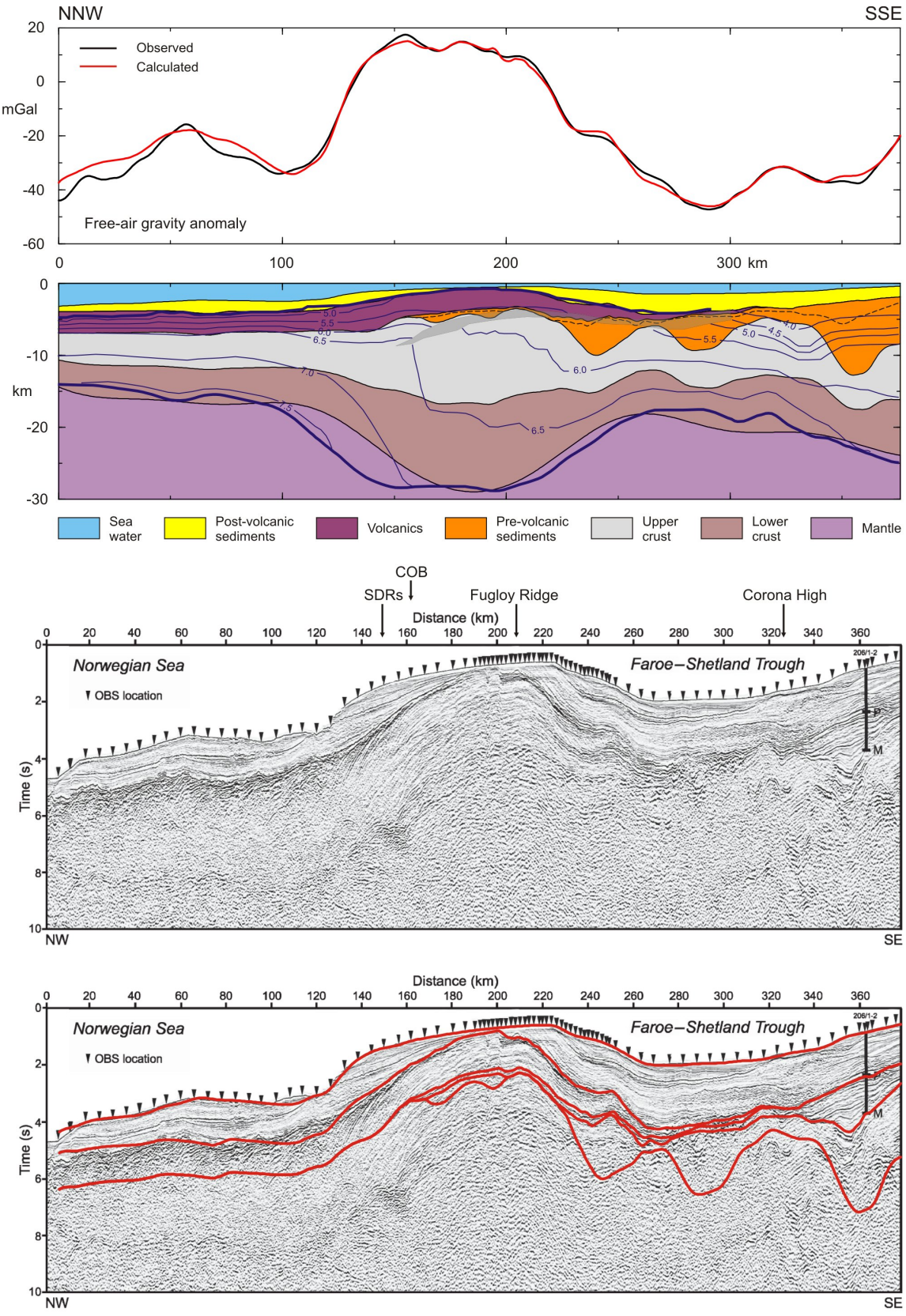

Figure 44 Comparison of a section extracted from the 3D model with the iSIMM results. The top two panels show the model fields and cross-section, on which are superimposed (in dark blue) the velocity contours and Moho and top basalt interfaces (bold) of Roberts et al. (2009b). The black dashed line is the base Cenozoic unconformity. The lower panels show the iSIMM Q-profile (time) section from Roberts et al. (2005; reproduced with the permission of WesternGeco and The Geological Society), with the model horizons superimposed in red on the bottom one. For profile location see Figure 30.

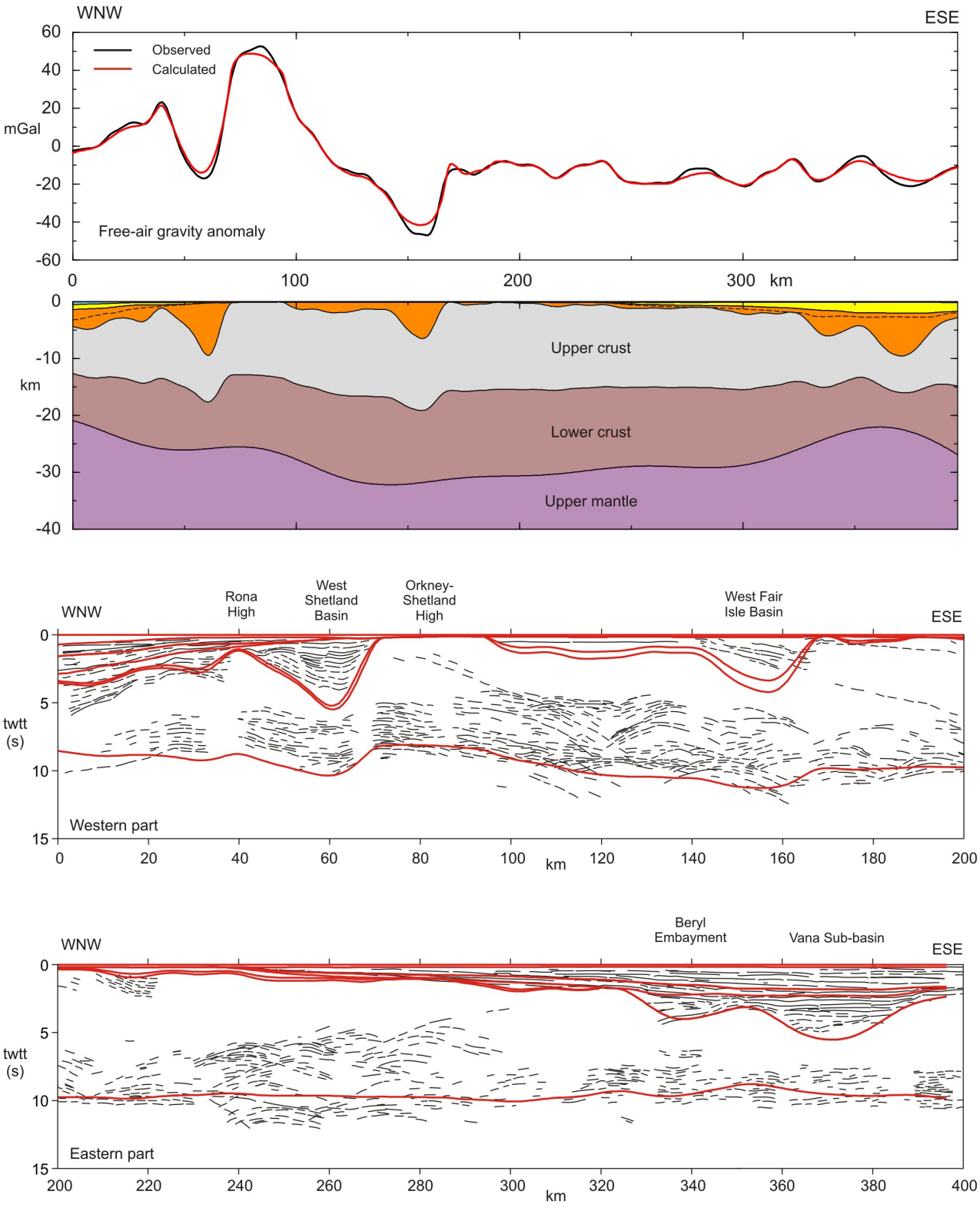

Figure 45 Comparison of the model results with the NSDP84-3 seismic profile. See Figure 44 for model legend. Model horizons (in red) are superimposed on a line drawing from the seismic section (after Ritchie et al. (2011), with a south-eastward extension) which is split into two halves. Alternative top basement horizons are shown on this section: the shallower one makes allowance for overcompaction using the amount of denudation indicated in Figure 14b.

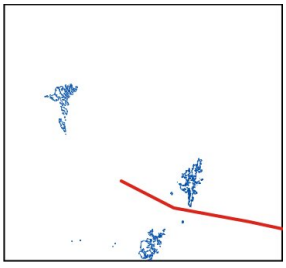

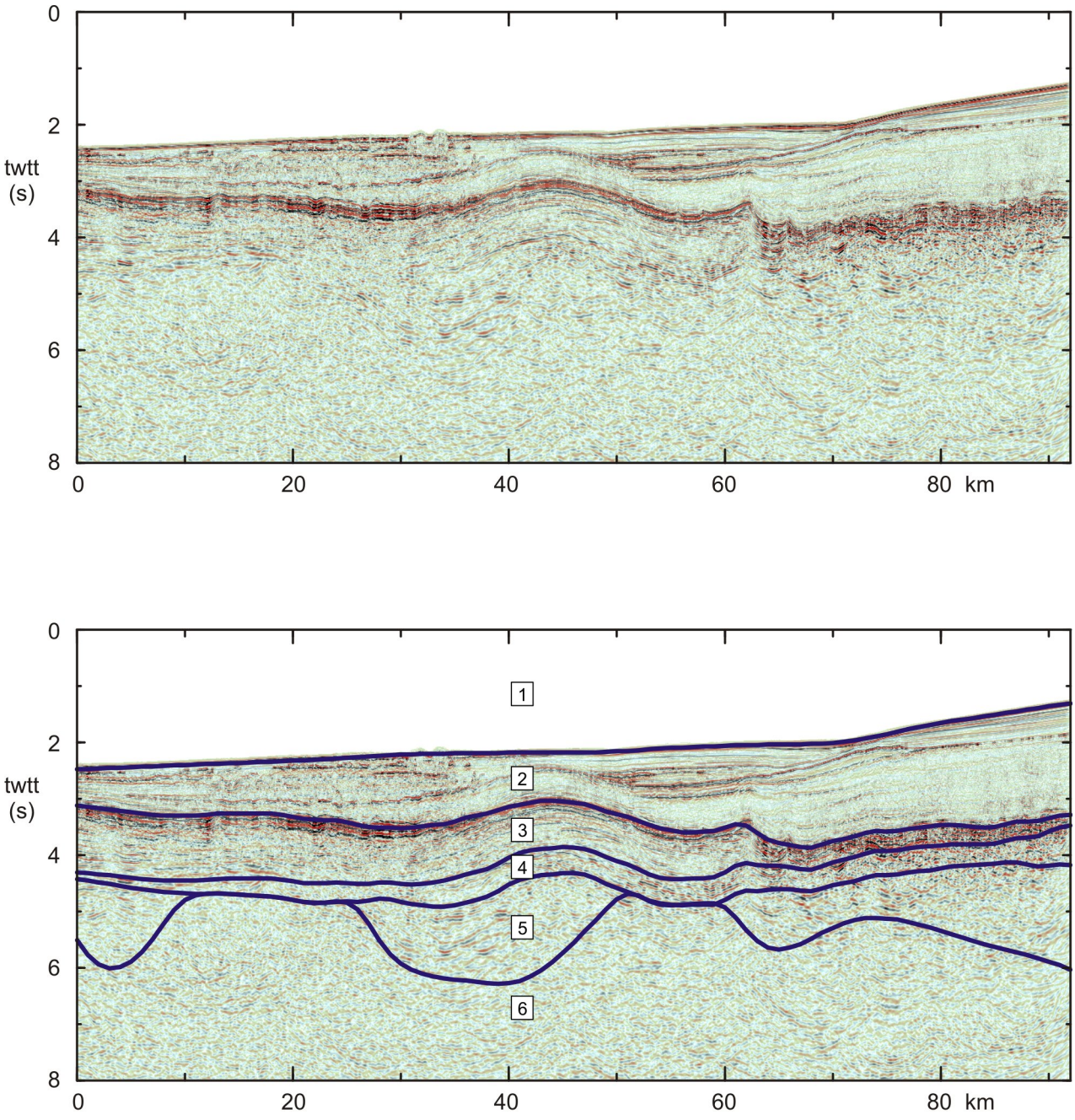

Figure 46 Illustrative seismic section from the Faroe-Shetland Consortium database. Horizons from the 3D model are superimposed on it in the bottom panel. 1 = sea water; 2 = post-volcanic sediments; 3 = volcanic rocks; 4 = pre-volcanic Cenozoic sediments; 5 = pre-Cenozoic sediments (may include thickening of the Paleocene sedimentary sequence); 6 = basement.

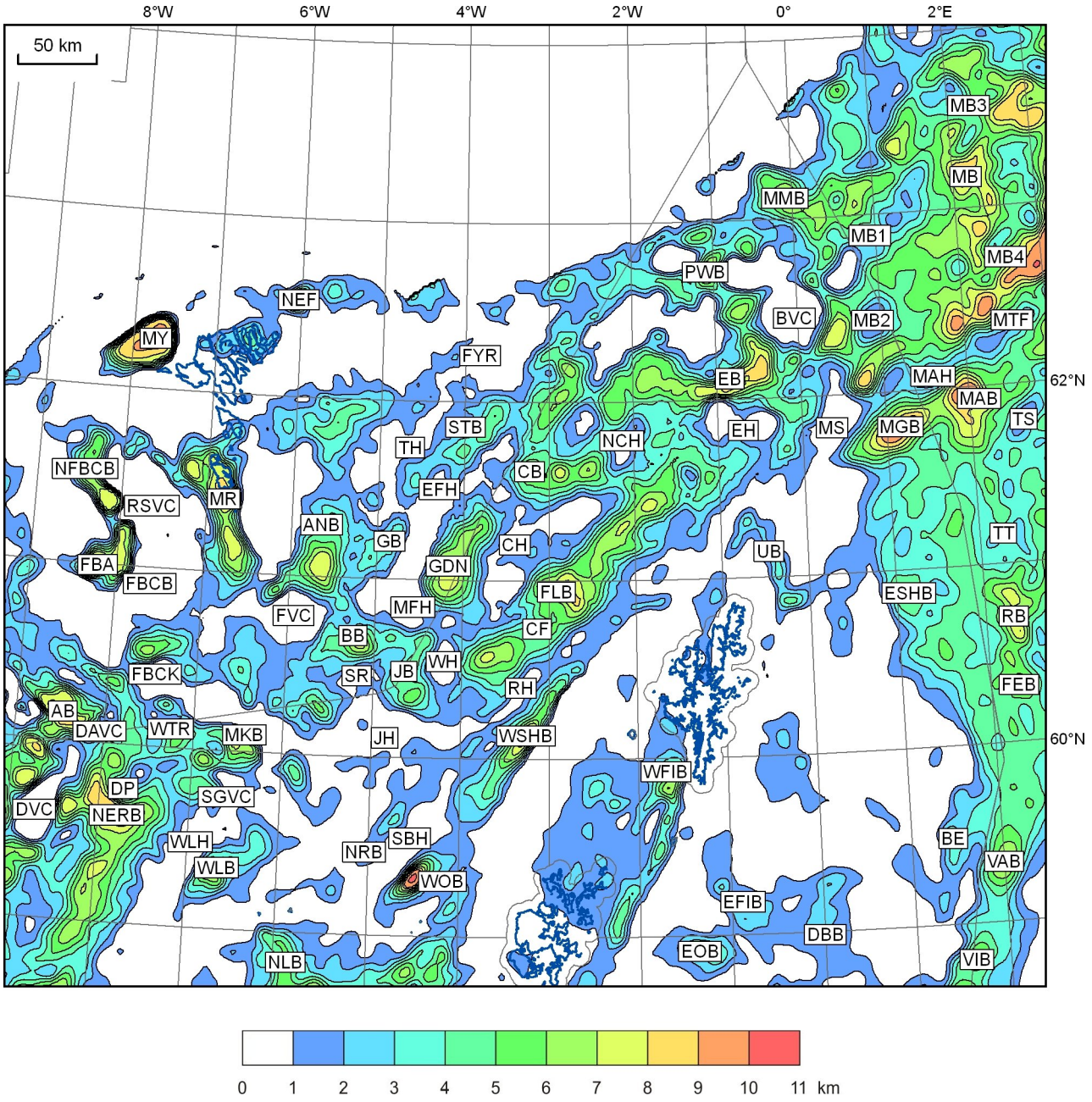

Figure 47 Modelled thickness of pre-Cenozoic sedimentary rocks with feature labels superimposed (see Appendix 4 for a list of abbreviations and Section 7.4 of the text for descriptions)

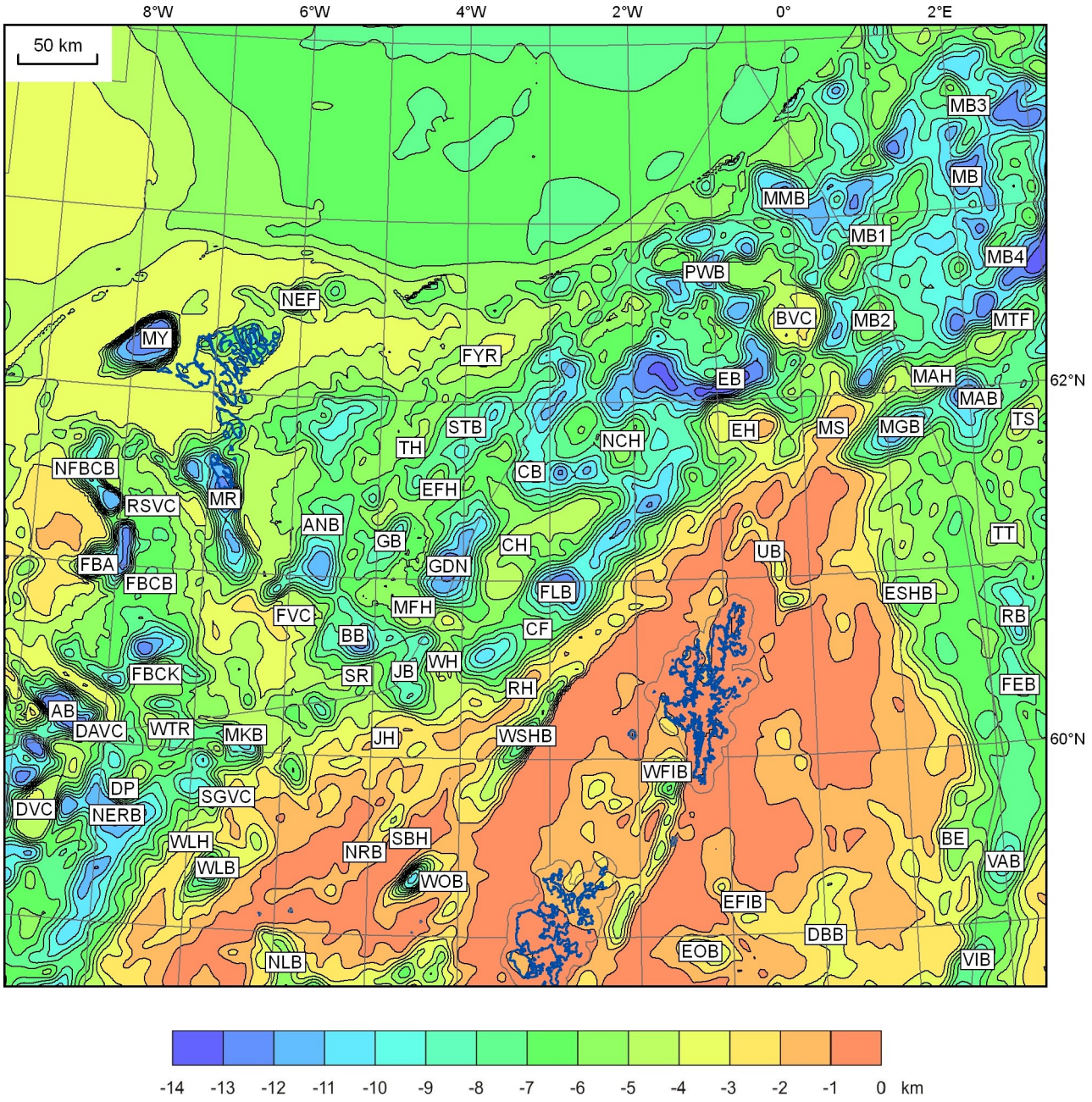

Figure 48 Modelled depth to basement with feature labels superimposed (see Appendix 4 for a list of abbreviations and Section 7.4 of the text for descriptions)

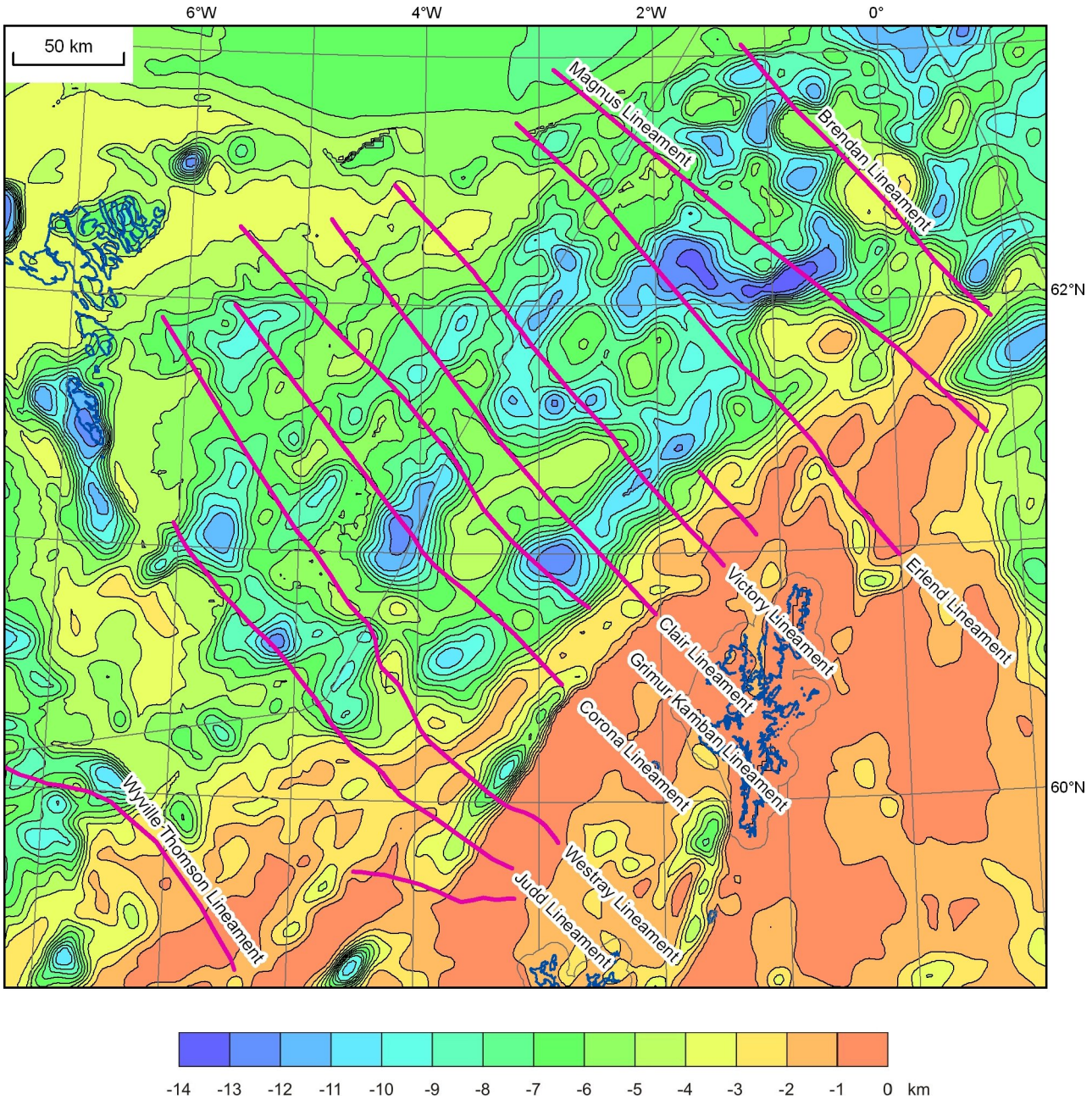

Figure 49 Lineaments of Ritchie et al. (2011) superimposed on modelled top basement